

Performance and Wake Analysis of a Darrieus Wind Turbine on the Roof of a Building using CFD

Marc Alexandre Allard

A Thesis
in The Department
of
Mechanical, Industrial and Aerospace Engineering

Presented in Partial Fulfillment of the Requirements for the Degree of

Master of Applied Science (Mechanical Engineering)

at
Concordia University
Montreal, Quebec, Canada

December 2020

© Marc Alexandre Allard, 2020

CONCORDIA UNIVERSITY
School of Graduate Studies

This is to certify that the thesis prepared

By: Marc Alexandre Allard

Entitled: Performance and Wake Analysis of a Darrieus Wind Turbine on the Roof
of a Building using CFD

and submitted in partial fulfillment of the requirements for the degree of

Master of Applied Science (Mechanical Engineering)

complies with the regulations of the University and meets the accepted standards with respect to
originality and quality.

Signed by the final Examining Committee:

_____	Chair
<i>Dr. Martin Pugh</i>	
_____	Examiner
<i>Dr. Mojtaba Kheiri</i>	
_____	Examiner
<i>Dr. Radu Grigore Zmeureanu</i>	
_____	Supervisor
<i>Dr. Marius Paraschivoiu</i>	

Approved by _____

Dr. Mamoun Medraj, Graduate Program Director
Department of Mechanical, Industrial and Aerospace Engineering

_____ 2020

Mourad Debbabi, Ph.D., Dean
Gina Cody School of Engineering and Computer Science

ABSTRACT

Performance and Wake Analysis of a Darrieus Wind Turbine on the Roof of a Building using CFD

Marc Alexandre Allard

In order to reduce greenhouse gas emissions and counter climate change, efforts have been made towards the development of technologies in the field of renewable energies. Wind turbines emerged as a result of these efforts. A significant amount of research has been made to increase their power producing capabilities. The concept of positioning micro-scale wind turbines on the roof of buildings is currently being studied due to the possible benefits of onsite power generation. The research detailed in this thesis concentrates on the performance and wake analysis of a Darrieus wind turbine, with a Troposkien shape, located above the roof of a cubic building at two different positions and operating under different wind flow conditions. The results presented are obtained from 3D unsteady Computational Fluid Dynamics (CFD) simulations and the applied methodology is validated by comparing coefficient of power (C_p) data from validation cases with a $C_p - \lambda$ curve acquired experimentally by Sheldahl. The first position considered is above the center upstream edge of the building, whereas the second one is located above one of the upstream building roof's corners at a lower height. An atmospheric boundary layer is enforced at the inlet of the domain with a selected desired velocity pointing at the center of the rotor. C_p values from the roof-mounted simulations are computed using various tip speed ratios and three different wind directions. Furthermore, the rotor's wakes in each scenario are measured and their behaviors are discussed. It is found that at a tip speed ratio of 5, the turbine's C_p can be increased from 0.318 to 0.549 by positioning it above the building's corner. Analysis of the rotor wake's structure at this location also revealed that because the wake mixes with the surrounding accelerated flow, it is shorter than when operating in a freestream.

ACKNOWLEDGMENTS

I would first like to thank my supervisor, Dr. Marius Paraschivoiu, for allowing me to conduct the necessary research and numerical simulations that form the bulk of this thesis' work. I also wish to express to him my sincere gratitude for his professionalism, his constant support and his optimism, without which my experience as a master student would have been much different. A special thank you to Mr. Scott Bunnell, as well as the entire technical support staff assigned to Concordia's Speed cluster, for helping me run my simulations and for their professionalism.

I would also like to thank my parents Pierre and Dominique, my brother Matthieu and Fannie, the love of my life, for their unconditional support and encouragement throughout this experience. Words cannot express how grateful I am for their presence and care. I know they will always be there, no matter how hard things get in my life.

To my dear friends and colleagues from the research lab, Maxime, Marie, Jean, Sean, Jiyeon, Alex, Belkacem, Maria and many others, thank you very much for all your support and help throughout these 2 years. Your presence has made my experience much more enjoyable and enriching and for this, I am forever grateful.

Finally, a special thanks to all the content creators of this world, especially those who create the amazing video games/movies soundtracks that I listen to daily. It helps me stay focused and motivated when I work and I am grateful for it.

TABLE OF CONTENTS

LIST OF FIGURES	vii
LIST OF TABLES	x
NOMENCLATURE	xi
CHAPTER 1: INTRODUCTION	1
1.1 Motivation.....	1
1.2 Objectives	5
1.3 Types of Wind Turbines	5
1.3.1 Horizontal Axis Wind Turbine (HAWT).....	5
1.3.2 Vertical Axis Wind Turbine (VAWT).....	7
1.4 VAWT Aerodynamics and Flow around Buildings.....	11
1.4.1 NACA 0012 Airfoil	11
1.4.2 VAWT Aerodynamics	11
1.4.3 Wind Flow around Buildings.....	14
CHAPTER 2: COMPUTATIONAL METHODOLOGY DESCRIPTION.....	17
2.1 Wind Profile and Wind Turbines Performance Equations	17
2.1.1 Wind Profile Equation	17
2.1.2 Tip Speed Ratio.....	17
2.1.3 Power Coefficient	18
2.2 Meshing Methodology	19
2.3 Wall Treatment Approach.....	20
2.4 Turbulence Modeling Approach	23
2.4.1 Reynolds-Averaged Navier-Stokes (RANS) Approach.....	23
2.4.2 The k- ω SST Turbulence Model.....	25
2.4.3 Large Eddy Simulations.....	27
2.4.4 Direct Numerical Simulations.....	28
2.5 Boundary Conditions	28
2.5.1 Symmetry Plane Boundary condition	28
2.5.2 Velocity inlet Boundary condition.....	28
2.5.3 Pressure Outlet Boundary condition	29
2.6 SIMPLE Pressure-Velocity Coupling Algorithm	29

CHAPTER 3: METHODOLOGY VALIDATION	30
3.1 Model Geometry	30
3.2 Computational Domain Geometry	32
3.3 Mesh Configuration	33
3.4 Boundary Conditions and Numerical Setup	38
3.5 Obtained validation results and discussion	39
CHAPTER 4: PERFORMANCE ANALYSES OF ROOF-MOUNTED DARRIEUS VAWT... 45	
4.1 Computational Domain's Geometry	45
4.2 Boundary Conditions	49
4.3 Meshes Configurations	51
4.3.1 Mesh Setup for Position 2 Simulations.....	51
4.3.2 Mesh Setup for Building Corner Simulations.....	56
4.4 Numerical Setup.....	59
4.5 Performance Results and Discussions	60
CHAPTER 5: WAKES AND WIND FLOW ANALYSES	66
5.1 Flow contours from the position 2 simulations.....	67
5.2 Flow contours from the building's corner simulations	69
CHAPTER 6: CONCLUSIONS AND FUTURE WORK.....	75
6.1: Summary and Conclusions	75
6.2: Future Work.....	76
REFERENCES	77

LIST OF FIGURES

Figure 1: Global trend in CO ₂ equivalents emanations from 1990 to 2016 [3]	1
Figure 2: Onshore wind turbine size increase in North America with future size predictions [7] .	2
Figure 3: Cleanfield Energy’s V3.5 turbine prototype [21].....	3
Figure 4: Horizontal axis wind turbine schematic [13]	6
Figure 5: A 200 kW fixed pitch H-rotor built by Vertical Wind [27]	8
Figure 6: 17m Sandia guy-wired phi-rotor (left), Illustration showing major components (right) [17].....	8
Figure 7: A 300 kW commercial Darrieus VAWT constructed by FloWind [29]	9
Figure 8: VMI 60 kW cantilevered (Troposkien) phi-rotor (left), artist impression of the VP100 components (right) [17]	10
Figure 9: NACA 0012 airfoil.....	11
Figure 10: Darrieus wind turbine blades section view [34].....	12
Figure 11: Aerodynamic forces acting on the blade [36]	13
Figure 12: Flow field schematic for a cubic building under turbulent flow conditions [41].....	14
Figure 13: Time-averaged streamlines for a cubic building case using an improved k- ω turbulence model [41]	15
Figure 14: Turbulent kinetic energy (m ² /s ²) contour obtained with an MMK-Bechmann RANS turbulence model [39]	16
Figure 15: Velocity contours of two cases with different turbine’s heights above a cubic building [40].....	16
Figure 16: CP versus TSR curve for a two bladed wind turbine [44].....	18
Figure 17: Boundary layer structure in Star CCM+ [45].....	21
Figure 18: All y + wall treatment [45]	22
Figure 19: Sandia Darrieus VAWT 2m model inside the wind tunnel testing site [33].....	30
Figure 20: VAWT model half rotor geometry	31
Figure 21: Bottom view of the computational domain	32
Figure 22: Right side view of the computational domain.....	33
Figure 23: Bottom view of the static and rotating regions’ mesh.....	34
Figure 24: Cross-sectional front view of the mesh	34

Figure 25: Blades mesh zones interface refinement	36
Figure 26: Blades hexahedral mesh at the symmetry plane.....	36
Figure 27: Inflation layers at the blades leading edge	37
Figure 28: Inflation layers at the blades trailing edge.....	37
Figure 29: Applied boundary conditions for each validation cases	38
Figure 30: Power Coefficient versus Tip Speed Ratio data	40
Figure 31: Moment coefficient plot for last 3 cycles of TSR=4.5 case	41
Figure 32: Top view of computational domain's velocity magnitude contour ($\lambda=4.5$).....	42
Figure 33: Top view of rotating region's velocity magnitude contour ($\lambda=4.5$)	42
Figure 34: Top view of a rotor blade velocity magnitude contour ($\lambda=4.5$)	43
Figure 35: Top view of a rotor blade pressure contour ($\lambda=4.5$).....	43
Figure 36: VAWT model full rotor geometry.....	46
Figure 37: Isometric view of the computational domain	46
Figure 38: Isometric view of the cubic building and the rotating region located at the building corner	47
Figure 39: Frontal view of the computational domain with a) VAWT positioned above the building's upstream edge center at position 2, b) VAWT located above the building's corner at position 1 height.....	48
Figure 40: Side view of the center of the domain with VAWT located at position 2	49
Figure 41: Wind profile for a straight wind (positive X) direction case.....	50
Figure 42: Boundary conditions and selected wind flow directions for the simulations.....	50
Figure 43: Frontal view of the position 2 cases mesh.....	52
Figure 44: Side section view of the position 2 cases mesh.....	52
Figure 45: Refined mesh around the building and the static/rotating regions' interface (position 2 cases).....	53
Figure 46: Rotating region's mesh for the position 2 geometry	53
Figure 47: Section view of a blade refinement zone structured mesh	54
Figure 48: Frontal view of the corner cases' mesh	56
Figure 49: Side section view of the corner cases' mesh	57
Figure 50: Refined mesh around the building and the rotor (corner cases).....	57
Figure 51: Mesh at the static/rotating regions' interface for the building corner geometry	58

Figure 52: C_p versus TSR for roof-mounted VAWT cases.....	61
Figure 53: Moment coefficient versus rotational angle ($^\circ$) plots for position 2 cases	62
Figure 54: Moment coefficient versus rotational angle ($^\circ$) plots for building's corner cases at TSR=3	62
Figure 55: Moment coefficient versus rotational angle ($^\circ$) plots for building's corner cases at TSR=5	63
Figure 56: Streamlines of velocity magnitude from the TSR=5 simulation on the rotor's center XZ plane.....	67
Figure 57: Side view of the flow streamlines above the roof on the rotor's center XZ plane for the TSR=5 case	67
Figure 58: Side view of the flow streamlines above the roof on the rotor's center XZ plane for the TSR=6 case	68
Figure 59: Streamlines of velocity magnitude from the TSR=3, straight wind simulation on the rotor's center XZ plane	69
Figure 60: Flow streamlines around the rotor on its center XZ plane from a) the TSR=3 straight wind case and b) the TSR=5 straight wind case	70
Figure 61: Section view of flow streamlines from the TSR=3 case with a 45° , positive Y wind direction	70
Figure 62: Section view of flow streamlines from the TSR=5 case with a 45° , positive Y wind direction	71
Figure 63: Section views of flow streamlines from a) the TSR=3 case with a 45° , negative Y wind and b) the TSR=5 case with a 45° , negative Y wind	71
Figure 64: Top views of flow streamlines at the rotor's center XY plane from a) the straight wind TSR=3 case and b) the straight wind TSR=5 case.....	72
Figure 65: Top views of flow streamlines at the rotor's center XY plane from a) the TSR=3 case with a 45° , positive Y wind and b) the TSR=5 case with a 45° , positive Y wind.....	72
Figure 66: Top views of flow streamlines at the rotor's center XY plane from a) the TSR=3 case with a 45° , negative Y wind and b) the TSR=5 case with a 45° , negative Y wind	73

LIST OF TABLES

Table 1: Important dimensions of the tested Sandia model.....	31
Table 2: Mesh parameters and sizes	35
Table 3: Calculated power coefficients from validation cases	40
Table 4: Mesh parameters for position 2 cases	55
Table 5: Mesh parameters for the building's corner cases	59
Table 6: Calculated power coefficients for roof-mounted cases	61
Table 7: Approximate dimensions of the mixed flow phenomenon for position 2 cases.....	68
Table 8: Approximate wakes' dimensions for building's corner cases	73

NOMENCLATURE

VAWT	Vertical Axis Wind Turbine
D	Diameter of the rotor
R	Radius of the rotor
C	Chord length
V	Vertical coordinate of the node
H	Height of the rotor
h	Height of the building
C_M	Coefficient of Moment
C_P	Coefficient of Power
λ	Tip Speed Ratio
M	Moment
ω	Angular velocity of the rotating region
ρ	Air density
V_t	Free stream velocity at the center of the rotor
A_c	Cross-sectional area of the rotor

CHAPTER 1: INTRODUCTION

1.1 Motivation

Greenhouse gas emissions caused by the continuously expanding global demand in primary energy is a well-known and important issue [1]. The extraction processes and consumption of exhaustible fossil fuels such as coal, natural gas and oil in order to meet the world's requirements in energy usage are the principal causes of air pollution and climate change. In 2018, natural gas demand increased by 5.3% and made up almost 45% of the total growth in energy consumption. In a similar manner, coal demand increased by 1.4%. Both of these expansions occurred in conjunction with a rise of 2% in carbon emissions, which was the fastest growth recorded in several years [2]. Figure 1 shows that between 1990 and 2016, worldwide annual emanations of CO₂ equivalents increased greatly. At the end of 2016, a total of 49.3 gigatonnes of CO₂ equivalents had been released in the atmosphere throughout the course of the year, as shown by Olivier et al. [3]. From this quantity, about 31 gigatonnes is related to energy consumption, which amounts to 63% of the total CO₂ equivalents emissions for this year [3].

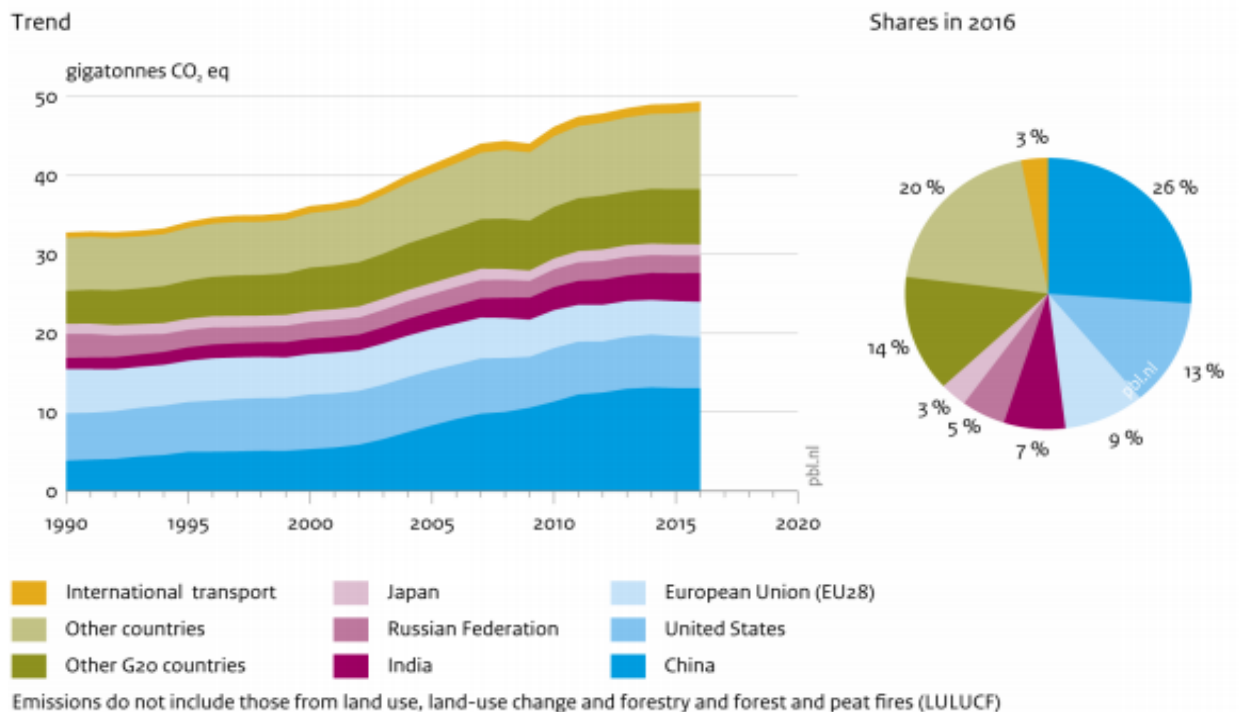


Figure 1: Global trend in CO₂ equivalents emanations from 1990 to 2016 [3]

In order to help decrease greenhouse gas emissions from exhaustible fossil fuels and reduce the impacts of climate change, interests in renewable sources of energy production such as hydro, solar and wind power have been growing rapidly over the past decades. Worldwide wind power installed capacity reached 591 GW at the end of 2018 with a total rise of 51.3 GW throughout the year only. Amongst the different countries that contributed to this growth, China and the USA stood out in particular with a respective 21.2 GW and 7.6 GW increase in onshore wind turbine capacity [4]. According to the GWEC (Global Wind Energy Council), increase in offshore and onshore installed capacity should reach more than 55 GW per year up to 2023 [4]. By considering the geophysical limits of the Earth's wind power capacity only, Marvel et al. [5] found that more than enough energy is contained in the wind to meet the increasingly high global demand in power consumption. With the wind power industry in full expansion, new offshore and onshore wind turbine models are being added to the market with a focus on enhancing their maximum power generating capabilities. These newer turbines often come with larger rotor sizes (Figure 2), which generate downstream wakes that are considerably bigger and longer than their predecessors. To avoid important power losses in wind farms due to the highly turbulent and slower air from these wakes, wind turbines need to be installed at a certain distance from each other to avoid been affected by their neighbors' wakes. This distance increases with the rotor diameter D , which is a clear drawback from increasing the rotor size [6].

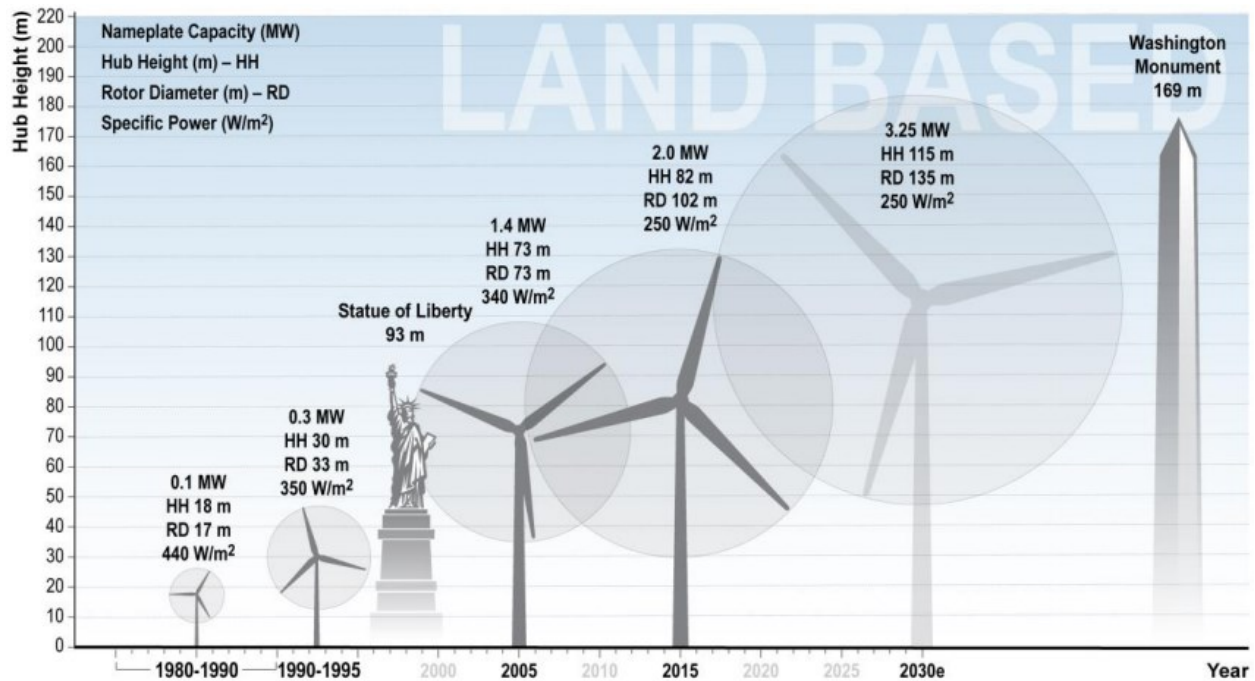


Figure 2: Onshore wind turbine size increase in North America with future size predictions [7]

In order to offer a complementary solution to massive wind farms and their ensuing high costs due to the production and installation of increasingly bigger turbines, the concept of installing small-scale wind turbines on rooftops in urban areas has received a lot of attention in the wind turbine research community [8], [10], [20]. A micro-scale wind turbine is defined as any wind turbine with an installed power of less than 2.5 kW [58]. Statistics on buildings' overall power consumption reveal that around 40% of the total global energy consumption is related to the building sector along with a third (30%) of the world's greenhouse gas emissions. Furthermore, it was found that over 80% of those emissions are produced during the buildings' operational phase due to ventilation, air conditioning, heating and other operations [11]. With the prospect of onsite power generation in urban environments, which would reduce losses related to transmission in power lines, along with achieving lower levels of building related greenhouse gas emissions, the potential benefits of building mounted wind turbine technology are clear.

Figure 3 shows an experimental H-Type Darrieus vertical axis wind turbine with modified NACA 0015 airfoils profiles for the blades. This small-scale wind turbine was tested on the roof of the McMaster Innovation Park main building in Hamilton, for the purpose of evaluating the impacts of urban unsteady wind conditions on the turbine's performance [21].



Figure 3: Cleanfield Energy's V3.5 turbine prototype [21]

It is well known that the wind present in urban locations is both slower and more turbulent when compared to rural areas. The complexity of these wind flows is due to the presence of the buildings themselves and their various effects on the wind flows' aerodynamic behavior. Such a situation poses an important challenge for the implementation of building mounted wind turbines in urban

areas. In addition to the requirement of conducting additional research on the subject of urban wind flow aerodynamics, a necessity to acquire more experimental data on wind turbines in these locations was expressed by Stathopoulos et al. [20]. Also, it was suggested by KC et al. [22] that improvements to the current international design standard for small wind turbines (SWTs), in order to better include urban wind conditions, needed to be done to ensure the reliability and efficiency of future designs. Al-Quraan et al. [18] showed that the accuracy of atmospheric boundary layer wind tunnel technology in predicting the energy yield potential of turbulent urban wind flows is not always acceptable as it depends on the roughness of the upstream terrain of the building. By comparing experimental field tests results with the data obtained from wind tunnel tests, it was determined from this study that the estimated data from wind tunnel testing tends to underpredict the energy yield potential of the urban wind (up to a 20% difference for highly heterogeneous and rough terrain).

Drew et al. [23] reported that 38 building mounted wind turbines in the UK performed below expectations during field tests conducted by Energy Saving Trust. The study found that the wind speed data used for assessing the technical and economic feasibility of these small wind turbines was obtained from low-resolution wind speed databases that do not accurately reflect the local changes in wind resource. These databases were generated by wind speed assessment tools (namely the NOABL and the Energy Saving Trust wind speed estimator) that were shown to tend to overpredict the local wind speeds, which led to shortcomings in these wind turbines' expected power producing capabilities. Thus, it is clear that a need to better understand the different effects of wind flows disturbed by buildings on roof-mounted wind turbines' performance is still present. One of the indirect methods that is used to predict wind flow behavior is Computational Fluid Dynamics (CFD). A number of recent studies used this numerical method to conduct accurate vertical axis wind turbines performance analyses [24], [25], [26]. Furthermore, the effectiveness of this numerical method in performing analyses of building-mounted wind turbines' performance was shown in Larin's work [9]. The importance of including the building's geometry in the simulation, to accurately assess the wind turbine's performance, was also emphasized by Larin [9].

The results presented in this thesis were obtained from multiple 3D CFD simulations of unsteady wind flow around wind turbines. The goals of the simulations that involve both a roof-mounted vertical-axis wind turbine (VAWT) and a building were to study the impacts of turbine positioning on its performance and to analyze the wakes formed by the turbine model in the different scenarios. It is also important to mention that the CFD code used to prepare and run all of the cases shown is Star CCM+.

1.2 Objectives

The main goal of this research is to evaluate the wind power extracting performance, under various conditions, of the tested roof-mounted Darrieus VAWT model and discuss its wake's behavior and shape in each scenario. In order to accomplish this goal, the following objectives are set:

- Validate the CFD methodology used by comparing the obtained data shown in the validation chapter to Sandia Laboratories experimental data. The model, mesh and numerical setup involved are described in chapter 3 of this work.
- Investigate the impacts of different wind flows disturbed by the presence of a building on the coefficient of power (C_p) of a selected building mounted Darrieus Troposkien vertical-axis wind turbine (VAWT) model. The domain geometries, meshes and numerical setup involve are described in Chapter 4 of this work.
- Analyze the wind turbine wakes and their interactions with the flow around the building.

1.3 Types of Wind Turbines

There are two types of conventional wind turbines, horizontal axis wind turbines (HAWTs) and vertical axis wind turbines (VAWTs). The following section gives information on both of these categories. The work presented in this thesis focuses on a particular type of VAWT, the Darrieus Troposkien shaped wind turbine, which is described in this section as well. It is important to note that the more recent airborne wind turbines are not covered in this work.

1.3.1 Horizontal Axis Wind Turbine (HAWT)

Also known as propeller type turbines, HAWTs are the most commonly built type of wind turbines due to their higher efficiency ratings [12] and ability to pitch the blades about their longitudinal axis. Blades pitch control allows efficient rotor speed and power output control. It is also considered as the best method to prevent rotor overspeed and protect the turbine from intense wind speeds [13]. The HAWT's generator shaft is located inside the nacelle above the ground and can be connected to the rotor's shaft in different ways depending on the mode of operation. Figure 4

shows a schematic of the components found in propeller type turbines. Torque on the rotor shaft is generated by the lift force acting on the blades.

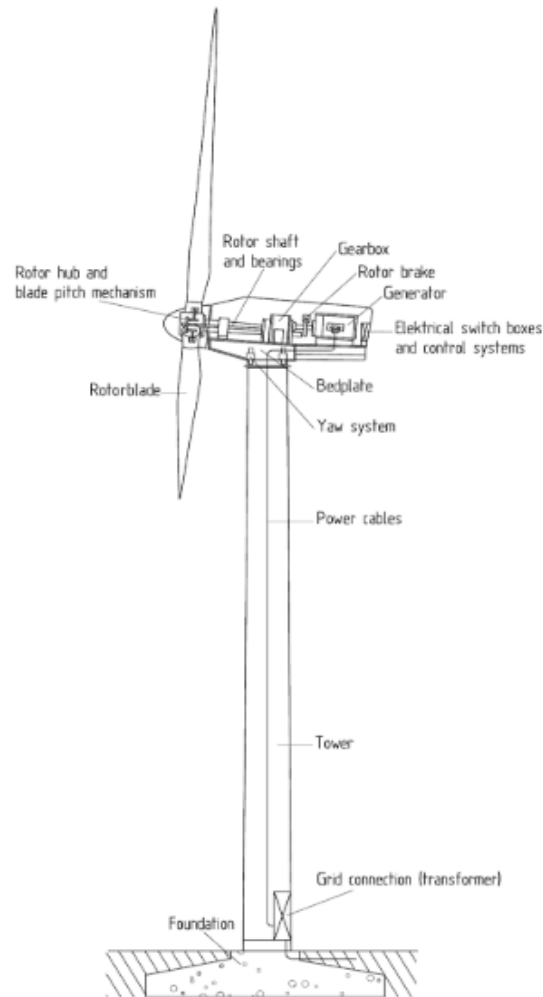


Figure 4: Horizontal axis wind turbine schematic [13]

In an effort to maintain maximum power extraction efficiency from the wind, HAWTs are equipped with yaw control systems to keep the rotor oriented as much as possible in the direction of the wind. This control system plays an important role in maximizing the turbine's efficiency and research is being done to further improve it by testing different approaches to modeling this particular system's behavior [14].

1.3.2 Vertical Axis Wind Turbine (VAWT)

Two different groups of wind turbines exist in this category, namely the Darrieus and Savonius types. The latter is composed of drag based turbines, from which the torque generated on the rotor shaft comes from the drag force applied on the blades. One of the main advantages of VAWTs over propeller type turbines is that they do not require installation of some of their components (such as the gearbox or generator) above ground. This is due to the orientation of the rotor shaft which is set transverse to the wind direction and is usually (but not always) vertical compare to the ground. VAWTs operation also benefits from being independent of the wind direction, which is not the case for HAWTs [15]. This might make them the ideal technology for urban environment integration, where the wind is slower and more turbulent [16]. A known shortcoming of VAWTs when compared to HAWTs is lower efficiency. It is due to the constantly changing apparent angle of attacks (AOAs) of the blades during a full rotation of the rotor. While the AOA of the upstream advancing blade is in the optimal position (highest lift generating potential), the other downstream retreating blades have higher AOAs which causes flow separation. This phenomenon leads to the important loss in lift force generation on the blades, which in turns negatively affects the turbine's power producing capabilities [12].

1.3.2.1 Darrieus Type Wind Turbines

Darrieus type wind turbines rely on the lift force to create torque on the rotor shaft. This kind of turbine is not always self-starting. Under high wind speed conditions and below the cut-off threshold, it is required that the rotor already be rotating in order to produce power. It should be noted however that recent Darrieus VAWT designs have shown better self-startup capabilities due to innovations in blades profiles' designs [19]. Throughout the development of Darrieus VAWTs, 2 major categories related to the turbine's shape were established: the curved and straight blades configurations. The fixed pitch H-rotor wind turbine model shown in Figure 5 is an example of straight blades design. This model is equipped with a directly driven permanent magnet synchronous generator that is located on the ground. The use of a generator of this type holds many advantages, such as avoiding losses and maintenance costs related to the gearbox. Furthermore, since the generator is located on the ground in this instance, design constraints related to weight and size can be ignored [28]. Figure 5 also shows the horizontal supports used to support the vertical blades. The curved blades category currently contains the phi-rotor configuration. An early example of this type of design is shown in Figure 6. Several support structures exist for this type of shape, namely the guy-wired, cantilevered, and fixed on tower arrangements. The wind turbine displayed in Figure 6 is supported by guy cables and X-shaped struts are also added inside the rotor to further support it. However, it was found that the added costs and drag induced effects caused by the presence of the struts had a negative impact on the overall design performance. Thus, they were removed from subsequent designs [17].

Another Darrieus VAWT model with curved blades configuration is shown in Figure 7. It has a 19 m long diameter and a rated capacity of 300 kW at 20m/s. This wind turbine was equipped with SNLA 2150 airfoil profiles for the blades and a retrofit gearbox to increase the rotational speed of the turbine to 60 rpm. An extended height to diameter (EHD) iteration of the model was also designed to improve the rotor power output. By extending the rotor shaft rather than expanding the rotor diameter, the total swept area of the turbine could then be increased to improve performance and reduce bend-in-place static stresses. Unfortunately, this turbine never attained its rated capacity level during its operational time, due to overpredictions of onshore wind speed [29].



Figure 5: A 200 kW fixed pitch H-rotor built by Vertical Wind [27]

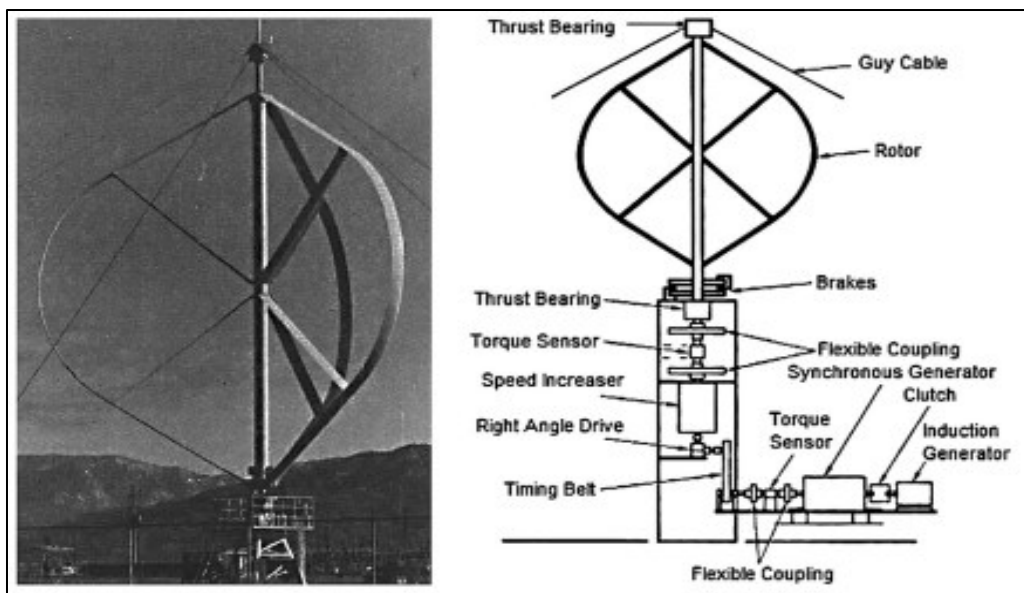


Figure 6: 17m Sandia guy-wired phi-rotor (left), Illustration showing major components (right) [17]



Figure 7: A 300 kW commercial Darrieus VAWT constructed by FloWind [29]

1.3.2.2 Darrieus Troposkien Wind Turbine

Amongst the different wind turbines shapes in the Darrieus category (such as Helical, H-rotor, etc...), the Troposkien shape is of interest in this work. Blackwell and Reis [30] described the Troposkien shape as “The shape assumed by the perfectly flexible cable of uniform density and cross section if its ends are attached to two points on the vertical axis and it is then spun at constant angular velocity about that vertical axis”. In addition to the previously defined ideal shape, different Troposkien blade geometries such as the catenary, parabola, modified and Sandia straight-circular-straight (S-C-S) configurations are described by Paraschivoiu using non-dimensional data sets and equations [31].

The ideal Troposkien shape, also called the “skipping-rope” shape, helps reduce the flatwise bending stresses on the turbine’s blades that are caused by the presence of centrifugal and gravitational forces. Designing the blades to approximate the ideal Troposkien configuration also helps increase the blades fatigue life. The Sandia straight-circular-straight (S-C-S) configuration, which is an approximation of the ideal Troposkien shape, is based on the computer code DMG. With the height and diameter of the rotor known, along with the upper and lower blade-to-tower angles, an appropriate S-C-S design for a given turbine’s rotor geometry can be generated using this program. As opposed to the computer program TROP, which was developed at an earlier time by Blackwell and Reis, the DMG program also took into account the effects of gravitational forces on the blades. However, TROP was still deemed a suitable code for approximating the S-C-S shape

of rotors with small diameters and high rotation rates, such as the Sandia 2m wind turbine model [32]. Since the centrifugal force acting on the blades of small-scale rotors is much larger than the gravitational force, the impacts of gravity induced bending stresses on the system can be ignored when compared to the effect of the centrifugal force [17]. It was demonstrated by Paraschivoiu [31] that the Sandia S-C-S shape is the most convenient Troposkien approximation for the blades when gravity effects are ignored. Furthermore, this configuration can also be easily manufactured due to its simple three sections geometry and behaves well structurally.

An example of Troposkien shaped Darrieus rotor is shown in figure 8. The VP100 model is a wind turbine with a rating of 60 kW and has a rotor diameter of 15m. It is equipped with three blades that are hinged at both ends and are made of an extruded aluminum alloy. The hinges are an important feature of this wind turbine, since they allow vibration in the rotor without creating stresses in the blades. Furthermore, due to the generator being located on the ground, it is much easier and therefore cheaper to conduct maintenance on this model compared to its HAWT counterpart [17].

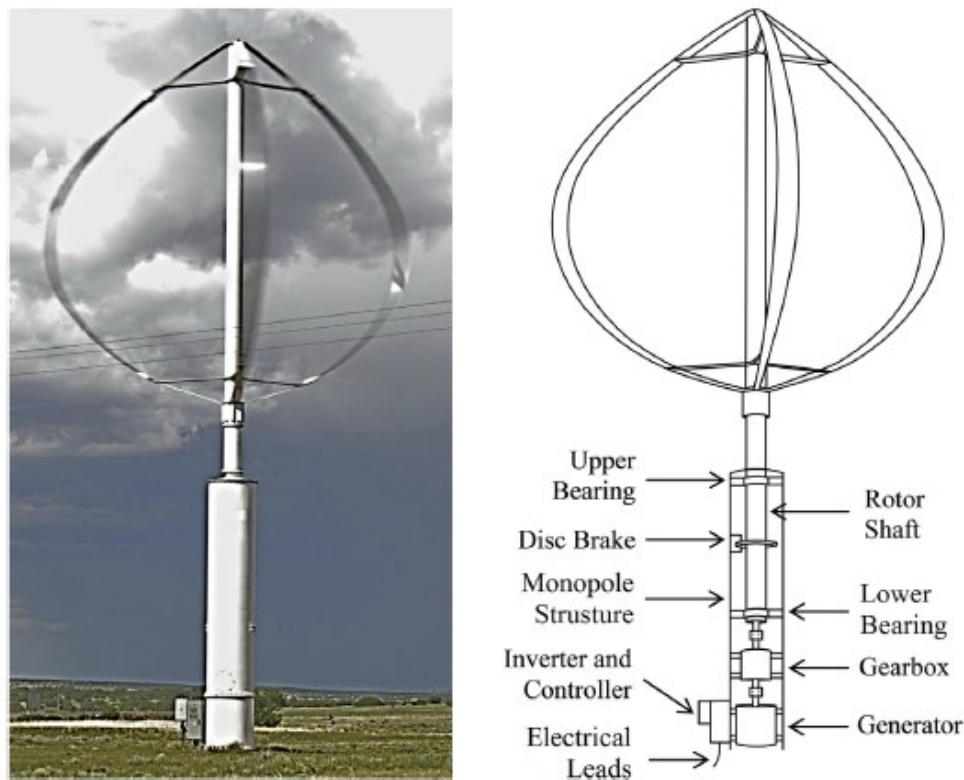


Figure 8: VMI 60 kW cantilevered (Troposkien) phi-rotor (left), artist impression of the VP100 components (right) [17]

1.4 VAWT Aerodynamics and Flow around Buildings

1.4.1 NACA 0012 Airfoil

Every numerical simulation detailed in this paper involves the same Darrieus Troposkien wind turbine rotor, which is based on the one presented in Sheldahl's work [33]. The airfoil used for the three blades' profiles is the symmetric NACA 0012 airfoil, which has a chord length of 58.77 mm and a thickness of 12%. It is said to be symmetric as its shape is the same on both sides of its centerline, as can clearly be seen in Figure 9.

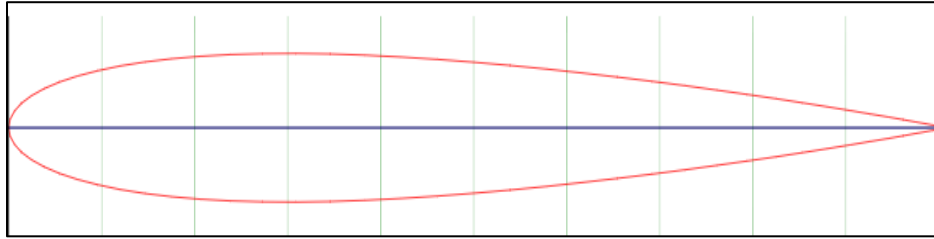


Figure 9: NACA 0012 airfoil

1.4.2 VAWT Aerodynamics

In order to properly analyze and prepare CFD simulations of VAWTs, it is important to have an appropriate knowledge of the aerodynamics and operation of these systems. As previously mentioned in section 1.3.2, the rotor blades go through different angle of attacks (AOAs) during a full rotation due to the particular orientation of their rotating motion with respect to the incoming wind flow. This negatively affects the blades capability to generate lift and therefore reduces the performance of the wind turbine. Darrieus wind turbines with Troposkien shape are no exception to this flaw. The constant change in AOA experienced by the rotor blades leads to flow reversal and boundary layer separation at high AOAs. Following flow separation, stall occurs, which leads to an important decrease in lift [12]. Furthermore, the blades located in the downstream area of the rotor are also affected by turbulent wakes formed upstream and by the effects of flow recirculation. Due to the turbulent nature of the rotor's downstream flow, accurately computing blades' aerodynamic forces in that area is one of the main challenges of VAWTs CFD simulations. From these different interactions, one can clearly see the complexity of the aerodynamics of VAWTs and Darrieus wind turbines. In order to improve the aerodynamic performance of VAWTs, Wang et al. [34] conducted 2D CFD simulations of a new type of VAWT which is equipped with airfoils capable of changing shape depending on their surfaces pressure distribution. Significant

improvements over the results obtained with the conventional VAWT were shown, including an important increase in maximum coefficient of power (C_p). Ma et al. [35] worked on the development of an automatic airfoil profile optimization system for VAWTs, with the goal of improving the power performance of these wind turbines. By combining results from 3D CFD simulations and the use of the Multi-Island Genetic Algorithm for airfoil optimization, they successfully improved the tested VAWT's power coefficients for Tip Speed Ratios (TSRs) ranging from 0.4 to 1.5 by employing optimized blades.

Figure 10 shows a section view of a typical Darrieus wind turbine rotor with three blades, along with the different aerodynamic forces acting on these blades at various positions. From looking at each blade in the figure, one can see that there are 3 velocity components describing both the wind and blade motion at each location along the circular path. The “U” component refers to the free stream wind velocity, whereas “ ωr ” describes the tangential velocity of the blade. The relative wind velocity “W” is derived from the other 2 components, and vary in magnitude and direction along the blade's path. When the rotor rotates at a constant angular velocity, the magnitude of the blade's tangential velocity remains the same. It is important to mention that for Darrieus Troposkien wind turbine rotors, the section view shown in Figure 10 correctly demonstrates the different aerodynamic forces and velocities experienced by the blades at the center of the rotor. This is where the radius is maximum due to the “skipping rope” Troposkien rotor design.

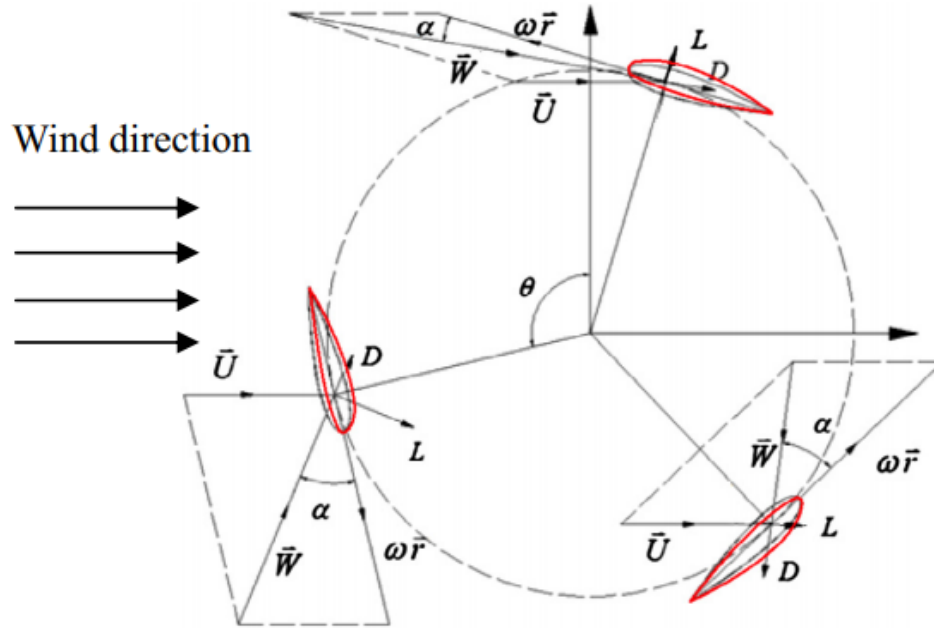


Figure 10: Darrieus wind turbine blades section view [34]

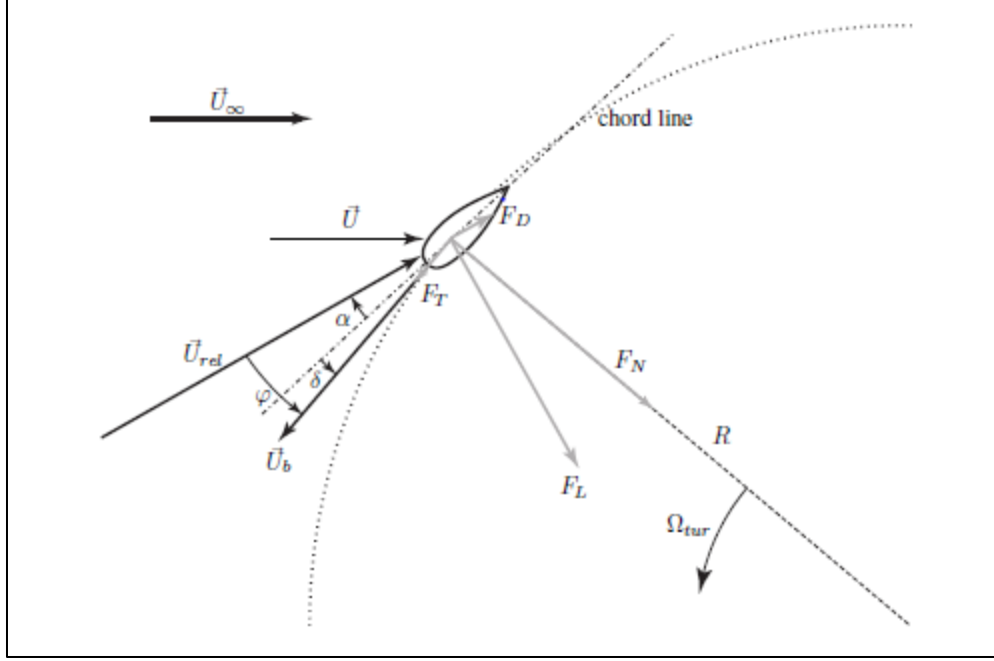


Figure 11: Aerodynamic forces acting on the blade [36]

The magnitude of the lift and drag forces, which are caused by the variation in pressure across the blade's surface, vary depending on the blade's AOA and the magnitude of the relative wind velocity. Furthermore, the drag force always acts in the direction of the relative wind velocity. Figure 11 also shows the tangential force F_T and the radial (normal) force F_N acting on the blade, which are both obtained by breaking down the lift and drag forces resulting force. The tangential force F_T produces the useful torque and the radial force F_N causes blade loading.

In their study of the three-dimensional unsteady aerodynamics of a Darrieus rotor blade, Balduzzi et al. [37] mentioned that in order to properly capture the complex aerodynamic features of the Darrieus rotor flows (such as blade tip flows and dynamic stall), the use of 3D CFD simulations over 2D ones is essential. Since these phenomena (and consequently their effects) strongly vary in space and time, the accuracy of 2D simulations in predicting the behavior of these flows may not be acceptable. It is for this reason that the simulations described in this thesis are all done using 3D geometry.

With the ongoing increase in computers' memory size and processing power, CFD simulations continue to offer a cheaper alternative solution to wind tunnel testing and other experimental data gathering methods. Whether it is used to conduct multiple analyses of a VAWT's performance under different unsteady wind conditions, or to carry parametric studies, the CFD method is able to provide accurate information of the flow's behavior and its impacts on VAWTs' performance in a progressively quicker timeframe. This data can then be used to optimize the designs of VAWTs and improve their efficiency.

1.4.3 Wind Flow around Buildings

Amongst the many building geometries and configurations considered in wind engineering research, the isolated cubic building case is one of the most studied combination in the field. Its simple geometry and complex flow behavior are often mentioned to explain this fact [41]. As the shape of the studied building in this thesis' work is also cubic, it is essential to know the flow phenomena present around these types of buildings. Figure 12 shows a schematic of the flow field around these structures, whereas Figure 13 displays numerically obtained time-averaged streamlines for a building immersed in a turbulent flow case, using an improved $k-\omega$ turbulence model. From these figures, one can see the main vortex formations around the structure, such as horseshoe vortices forming on both sides of the building. These are due to flow separation near both of the connections between the building side faces and the ground. Furthermore, flow recirculation on top of the building, as well as the formation of vortices behind it, can also clearly be seen in Figure 13. Flow separation occurs on top of the building, which causes the aforementioned recirculation. A standing vortex can also be observed directly in front of the windward side of the structure in Figure 13.

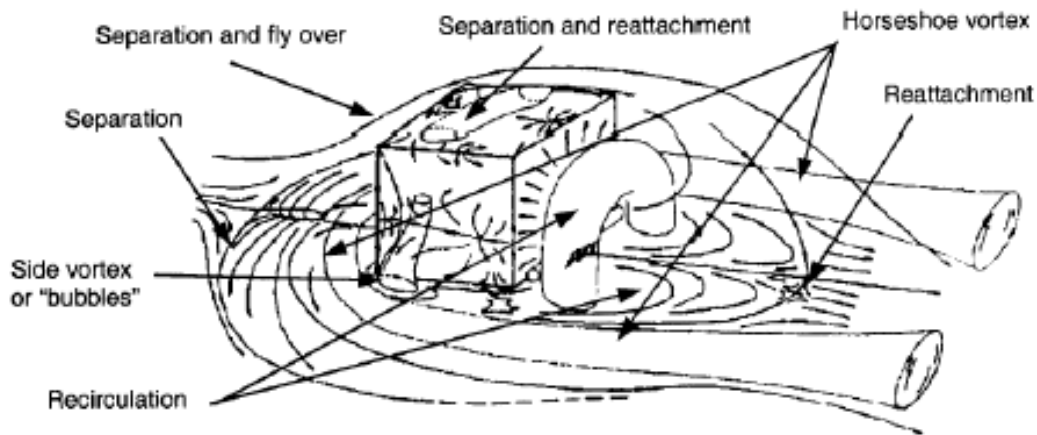


Figure 12: Flow field schematic for a cubic building under turbulent flow conditions [41]

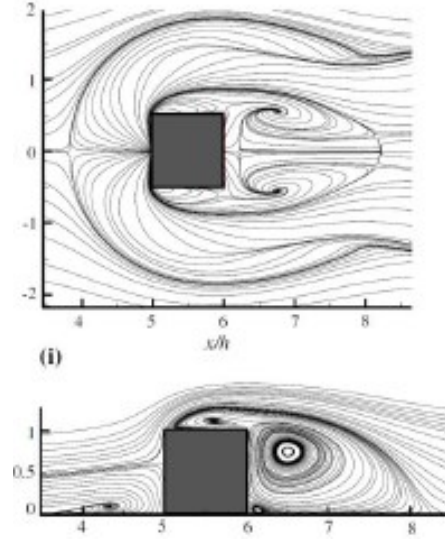


Figure 13: Time-averaged streamlines for a cubic building case using an improved $k-\omega$ turbulence model [41]

One of the main challenges faced by the wind turbine research community is investigating the impacts of wind flows around buildings on the power producing capabilities of rooftop mounted small-scale wind turbines [38]. It is desired to appropriately position and design the turbines so they can operate in the most efficient manner inside the accelerated wind region on the building's rooftop. The most commonly used numerical tool to acquire data in the fields of building aerodynamics and urban wind energy is CFD, as it is able to accurately simulate the complex urban flows present around buildings and wind turbines. The turbulence models used are carefully selected through validation processes that are based on available experimental data. Toja-Silva et al. [39] conducted a number of CFD simulations of the wind flow around an isolated building and compared their results with experimental data obtained during wind tunnel tests. It is important to mention that since the goal of their work was to analyze the characteristics of the flow for the purpose of wind energy exploitation, their analysis was focused on the building's roof and the flow recirculation occurring there. One of the objectives of this work was to evaluate the capability of several Reynolds-Averaged Navier-Stokes (RANS) turbulence models to reproduce experimentally obtained data. Both a qualitative approach and a quantitative approach were used in the analysis. The former focused on the flow's behavior by looking at the wind direction and the recirculation distance above the roof, while the latter examined the accuracy of the streamwise velocity and turbulent kinetic energy numerical results. Figure 14 shows a turbulent kinetic energy ' k ' contour taken at the center of the domain for one of the cases. All the peak values of ' k ' are located around the center of the building's roof, which is the best quantitative agreement obtained with experimental data. The contour was obtained using an MMK model with Bechmann coefficients.

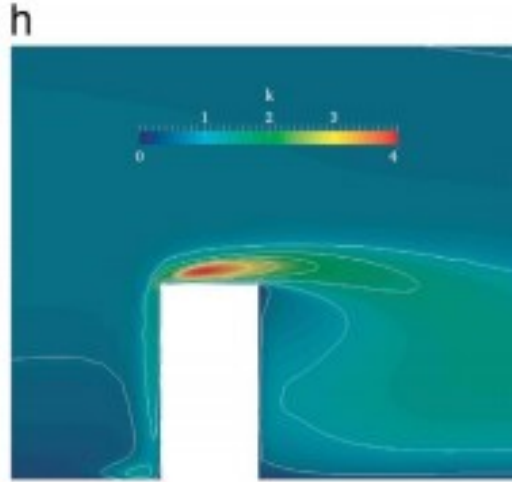


Figure 14: Turbulent kinetic energy (m^2/s^2) contour obtained with an MMK-Bechmann RANS turbulence model [39]

In their numerical study of the relationship between the power generation capability of a small-scale wind turbine and its height location above a cubic building, Micallef et al. [40] showed that the effects of the turbine's and building's presence on the surrounding wind flows are linked and impact performance differently depending on the tested configuration. Figure 15 displays velocity contours for 2 different vertical positions of the selected turbine above the building. The atmospheric boundary layer profile is the same for both positions and the wind direction is from right to left. Furthermore, contour zones colored in red corresponds to the highest velocities, whereas zones colored in blue show areas of low wind speeds. When comparing both cases, it is obvious that the recirculation zone behind the building is larger for the case where the turbine is lower and positioned inside another recirculation zone above the structure. Knowing that both recirculation zones are caused by the building itself, the existence of relationships between the turbine's and building's effects on the wind flows mentioned previously is clear. Such results further emphasize the importance of conducting combined building and turbine simulations.

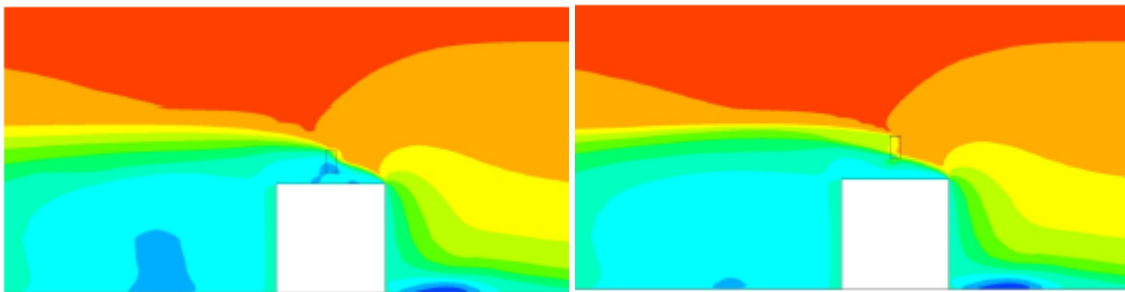


Figure 15: Velocity contours of two cases with different turbine's heights above a cubic building [40]

CHAPTER 2: COMPUTATIONAL METHODOLOGY DESCRIPTION

2.1 Wind Profile and Wind Turbines Performance Equations

2.1.1 Wind Profile Equation

The definition of appropriate boundary conditions is an important step in the CFD workflow. When the numerical simulations involve atmospheric flow, a critical boundary condition to consider is the wind profile equation, which describes the relationship between the wind speed and height [42]. In the context of the work presented in this thesis, this equation is only considered in cases where the building and a roof mounted turbine are introduced. The selected wind profile equation is the following:

$$V_z = V_t * \left(\frac{Z}{H_t}\right)^{0.31} \quad (2.1)$$

This equation is applied at the velocity inlet boundaries of building-mounted wind turbines simulations. It is derived from the mean wind velocity (U_z) equation used by weather stations to report local wind behavior [43]. The resulting wind profile is also referred to as “Atmospheric boundary layer (ABL)” in the literature. In this particular formulation, “ Z ” refers to the height measured from the ground (in meters), “ V_t ” is the wind speed at the middle of the rotor, “ H_t ” is the height of the middle of the rotor from the ground and “ V_z ” is the calculated wind speed at height Z .

2.1.2 Tip Speed Ratio

An important design parameter to consider in wind turbine performance analyses is the tip speed ratio, or “TSR”. It is defined as the ratio of the speed of the rotor blade’s tip to the free stream wind speed [44]. The equation describing this relationship is the following:

$$\lambda = \frac{\omega R}{V_t} \quad (2.2)$$

Where “ λ ” is the dimensionless tip speed ratio value, “ ω ” is the angular velocity of the rotor with units of rad/s, “ R ” is the radius of the rotor in meters and “ V_t ” is the free stream speed at the middle of the rotor.

2.1.3 Power Coefficient

The power coefficient “ C_P ”, also known as the rotor efficiency, is the dimensionless ratio of the power extracted by the wind turbine to the energy available in the wind stream [44]. It is a key parameter in assessing wind turbine performance and is limited by the theoretical Betz limit value of 0.5926. In practice however, wind turbines cannot reach this limit due to inefficiencies (such as gearbox, finite wings and generator related losses) that adversely affect the power extraction process. The power coefficient can be described as a product of the tip speed ratio and the moment coefficient, as shown in equations (2.3) and (2.4):

$$C_P = C_M * \lambda \quad (2.3)$$

$$C_P = \frac{M}{(0.5\rho V_t^2) * A_c * R} * \frac{\omega R}{V_t} \quad (2.4)$$

$$C_P = \frac{M\omega}{0.5\rho V_t^3 A_c} \quad (2.5)$$

Where “ M ” is the total instantaneous torque acting on the rotor blades, “ ρ ” is the air density and “ A_c ” is the cross-sectional area of the wind turbine. The moment coefficient is not constant, as it varies directly with the total torque applied on the turbine’s blades. Also, in practice, the tip speed ratio does not remain constant as well due to the erratic behavior of turbulent wind and the limitations of control systems. This can affect wind turbine performance due to the direct relationship between TSR and C_P , as can be seen from Figure 16.

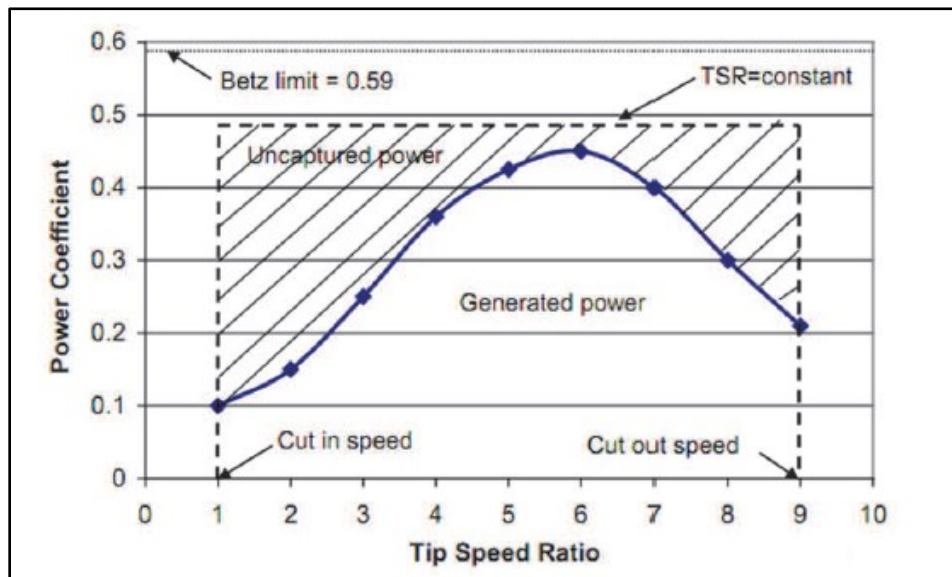


Figure 16: C_P versus TSR curve for a two bladed wind turbine [44]

2.2 Meshing Methodology

The first important pre-processing step of any CFD simulation is the mesh generation. The quality of the mesh is an important factor in ensuring proper convergence and accuracy of the final solution. In Star CCM+, mesh metrics such as skewness angle and volume change, are critical parameters to consider when evaluating mesh quality [45]. The volume change metric refers to the ratio of any given cell volume to its largest neighbor's volume. To maintain solver stability and increase accuracy, it is important that no cell bears a volume change equal to or lower than 0.01. The skewness angle metric reflects the ability of two connected cells to allow proper diffusion of flow quantities through their connecting face without these quantities becoming unbounded. This metric is defined in Star CCM+ [45] as the angle between the face area vector (face normal) and the vector connecting the two cell centroids. Cells with a skewness angle higher than 85 degrees are considered bad cells and can lead to interpolation errors. All of the meshes presented in this work maintain an acceptable skewness angle and a volume change metric above 0.01.

There are two types of mesh, structured and unstructured. Unstructured grids are easier to generate on complex geometries. However, since their elements have no repeating patterns, information relating to their connectivity needs to be kept in memory explicitly. Additional computational costs are therefore involved due to the extra memory used for storing. Furthermore, this type of mesh can also lead to more numerical dissipation. Unstructured meshes are composed of 2D triangular elements and 3D tetrahedral elements of various shapes. Structured grids on the other hand are composed of 2D quadrilateral elements and 3D hexahedral elements. In such meshes, grid nodes are determined by i , j and k indexes and are ordered in a repeating pattern. This leads to faster communication between neighboring nodes when compared with the unstructured approach [46][47]. It is also possible to stretch the grid in any specific direction in order to refine the mesh in areas of the flow where large gradients are expected. Doing so increases the accuracy of the computed flow solution and can reduce computational time.

Hybrid meshes are used in all of the CFD simulations presented in this work. This type of mesh is a combination of structured and unstructured meshes, where prism cells are present in the viscous region (the area of interest) and tetrahedral cells populate the more inviscid parts of the flow, away from the walls. Hybrid meshes are commonly used in viscous CFD cases due to their greater ability to control element sizes in areas of interest, such as near-wall regions. This method is very effective for meshing airfoil geometry [48]. In each simulation, a structured mesh approach is applied around the wind turbine's blades to appropriately simulate the viscous effects present inside the different boundary layers. Outside these refinement zones, tetrahedral unstructured cells are

generated to better capture the cylindrical geometry of the domain's rotating region. Further details on the applied meshes are given in their respective chapters' sections.

2.3 Wall Treatment Approach

It is well known that walls are sources of vorticity in turbulent flows. Therefore, it is important to accurately capture the effects of their presence on the flow and the various parameters of turbulence. This is especially true in close proximity to the walls, where the fluid's viscosity acts as a dominant factor in describing the flow's behavior [49]. Furthermore, correctly resolving the boundary layer is critical for the computation of forces and moments acting on the wind turbine's blades. In Star CCM+ [45], the non-dimensional y^+ parameter, which is an indication of wall distance, is defined in the following way:

$$y^+ = \frac{\rho y u^*}{\mu} \quad (2.6)$$

Where μ is the dynamic viscosity of the fluid, y is the normal distance from the wall to the centroid of the first cell, ρ is the fluid density and u^* is the reference velocity given by:

$$u^* = \sqrt{\frac{\tau_\omega}{\rho}} \quad (2.7)$$

Where τ_ω is the wall shear stress. In Star CCM+, the inner region of the boundary layer is divided into three sublayers. They are shown in Figure 17.

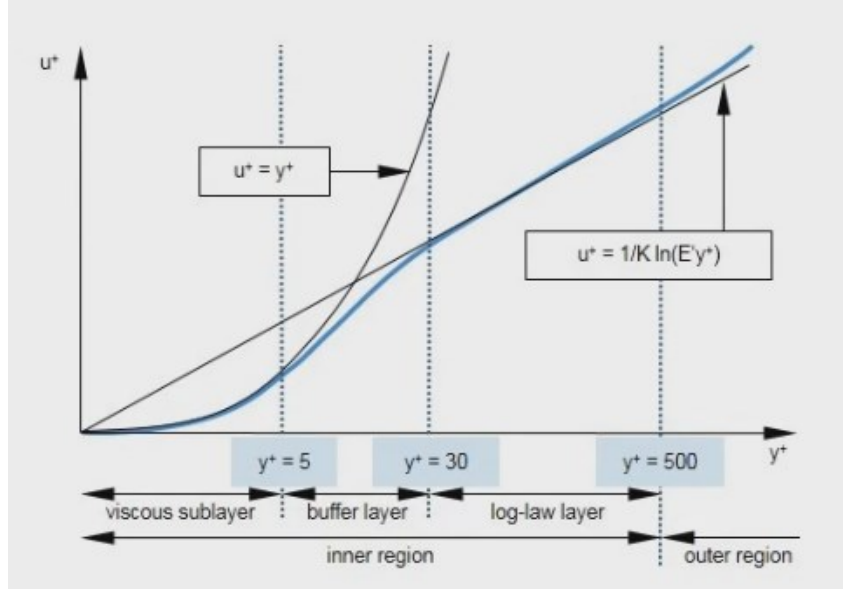


Figure 17: Boundary layer structure in Star CCM+ [45]

The furthest layer from the wall is the log-law sublayer, where the flow is equally impacted by viscous and turbulent effects. The closest layer to the wall is the viscous sublayer, where the flow is most affected by the effects of viscosity. The flow velocity inside this sublayer changes rapidly from the wall, where the no-slip condition is applied. Star CCM+ offers three different approaches to near wall modeling [45]:

1. High y^+ wall treatment ($y^+ > 30$)
2. Low y^+ wall treatment ($y^+ \sim 1$)
3. All y^+ wall treatment

In the high y^+ wall treatment approach, semi empirical wall functions are used to obtain the boundary conditions for the continuum equations. In this method, the buffer layer and the viscous sublayer are not resolved. Instead, the physics of the flow inside these layers is modeled to behave in a similar manner to the flow physics present in the log-law layer. In order to apply this method, the near wall cell centroid must follow a y^+ requirement of $y^+ > 30$, which can significantly reduce the number of elements in the near-wall region of the mesh. This wall treatment approach is recommended for cases with high Reynolds number flows that do not require fully resolving the boundary layer and computing wall forces.

The low y^+ wall treatment method completely resolves the boundary layer and is much more accurate than the previously described high y^+ method. In this approach, the near wall cell centroid is located inside the viscous sublayer at a $y^+ \sim 1$, which allows the transport equations to be computed all the way to the wall cell. Enforcing this low y^+ criteria on the first wall cell requires

the mesh to be adequately refined near the wall, which then increases the total amount of mesh elements. This method is suggested for flows that involve high levels of boundary layer separation due to adverse pressure gradients. It is also recommended for the computation of forces and moments acting on wall surfaces. In addition to the higher computational costs involved in using this approach, this wall treatment can be difficult to apply on geometries of various scales and complexities, due to its strict y^+ requirement. Since the combined building and wind turbine simulations described in this work involve computational domain geometries of this nature, generating a pure low y^+ mesh on each wall surface boundary present in these domains is not feasible.

In order to maintain the level of physical accuracy offered by the low y^+ approach on the wind turbine blades' surfaces without creating an unnecessarily large mesh, the all y^+ wall treatment approach is used for all cases. Star CCM+ describes this method as ‘‘a hybrid treatment that emulates the low- y^+ wall treatment for fine meshes, and the high- y^+ wall treatment for coarse meshes.’’ [45]. This approach therefore allows for larger near-wall cells on the building and bottom walls. It also uses a blending function to compute turbulence quantities for cells located in the buffer region of the boundary layer, which helps the calculation of an acceptable flow solution for these elements. Figure 18 illustrates this method, and equation (2.8) details the blending function g .

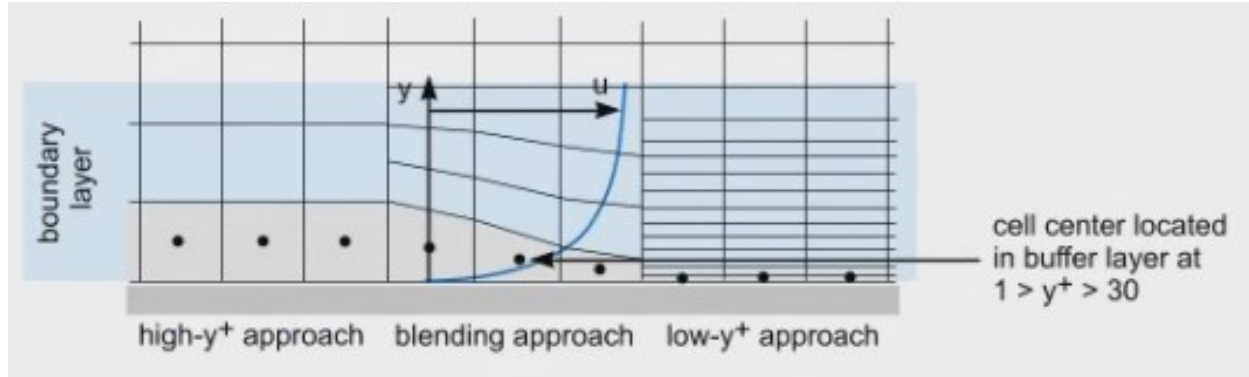


Figure 18: All y^+ wall treatment [45]

$$g = \exp\left(-\frac{Re_y}{11}\right) \quad (2.8)$$

Where $Re_y = \frac{\sqrt{k}y}{\nu}$ is a Reynolds number dependent on wall distance.

2.4 Turbulence Modeling Approach

Turbulence flow modeling is a critical part of the CFD methodology. Indeed, most of the flows found in engineering applications (and in nature itself) are turbulent. Hinze [50] defines turbulence as “an irregular condition of flow in which the various quantities show a random variation with time and space coordinates, so that statistically distinct average values can be discerned.”. These random fluctuations are caused by the presence of eddies of different sizes in the flow and their various interactions. They are also responsible for the diffusive behavior of turbulent flows, due to their characteristic swirling motions.

Three different approaches are available in CFD to model turbulence. In this section, information about these methods is presented, along with a description of the selected turbulence model used in all the simulated cases shown in this work. The aforementioned approaches are listed below:

1. Reynolds-Averaged Navier-Stokes (RANS)
2. Large Eddy Simulations (LES)
3. Direct Numerical Simulations (DNS)

2.4.1 Reynolds-Averaged Navier-Stokes (RANS) Approach

The relations that describe conservation of mass, momentum and energy in fluid mechanics are widely known and established. Amongst these governing equations, the ones associated with conservation of momentum are also known as the Navier-Stokes equations. When a turbulent flow is considered, the various flow quantities present in the governing equations, such as velocity and pressure, are instantaneous in nature. They completely describe the flow’s behavior, but cannot be solved for directly due to the random fluctuations involved in their computations.

The Reynolds decomposition process, established by Osborne Reynolds, is the first step of the RANS method. According to this process, each of the instantaneous variables in the governing equations can be separated into two components: a mean part and a fluctuating one with zero mean [51]:

For the velocity components:

$$u_i = \bar{u}_i + u_i' \quad (2.9)$$

For other quantities, such as pressure:

$$P = \bar{P} + P' \quad (2.10)$$

Where u_i and P are instantaneous quantities, \bar{u}_i and \bar{P} are the mean parts of the variable and u_i' and P' are the fluctuating components of the quantity. The purpose of this process is to form governing equations that only contain mean quantities, independent of the turbulent fluctuations. After applying the decomposition process shown in equations (2.9) and (2.10) to the conservation of mass and momentum relations, Reynolds performed a time-average operation on them as well. In doing so, the average form of the conservation of mass and Navier-Stokes equations were obtained. These equations, shown below in Cartesian form, are also known as the Reynolds-Averaged Navier-Stokes (RANS) equations:

$$\frac{\partial \rho}{\partial t} + \frac{\partial}{\partial x_i} (\rho u_i) = 0 \quad (2.11)$$

$$\frac{\partial (\rho u_i)}{\partial t} + \frac{\partial}{\partial x_j} (\rho u_i u_j) = -\frac{\partial p}{\partial x_i} + \frac{\partial}{\partial x_j} \left[\mu \left(\frac{\partial u_i}{\partial x_j} + \frac{\partial u_j}{\partial x_i} - \frac{2}{3} \delta_{ij} \frac{\partial u_l}{\partial x_l} \right) \right] + \frac{\partial}{\partial x_j} (-\rho \overline{u_i' u_j'}) \quad (2.12)$$

Where all the pressure and velocity terms involved are replaced by their mean value equivalents. Also, equations (2.11) and (2.12) assume a viscous and compressible fluid. The last term on the right-hand side of equation (2.12) however is not composed of mean velocity components. This expression, $-\rho \overline{u_i' u_j'}$, is known as the Reynolds stress tensor. It represents the effects of turbulent motions (eddies) on the mean flow stresses. Unfortunately, this tensor effectively adds 6 independent unknowns to the equations due to its three-dimensional nature, which prevents the computation of the RANS equations. This issue is known as the turbulence closure problem. The Reynolds stress tensor is defined in the following way:

$$\tau = -\rho \begin{bmatrix} \overline{u'u'} & \overline{u'v'} & \overline{u'w'} \\ \overline{v'u'} & \overline{v'v'} & \overline{v'w'} \\ \overline{w'u'} & \overline{w'v'} & \overline{w'w'} \end{bmatrix} \quad (2.13)$$

Many turbulence models were created in an attempt to model the Reynolds stress tensor term and close the RANS system of equations. A total of 4 main categories of models were developed using the RANS approach:

1. Algebraic (zero-equation) models
2. One-equation models
3. Two-equation models
4. Stress transport models

The first 3 turbulence model categories use the concept of eddy viscosity and the Boussinesq approximation to attain closure, while the stress transport models directly compute the individual components of the Reynolds stress tensor using exact equations.

The Boussinesq approximation assumes that the momentum transfer caused by the turbulent eddies' interactions can be modeled with the concept of an eddy viscosity. It is analogous to how the momentum transfer resulting from the molecular interactions inside a gas can be related to a molecular viscosity. This assumption is a well established idea in RANS turbulence modeling and relates the notion of eddy viscosity to the effects of turbulence (Reynolds stresses) and the mean flow behavior. The Boussinesq approximation provides a new equation for turbulence closure and is formulated in the following way:

$$\tau_{ij} = 2\nu_t S_{ij} - \frac{2}{3}k\delta_{ij} \quad (2.14)$$

Where τ_{ij} is the Reynolds stress tensor, ν_t is the eddy viscosity, k is the turbulent kinetic energy, δ_{ij} is the Kronecker delta and $S_{ij} = \frac{1}{2}\left(\frac{\partial \bar{u}_i}{\partial x_j} + \frac{\partial \bar{u}_j}{\partial x_i}\right)$ is the strain-rate tensor of the mean field.

2.4.2 The k - ω SST Turbulence Model

The standard k - ω turbulence model, along with its Shear-Stress Transport (SST) variant, are two-equation models that compute two scale quantities of turbulence using transport equations. These quantities are the turbulent kinetic energy k and the specific dissipation rate ω . The latter is defined in the following way:

$$\omega \sim \frac{\varepsilon}{k} \quad (2.15)$$

Where ε is the turbulent dissipation rate. The k - ω models are based on the RANS approach to turbulence modeling and the Boussinesq approximation. Thus, their goal is to solve transport equations for the aforementioned turbulent scale quantities in order to compute the eddy viscosity. Wilcox, who developed the original k - ω turbulence model [52], reported that his model produced more accurate results for boundary layers containing adverse pressure gradients, when compared to k - ε models.

A known shortcoming of the original k - ω model is the sensitivity of boundary layer calculations to values of ω in the free-stream. As a result, internal flows are really sensitive to inlet boundary conditions, an issue that is not present in k - ε models. It was Menter [53] that developed the SST approach to tackle this issue. The first step was to change the transport equation for ε , from the standard k - ε model, into a transport equation for ω using variable substitution. In doing so, a non-conservative cross-diffusion term appeared in the equation. It was found that adding this term to the transport equation could potentially force the k - ω model to yield the same results as the k - ε model. Since it was preferable to keep the original k - ω approach close to the wall, due to its superior performance over the k - ε model in that region, Menter proposed to use a blending function that would include the cross-diffusion term in the far-field, but not close to the wall. In doing so, he came up with a model that combined the k - ε approach in the outer free shear flow region and the k - ω model close to the wall, inside the boundary layer. This approach essentially solved the sensitivity issue of the original k - ω model. The Menter k - ω SST model is widely used in the aerospace industry and is appropriate for cases where a complete resolution of the boundary layer is required.

From the Star CCM+ theory guide [45], the following transport equations for the turbulent kinetic energy k and the specific dissipation rate ω are given for the Menter k - ω SST turbulence model:

$$\frac{\partial(\rho k)}{\partial t} + \nabla \cdot (\rho k \bar{\mathbf{v}}) = \nabla \cdot [(\mu + \sigma_k \mu_t) \nabla k] + P_k - \rho \beta^* f_{\beta^*} (\omega k - \omega_0 k_0) + S_k \quad (2.16)$$

$$\frac{\partial(\rho \omega)}{\partial t} + \nabla \cdot (\rho \omega \bar{\mathbf{v}}) = \nabla \cdot [(\mu + \sigma_\omega \mu_t) \nabla \omega] + P_\omega - \rho \beta f_\beta (\omega^2 - \omega_0^2) + S_\omega \quad (2.17)$$

Where μ is the molecular dynamic viscosity, $\bar{\mathbf{v}}$ is the mean flow velocity, P_k and P_ω are production terms, σ_k and σ_ω are model coefficients, f_{β^*} is the free shear modification factor, f_β is the vortex-stretching modification factor, S_k and S_ω are source terms, β and β^* are model coefficients and k_0 and ω_0 are ambient turbulence values. The aforementioned production terms are defined in the following ways:

$$P_k = G_k + G_{nl} + G_b \quad (2.18)$$

$$P_\omega = G_\omega + D_\omega \quad (2.19)$$

Where G_k is the turbulent production term, G_{nl} is the non-linear production term, G_b is the buoyancy production term, G_ω is the specific dissipation rate production term and D_ω is the cross-diffusion term that appears in the specific dissipation rate's transport equation for the Menter $k-\omega$ SST model:

$$D_\omega = 2\rho(1 - F_1)\sigma_{\omega_2} \frac{1}{\omega} \nabla k \cdot \nabla \omega \quad (2.20)$$

Where F_1 is the blending function that includes the cross-diffusion term in the far-field, but not close to the wall and σ_{ω_2} is a model coefficient. The blending function F_1 and the shear stress transport blending function F_2 , the latter being found in the turbulent time scale definition of this model [45], are defined in the following ways:

$$F_1 = \tanh \left(\left[\min \left(\max \left(\frac{\sqrt{k}}{0.09\omega d}, \frac{500\nu}{d^2\omega} \right), \frac{2k}{d^2 CD_{k\omega}} \right) \right]^4 \right) \quad (2.21)$$

$$F_2 = \tanh \left(\left(\max \left(\frac{2\sqrt{k}}{\beta^*\omega d}, \frac{500\nu}{d^2\omega} \right) \right)^2 \right) \quad (2.22)$$

Where ν is the kinematic molecular viscosity, $CD_{k\omega} = \max \left(\frac{1}{\omega} \nabla k \cdot \nabla \omega, 10^{-20} \right)$ is a cross-diffusion coefficient and d is the wall distance. The Menter $k-\omega$ SST model is used in all of the simulations presented in this work.

2.4.3 Large Eddy Simulations

This approach to turbulence modeling considers that turbulent flows contain eddies of different time and length scales. The large scales of turbulence are directly resolved in this method, while the small scales are instead modeled. In doing so, the error in the turbulence modeling assumptions is not as great, as most of the turbulence in the flow is resolved. Also, it is assumed that smaller eddies follow simpler and more universal models due to their self-similarity, which makes them easier to model than large scale eddies. Most of the Reynolds stresses and flow momentum, mass and energy are contained in the large eddies, which is why this method's accuracy in describing the turbulence effects on the flow is considered greater than the simpler RANS models. However, when the same case is considered for both options, using this turbulence model can involve greater computational costs and can be more time consuming when compared to RANS models. Indeed, since the larger eddies tend to decrease in size as progress is made towards the wall, it is crucial for the mesh to reduce in size as well to keep up and allow for an accurate resolution of the flow.

2.4.4 Direct Numerical Simulations

Direct numerical simulation is the most complex turbulence solving method in CFD as it resolves the whole range of turbulence scales present in the flow directly, without any modeling involved. As a result, the computational costs associated with such an approach are too high to be applied to complex high Reynolds number flows. It is instead used to analyze turbulence in simpler flows, yielding results that are significantly more accurate than any other models present in the RANS or LES approach. The commercial CFD code Star CCM+ does not contain any DNS models [45].

2.5 Boundary Conditions

An important part of the CFD workflow is the selection of appropriate boundary conditions for the simulation domain. In order to ensure this step of the numerical setup is carried out properly, knowing the definitions and applications of these boundary conditions is crucial. This section describes the boundary conditions used for both the validation cases and the building mounted wind turbine cases.

2.5.1 Symmetry Plane Boundary condition

When the full geometry of the domain can be divided into two symmetrical parts and the flow's behavior is expected to be symmetrical about the same surface, the symmetry plane boundary condition can be used to reduce the size of the domain by half. It is applied on the symmetry plane surface and yields a flow solution that is identical to the one that would be obtained by mirroring the mesh about the symmetry plane. Furthermore, this boundary condition can also be used to model zero shear slip walls in viscous flows [45].

2.5.2 Velocity inlet Boundary condition

This boundary condition is used to establish the velocity and scale properties of the flow at the inlet(s) of the computational domain, if they are known prior to the calculations. The velocity inlet boundaries used for the validation cases employ a uniform velocity profile, whereas those present in the roof mounted wind turbine simulations utilize the wind profile equation mentioned in section 2.1.1 to create their velocity profiles (with the exception of the velocity inlets located at the top of the domains).

2.5.3 Pressure Outlet Boundary condition

The pressure outlet boundary condition defines a flow outlet where the pressure is specified. In Star CCM+, there are two possible options for boundary conditions at the domain's outlet: the outlet boundary condition, and the pressure outlet condition. The former is applied for cases where either the ratios of mass flow or the exit mass flow rates are known for each outlet boundaries before the simulation. The advantage of using the pressure outlet option over the outlet boundary condition is that the latter is not recommended for flows where recirculation could occur at the outflow boundary [45]. This is why the pressure outlet boundary condition is used for all of the presented simulations.

2.6 SIMPLE Pressure-Velocity Coupling Algorithm

The segregated flow solver, which uses the SIMPLE (Semi-Implicit Method for Pressure-Linked Equations) pressure-velocity coupling algorithm, is selected for all of the CFD simulations presented in this work. This solver computes the different solution variables (such as pressure and velocity) from the non-linear conservation equations of mass and momentum in an iterative manner. Every simulation detailed in this thesis solves the incompressible form of the Navier-Stokes equations, which is why this solver is used, as it is appropriate for flows that are either incompressible or with low compressibility [45]. Furthermore, as the equations only need to be loaded into memory one at a time with the segregated approach, it consumes less memory than the coupled approach. Indeed, the coupled flow solver computes the conservation equations simultaneously as a vector of equations. In this approach, the pressure is obtained from the continuity equation, the density is calculated from the equation of state and the velocity field is computed from the momentum equations.

The SIMPLE algorithm is also referred to as a predictor-corrector approach, where pressure is acquired from a pressure-correction equation. This equation is derived from the continuity and momentum equations such that by adjusting the pressure, a velocity field that satisfies continuity can be obtained.

This algorithm is suggested by Bedon [54] for conducting CFD simulations of wind tunnel testing on a Darrieus wind turbine due to the time step size and the flow's turbulent nature. In his work, only half the rotor was modeled, as is also the case for the validation simulations detailed in Chapter 3.

CHAPTER 3: METHODOLOGY VALIDATION

3.1 Model Geometry

The previously described methodology is used to conduct numerical simulations of the experiment done by Sheldahl [33] in Vought Corporation's low speed wind tunnel. The purpose of these simulations is to validate the aforementioned methodology by comparing the obtained numerical results with the corresponding experimental data. More specifically, experimentally obtained coefficients of power (C_p) from the tested Darrieus vertical-axis wind turbine model shown in Figure 19 are to be compared to numerically obtained data. In the experiment, the wind velocity profile upstream of the rotor in the wind tunnel is constant and the C_p results are gained at various tip speed ratios. This validation process was also carried out by Samson [8] and in a similar manner by Bedon [54]. In each simulated case, half of the rotor's geometry is used in order to take advantage of the turbine's symmetrical shape and apply a symmetry boundary condition at the bottom surface of the domain. Furthermore, doing this also helps reduce computational time. The turbine's rotor geometry is shown in Figure 20.

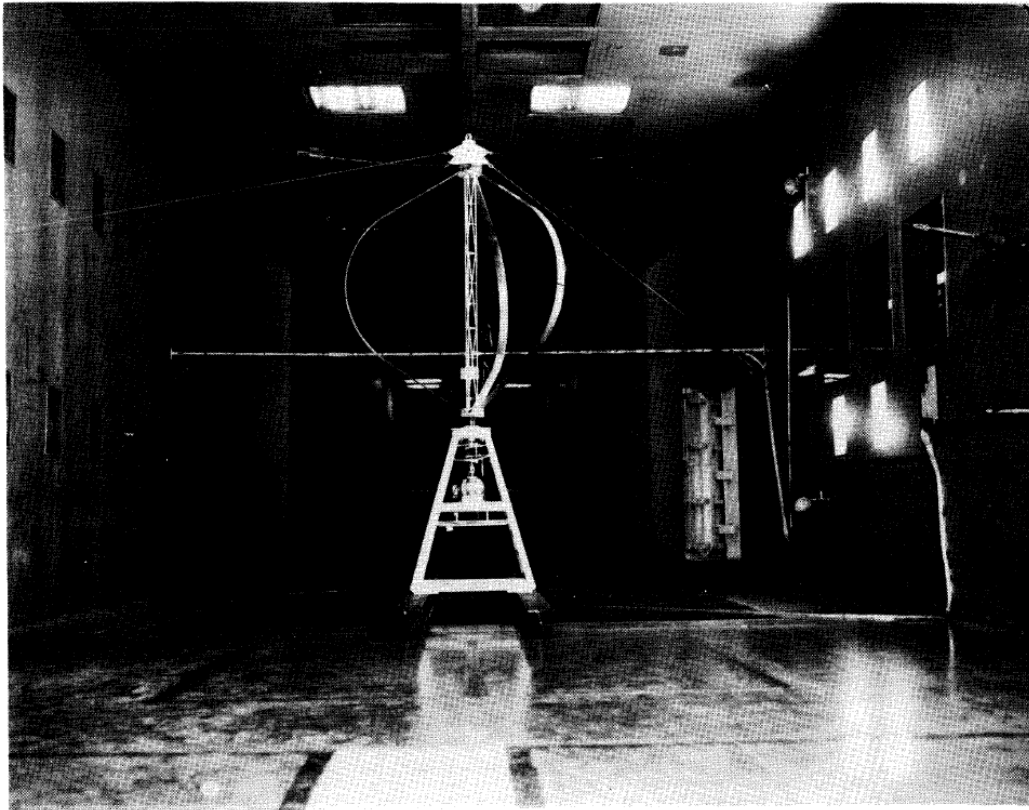


Figure 19: Sandia Darrieus VAWT 2m model inside the wind tunnel testing site [33]

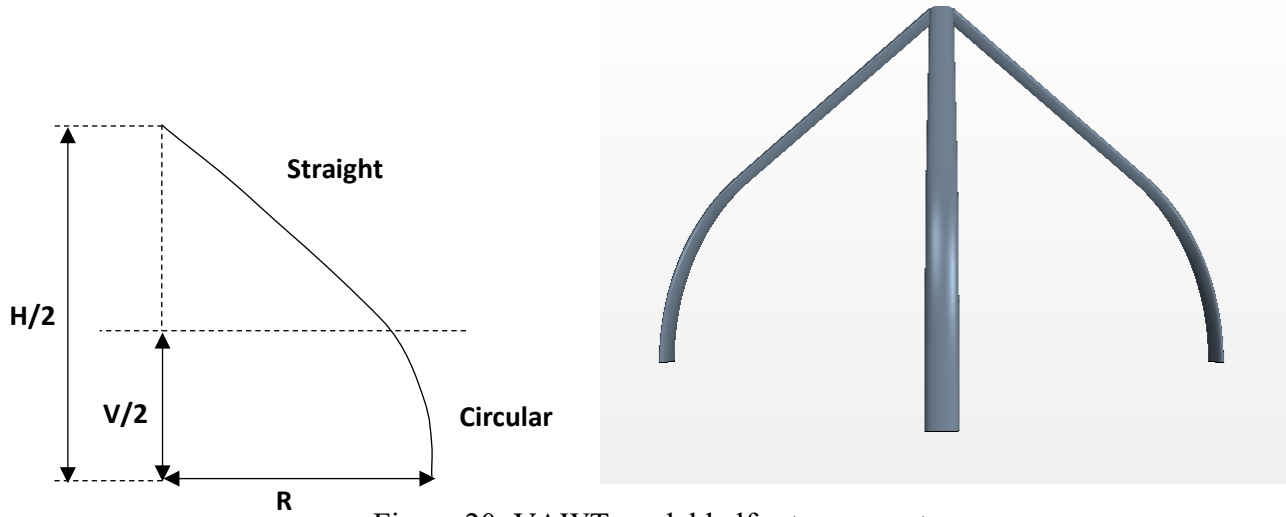


Figure 20: VAWT model half rotor geometry

The rotor blades follow a straight-circular-straight (SCS) pattern that is considered to be a good approximation of the Troposkien shape. Since no information was given about the rotor's central shaft geometry [33] and to avoid potential mesh cells quality issues due to the proximity of the shaft to the blade ends, it was deemed appropriate to not include the shaft in the model. This was also done in previous papers [8][54]. The maximum radius of the rotor, located at the center of the curve part of the blades, is 0.98m and the height of the curve part of the rotor blades is 0.5654m. The total height of the rotor is 2m. The previously shown NACA 0012 airfoil profile in Figure 9 is selected for the blades. The rotor used for wind tunnel tests used blades that were manufactured using 7075-T6 high-strength aluminum alloy. The curve part of the blades was formed from a flat ribbon [33].

Table 1: Important dimensions of the tested Sandia model

Important dimensions of the tested Sandia model	
Number of blades	3
Blade profile	NACA 0012
Blade pattern	Straight-Circular-Straight
R [m]	0.98
H [m]	2
V [m]	0.5654
C [m]	0.05877

Table 1 shows a summary of the key dimensions and parameters involved in the tested VAWT model. It is important to mention that the chord length C of the blades profile is also given in this table.

3.2 Computational Domain Geometry

The numerical domain of the simulation is composed of 2 sections, namely the static and rotating regions. The latter is shaped as a half-cylinder and is shown in Figure 21. Inside the rotating region is the turbine's rotor half, it is located at the center of the rotating region. A schematic of the side view of the domain is shown in Figure 22 along with a close up view of the rotating domain. The center of the rotor is 30m away from the static domain's inlet and 60m away from the outlet. The outlet distance is greater to avoid reverse flow effects on the rotor's performance. The width of the static region is 20m and its total height is 3m. It is also important to mention that the inlet is located to the right of the domain in the bottom figure. The computational domain's geometry is identical to the one used by Samson [8].

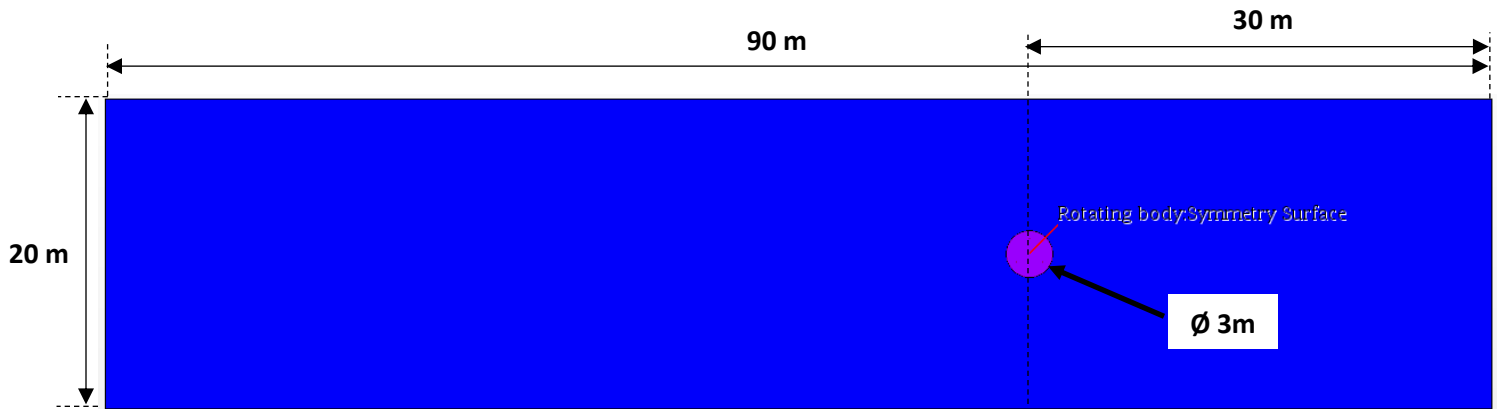


Figure 21: Bottom view of the computational domain

The rotating domain has a diameter of 3m, whereas the rotor's maximum diameter is of 1.96m at the static region's bottom symmetry surface.

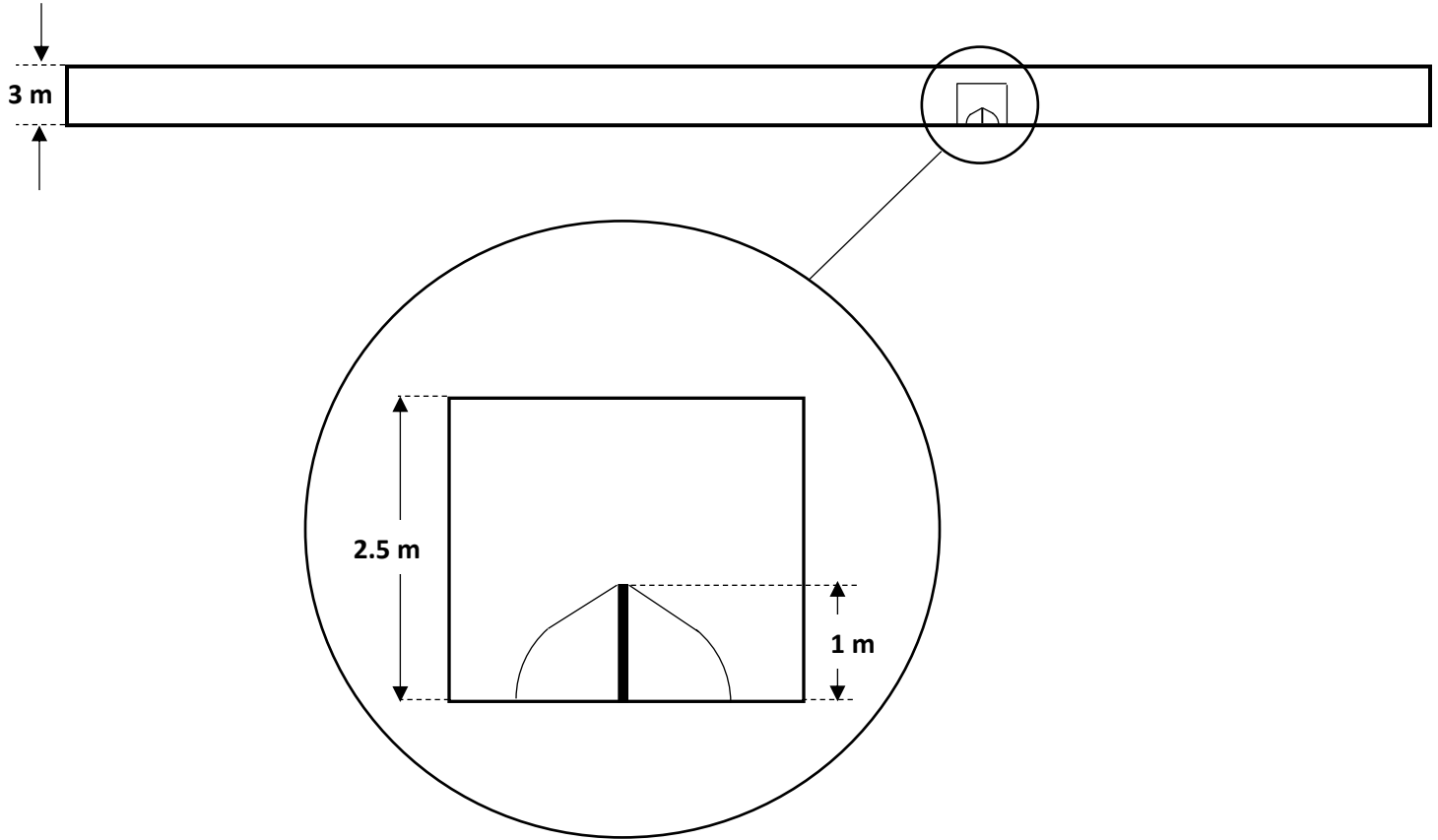


Figure 22: Right side view of the computational domain

3.3 Mesh Configuration

An unstructured mesh approach is applied for both the static and rotating regions' mesh in order to better capture the cylindrical shape of the rotating region. The mesh was generated using the ANSYS ICEM CFD meshing software and then imported in Star CCM+. This mesh is also described in Samson's work [8]. As shown in Figure 23 and in Figure 24, the volume cells are progressively refined as they approach the internal interface separating the rotating and static domain. The patch independent option is selected to generate both the static and rotating domain meshes. This method, combined with a small element growth rate of 1.01, ensures a smooth transition between both regions meshes by controlling the maximum cell size. A growth rate of 1.01 refers to an increase in 1% of cell edge size between each consecutive cell layer inside the volume mesh [8].

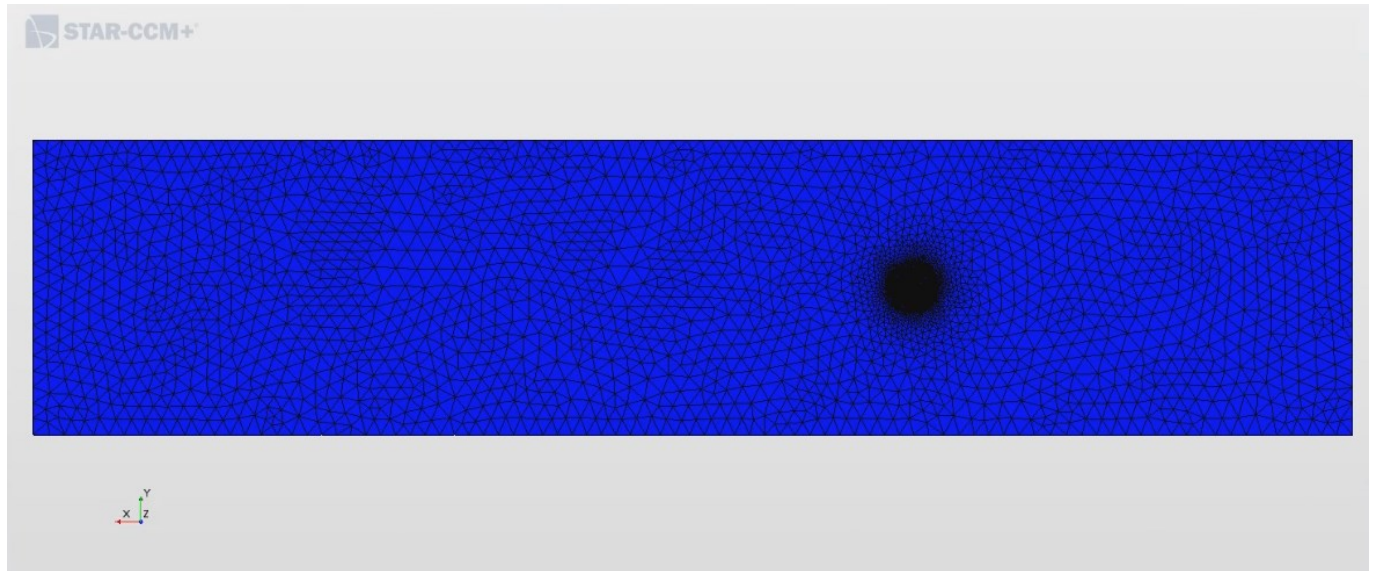


Figure 23: Bottom view of the static and rotating regions' mesh

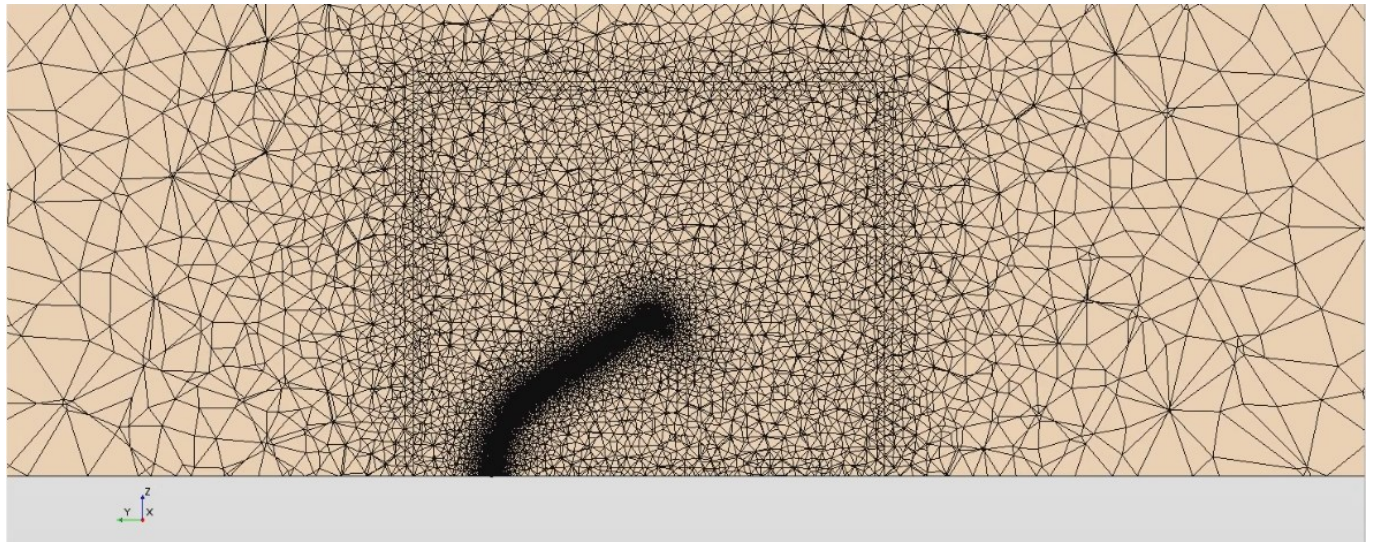


Figure 24: Cross-sectional front view of the mesh

The airfoil sections of the blades are divided into two parts during the meshing procedure; the leading edge and the trailing edge components. The bias factor option is applied to both parts to control the mesh density in these regions. A bias factor of 3 is used for the trailing edge section while a bias factor of 6 is applied to the leading edge [8]. Furthermore, in order to properly capture the behavior of the flow inside the boundary layer around the rotor blades, inflation layers were generated from each blades' surfaces. The thickness of the first layer corresponds to a low y^+ condition (~ 1) and allows for accurate resolution of near wall flow phenomenon such as separation.

To efficiently control the volume mesh parameters, close to the rotor blades' locations, mesh refinement regions positioned around each rotor blades are used. One of these three refinement zones can be seen in Figure 24. The volume meshes of these regions are populated by hexahedral cell elements. These cells are created from 2D quadrilateral elements and swept along the blades' surfaces. Such a procedure increases mesh quality around the blades and ensures that the distribution of prismatic cell elements is uniform. Figure 25 to 28 show the refinement around the blades in more detail. Also, in order to improve mesh quality at the trailing edge, a straight cut geometry is used for the airfoil profile where 5 same size elements are grown from the trailing edge tip surface [8]. A summary of important mesh parameters and their appropriate values is shown in Table 2.

Table 2: Mesh parameters and sizes

Mesh parameters and sizes	
Parameter	Value
Rotating domain interface element size	0.70 m
Static domain interface element size	0.75 m
Number of elements swept around each blade	300
Airfoil profile elements count	223
y^+ value at each blade surface	~ 1
Volume growth rate	1.01
Static domain volume cells count	230 000
Rotating domain volume cells count	4 million
Blade refinement zone volume cells count	1.6 million
Total mesh elements count	9 million

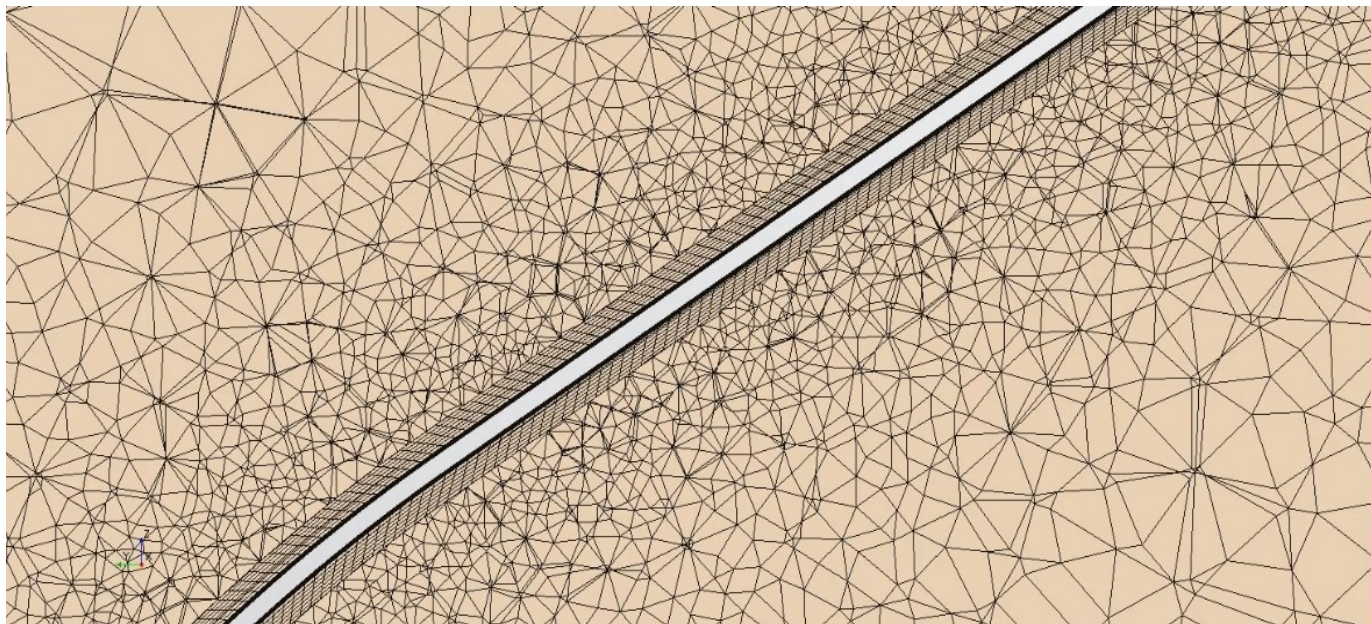


Figure 25: Blades mesh zones interface refinement

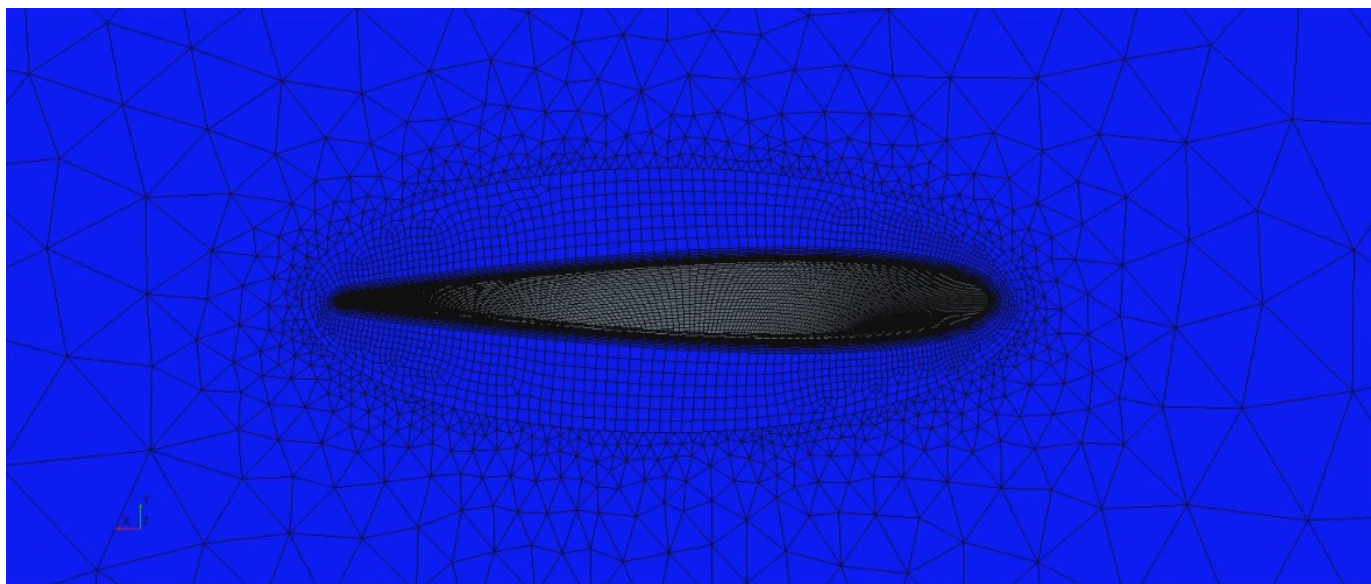


Figure 26: Blades hexahedral mesh at the symmetry plane

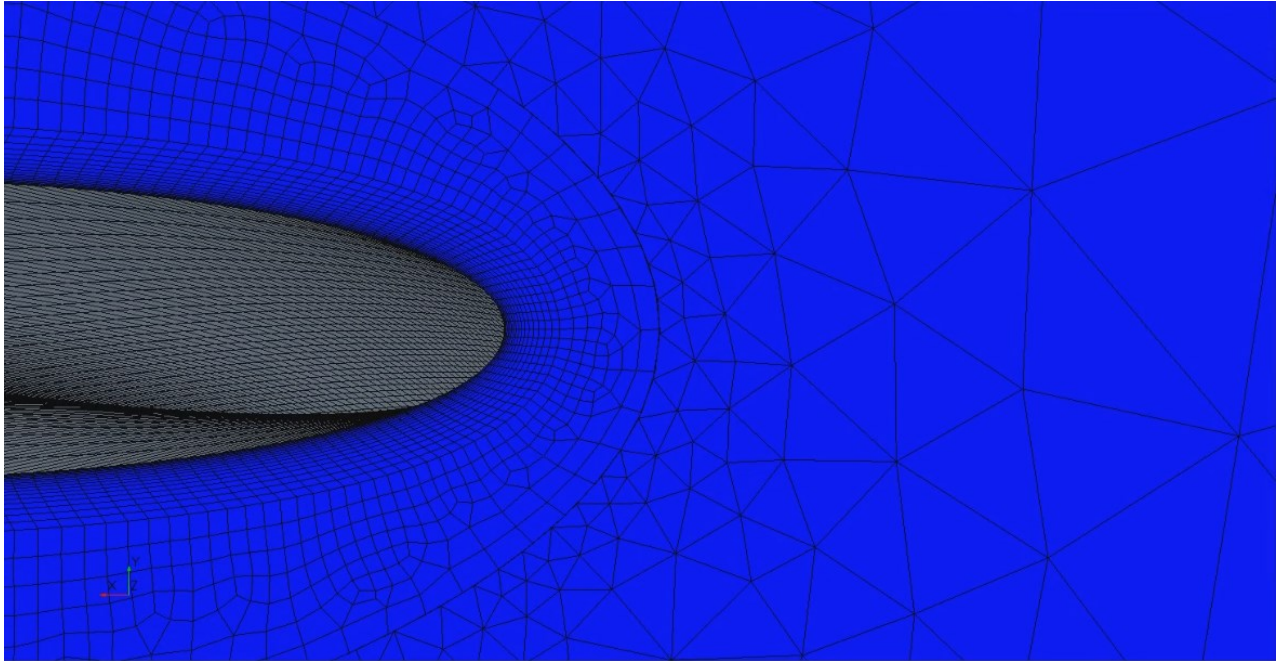


Figure 27: Inflation layers at the blades leading edge

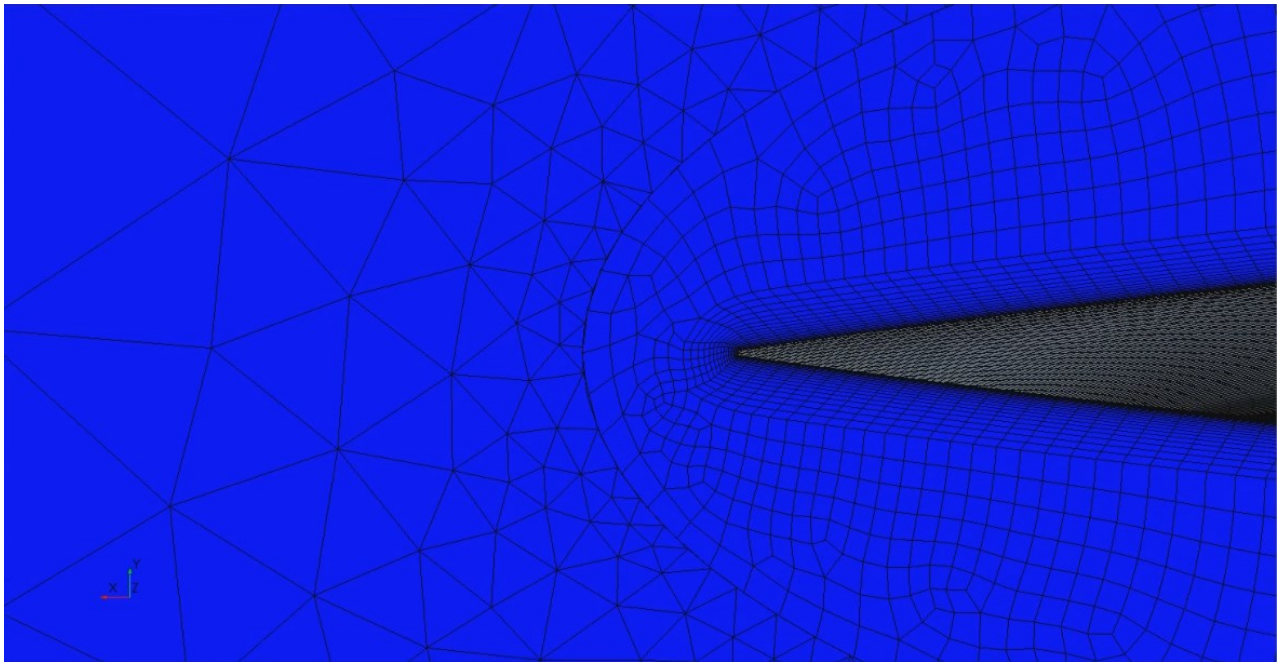


Figure 28: Inflation layers at the blades trailing edge

3.4 Boundary Conditions and Numerical Setup

Selecting the appropriate boundary conditions for each of the computational domain's surfaces is a critical step of the simulation's physical model setup. Figure 29 shows the applied boundary conditions for each validation cases. Detailed descriptions of the selected boundary conditions are given in Chapter 2.5. At the upstream boundary of the static region, a velocity inlet condition is selected. A constant velocity profile is applied at this surface and the magnitude is modified depending on the studied case. The velocity magnitude is obtained from eq. (2.2). On the bottom, top and side surfaces of the computational domain, a symmetry boundary condition is applied. This condition is used to take advantage of the symmetrical nature of the model's geometry at the bottom surface. It is also selected for the side and top surfaces of the domain to model them as slip walls with zero shear stress. Furthermore, a pressure outlet boundary condition is applied at the downstream surface of the static region with a null gauge pressure. For both the inlet and outlet surfaces of the domain, a turbulence intensity ratio of 0.1% is set to simulate wind tunnel test conditions. However, the turbulence viscosity ratio remains at its default value of 10. The blades surfaces are considered as no-slip walls and a non-conformal internal interface is created between the static and rotating region. To connect the rotating domain to the mesh refinement regions around the blades, non-conformal internal interfaces are also generated between them.

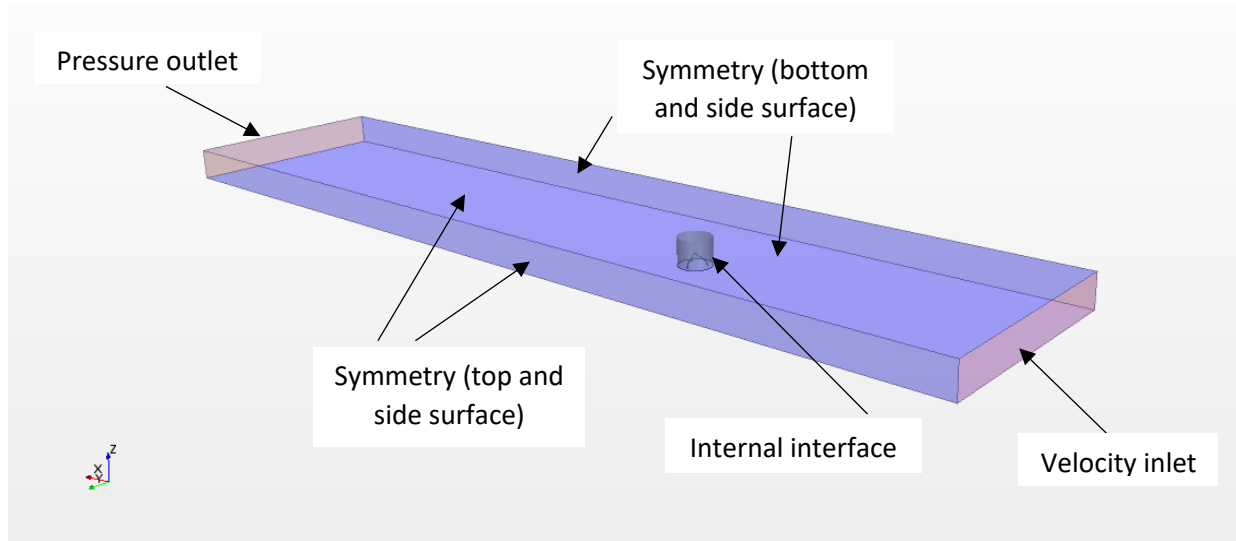


Figure 29: Applied boundary conditions for each validation cases

All three validation cases are given a time-step value corresponding to a rotor rotation of 1 degree about its center axis. The speed of the incoming wind from the inlet varies with each simulated case. It can be computed from eq. (2.2), knowing that the angular velocity of the rotor is fixed at

400 rpm in each scenario. In order to appropriately simulate the rotation motion of the turbine's rotor, a rigid rotating motion of the mesh vertices is applied to the rotating region and the blades refinement zones. This approach allows the mesh cells to remain unchanged as they slide along their respective interfaces. With each time-step, the mesh vertices are rotated and the non-conformal interfaces are updated accordingly. An ideal gas behavior is selected for air. It has a density of 1.225 kg/m^3 and a dynamic viscosity of $1.7894 \times 10^{-5} \text{ kg/m}\cdot\text{s}$. The Menter $k-\omega$ SST turbulence model described in Chapter 2.4.2 is used in conjunction with the Implicit Unsteady model to simulate transient flow over the turbine for a given period of time. The segregated flow solver is selected and the SIMPLE (Semi-Implicit Method for the Pressure Linked Equations) algorithm is applied as a pressure-velocity coupling. This solver computes the different solution variables (such as pressure and velocity) from the non-linear conservation equations of mass and momentum in an iterative manner. The SIMPLE algorithm is discussed in Chapter 2.6. To determine the solution variables gradients, the default Hybrid Gauss-Least Squares method is used. This allows the necessary computation of secondary diffusion terms, variable values at element faces and pressure gradients [45]. Second-order temporal discretization accuracy is applied to each simulation. Second-order upwind is selected as the convective discretization scheme. Values at a given cell faces are computed from the cell's center values using this approach.

The blades moment coefficient (C_m) data is plotted over the course of each run. Once the values of C_m reach persistent oscillatory behavior, which is when the average value of each cycle does not vary by more than 1%, the simulation is considered to be periodic. At this point, the average C_m value of the simulation's last rotational cycle is obtained. It is then possible to determine the final C_p value using eq. (2.3). It is important to mention that each time-step is assumed to be converged once the residuals reach a level below 10^{-5} . The numerical configuration and physical model setup described above are similar to those detailed in Bedon [54] and Samson [8] papers.

3.5 Obtained validation results and discussion

In order to validate the previously described CFD methodology, it is crucial to compare results computed using this approach with experimentally obtained data. Three different CFD cases simulating the wind tunnel testing conditions described in Sheldahl's experimental work [33] were conducted for this purpose. A tip speed ratio, associated with a peak power coefficient value, is selected for each case to determine the wind speed assigned at the inlet. The solution is initialized based on inlet conditions. Figure 30 shows C_p data at different TSR values from various sources. As Bedon [54] performed a similar study using 27 extrusion steps for computation of the boundary layer, the performance curve obtained as part of that work is displayed in Figure 30 for comparison purposes. Furthermore, the performance data curve shown in the validation chapter of Samson's work [8] is also added to Figure 30. The obtained C_p values for each case are given in Table 3.

In his work, Bedon [54] carried out a mesh sensitivity analysis to study the effects of critical mesh parameters on the wind turbine performance data. The growth rate and the amount of boundary layer mesh extrusion steps were considered. The first tested configuration involved 27 extrusion steps with a growth rate of 1.15, while the second combination used 15 extrusion steps with a different growth rate setup. The results showed that although both of the obtained performance curves closely matched the experimental data, the 27 steps configuration performed better for tip speed ratios lower than 4. For this reason, the corresponding performance curve is shown in Figure 30.

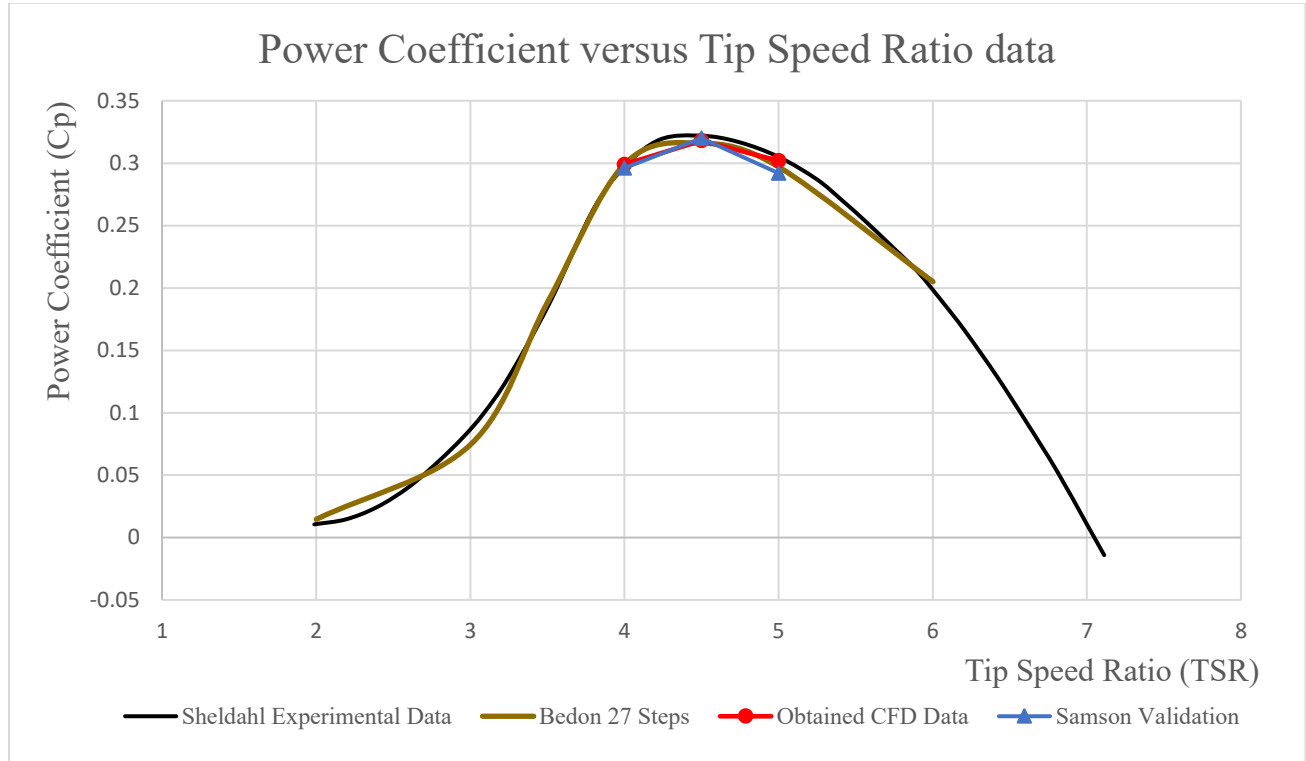


Figure 30: Power Coefficient versus Tip Speed Ratio data

Table 3: Calculated power coefficients from validation cases

Calculated power coefficients from validation cases	
TSR	Cp
4	0.299
4.5	0.318
5	0.302

From Figure 30, one can see that although the simulated cases' geometry and mesh configuration are identical to those described in Samson's thesis, a clear difference in calculated power coefficient values is present, especially when considering the TSR=5 simulation. Also, the obtained CFD data shows better agreement with the experimental results when compared to both Samson's and Bedon's values. The relationship between tip speed ratio and power coefficient is critical in measuring a wind turbine's power generating capability. Therefore, it is safe to conclude that the accuracy of the obtained results show that the previously described methodology is appropriate for conducting simulations that involve this wind turbine's model. Figure 31 displays the C_m curve for the last 3 cycles of the TSR=4.5 case, where persistent oscillatory behavior is clearly shown. Furthermore, the TSR=4 and TSR=4.5 cases converged after 7 cycles, which corresponds to 2520 time-steps. On the other hand, the TSR=5 simulation converged after 8 cycles, or 2880 time-steps.

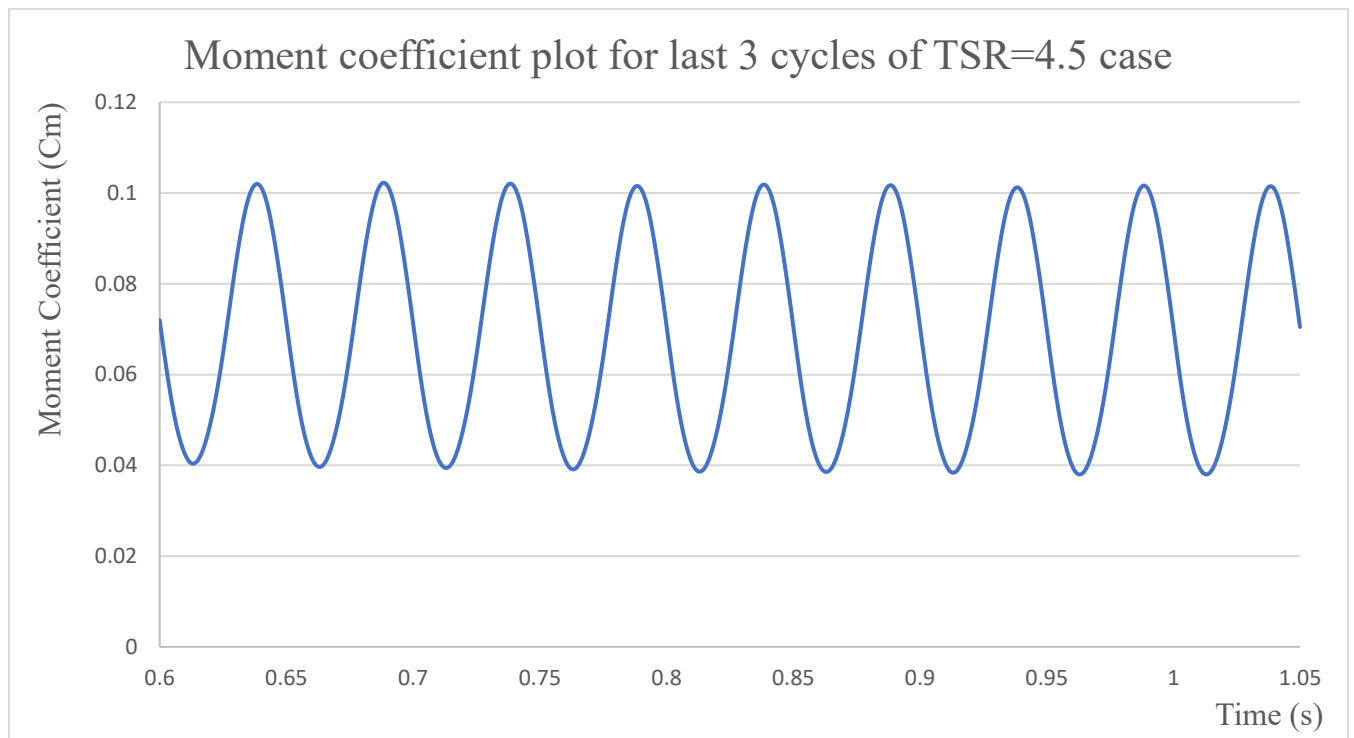


Figure 31: Moment coefficient plot for last 3 cycles of TSR=4.5 case

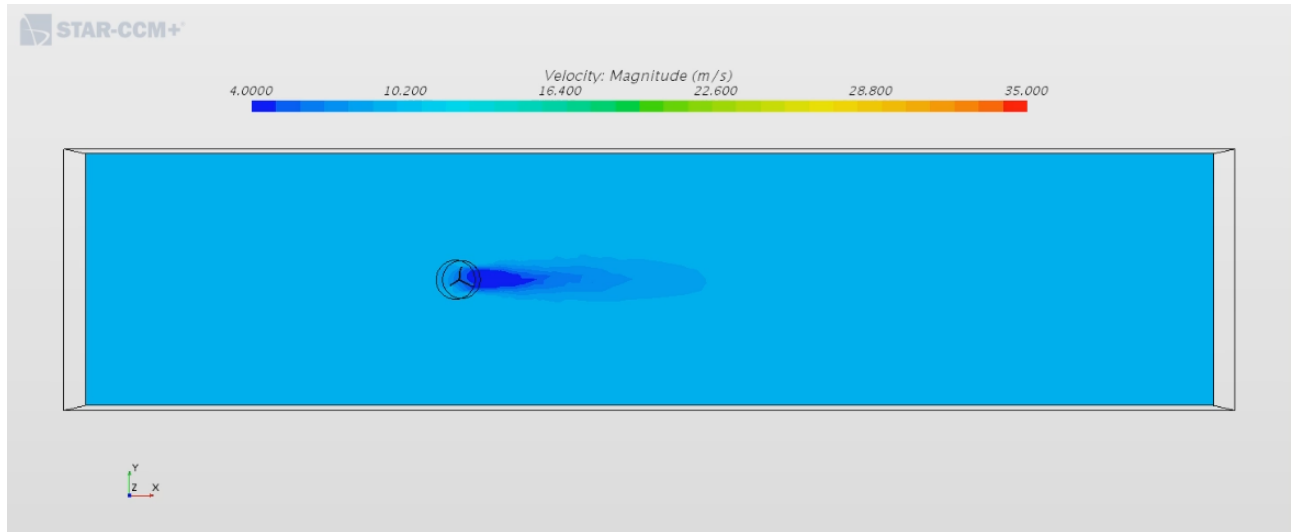


Figure 32: Top view of computational domain's velocity magnitude contour ($\lambda=4.5$)

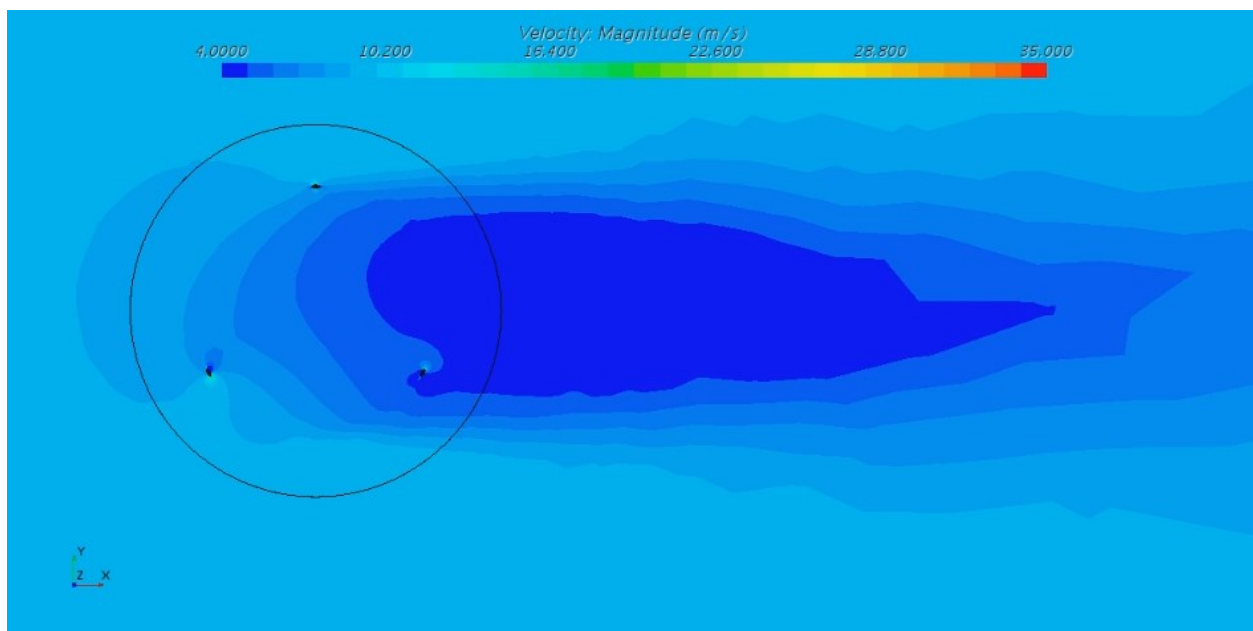


Figure 33: Top view of rotating region's velocity magnitude contour ($\lambda=4.5$)

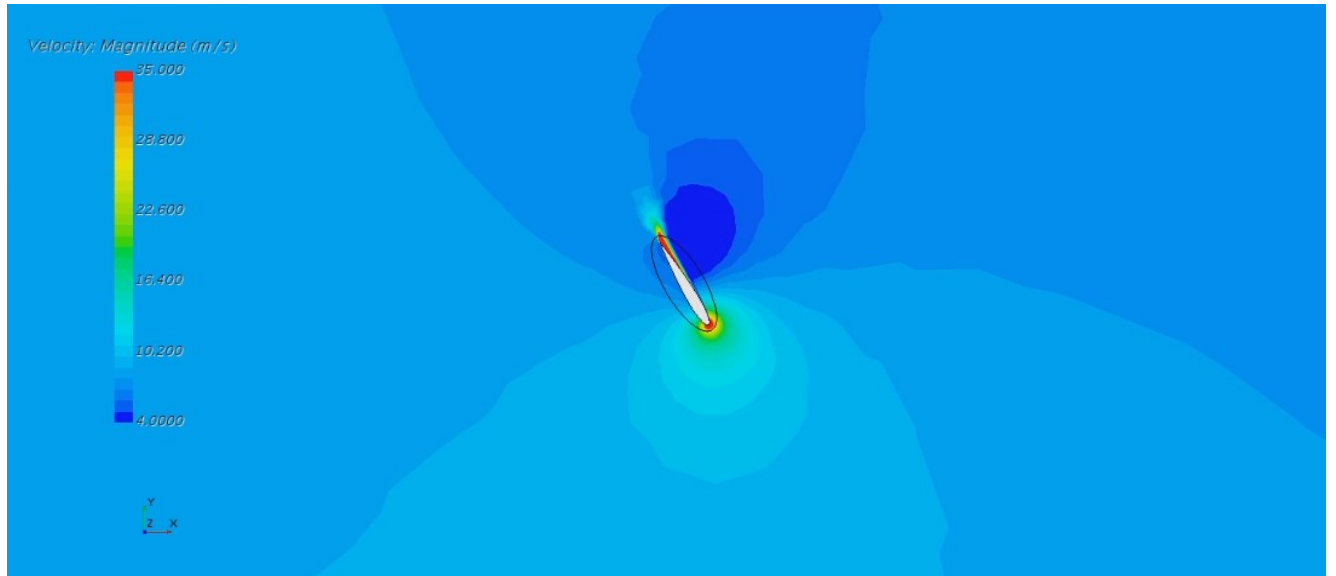


Figure 34: Top view of a rotor blade velocity magnitude contour ($\lambda=4.5$)

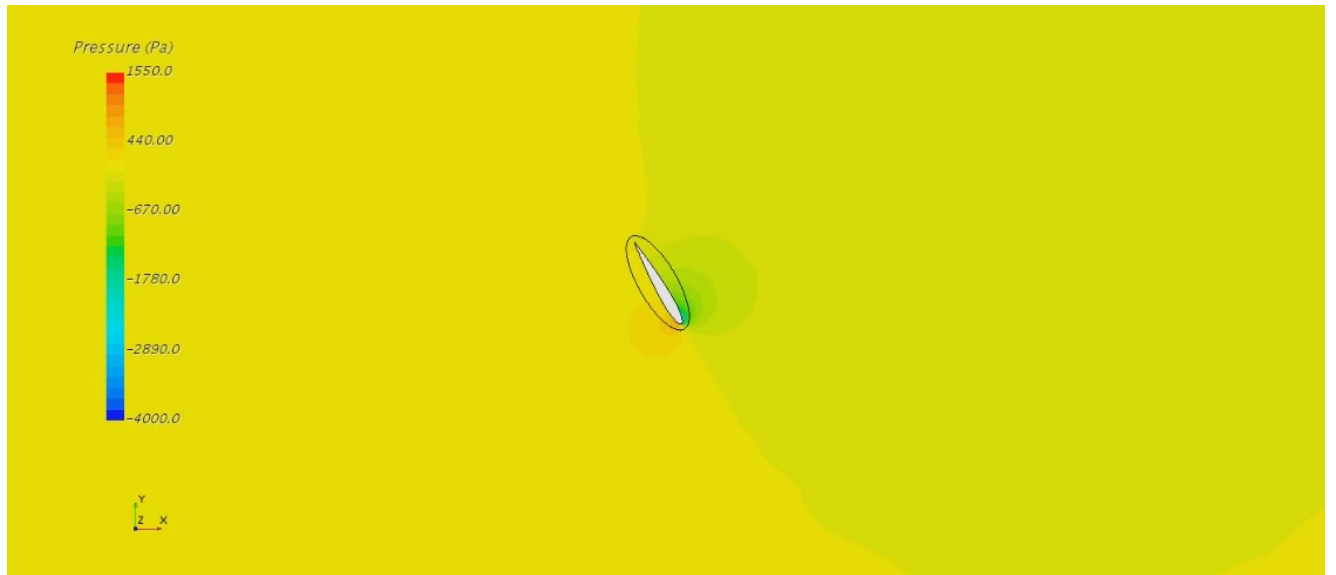


Figure 35: Top view of a rotor blade pressure contour ($\lambda=4.5$)

Figure 32 to 35 show various contours of the computed wind flow for the TSR=4.5 case, after 15 completed cycles. The inflow velocity for this case is 9.122 m/s. All of these contours are located on the bottom symmetry boundary of the domain. Figure 32 shows a top view of the computational domain's contour of velocity magnitude. The wind turbine's wake can clearly be seen where the wind is slower. A close-up view of the wake and the rotor's contour is shown in Figure 33. Lastly, Figure 34 and Figure 35 both show contours of the flow around the upstream blade. High velocity

at the leading and trailing edge, along with high pressure on the windward side of the blade, further confirms the validity of the computed data.

CHAPTER 4: PERFORMANCE ANALYSES OF ROOF-MOUNTED DARRIEUS VAWT

In this chapter, a description of the CFD simulations that involve both the previously shown Darrieus wind turbine model and the cubic building is given. The CFD methodology used to prepare these cases and analyze the obtained results is the same as the one described in Chapter 3. The wind turbine's power generating performance in each scenario is discussed here. It is assessed by first computing its coefficient of power, for a given TSR value, and then comparing the obtained C_p with its corresponding data from the model's experimental performance curve introduced in Chapter 3. Furthermore, comparisons with the performance data detailed in Samson's work [8] of the same wind turbine mounted on the cubic building's roof, is given when appropriate.

Ledo et al. [55] conducted a numerical study of the impacts of suburban topology on the wind flow's speed and turbulence intensity fields above buildings' roofs. In their work, they concluded that the wind direction and the shape of the buildings' roofs are critical factors affecting the turbulence intensity of the flow in that region. It was also determined that micro wind turbines installed on flat roof profiles could potentially reach greater and more constant power production levels, for the same hubs' height, than wind turbines located on buildings with pyramidal or pitched roof shapes. Indeed, the obtained data showed that lower turbulence intensity levels were present in the flow over the flat roofs' cases. Furthermore, higher wind flow speeds could be found at the upstream edges of the buildings with flat roofs, when compared to those with other roof shapes. Thus, a cubic building is used in all of the roof-mounted cases presented in this thesis in order to maximize the performance of the Darrieus VAWT.

4.1 Computational Domain's Geometry

The same Darrieus VAWT model described in Chapter 3, with a straight-circular-straight blade pattern to approximate the Troposkien shape, is considered in each simulation. However, it is not possible to simulate half of the rotor geometry in the roof-mounted cases, as there is no domain symmetry at the rotor's center. Therefore, the full rotor geometry is used for these scenarios. Furthermore, the rotor's central shaft is once again not included in the computational domain's geometry due to reasons mentioned previously in Chapter 3. The NACA 0012 airfoil profile is chosen once more for the blades' configurations. Figure 36 shows the complete Darrieus VAWT geometry used as part of these simulations. The dimensions displayed in Figure 36 are given in Table 1.

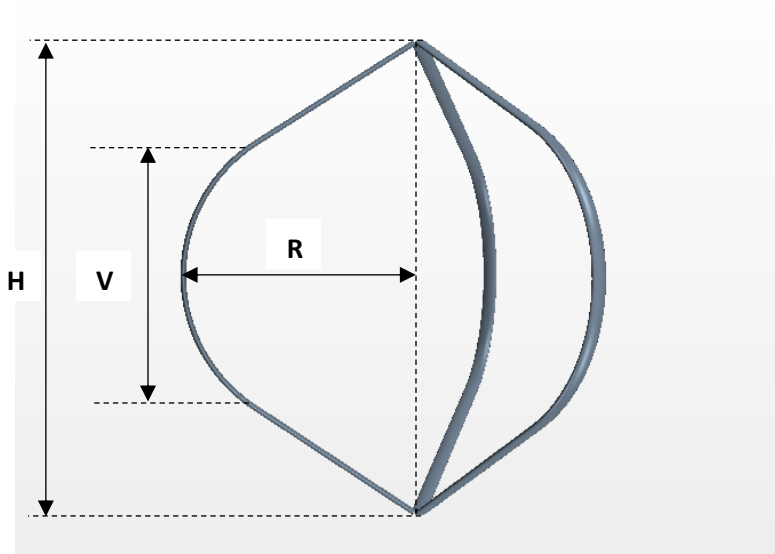


Figure 36:VAWT model full rotor geometry

The computational domain is divided into two parts, the static region, which includes the building geometry and its surrounding area, as well as the rotating region that contains the turbine blades and their respective refinement zones around them. This is done in order to apply different mesh densities and growth rates to the mesh and to allow a section of the domain's mesh to rotate with the blades' refinement zones at a specified angular velocity. An isometric view of the numerical domain is shown in Figure 37. The cubic building is located closer to the frontal velocity inlet side of the domain in order to avoid reverse flow at the downstream pressure outlet surface. The rotating region is shaped as a cylinder and the rotor is located at its center, as shown in Figure 38.

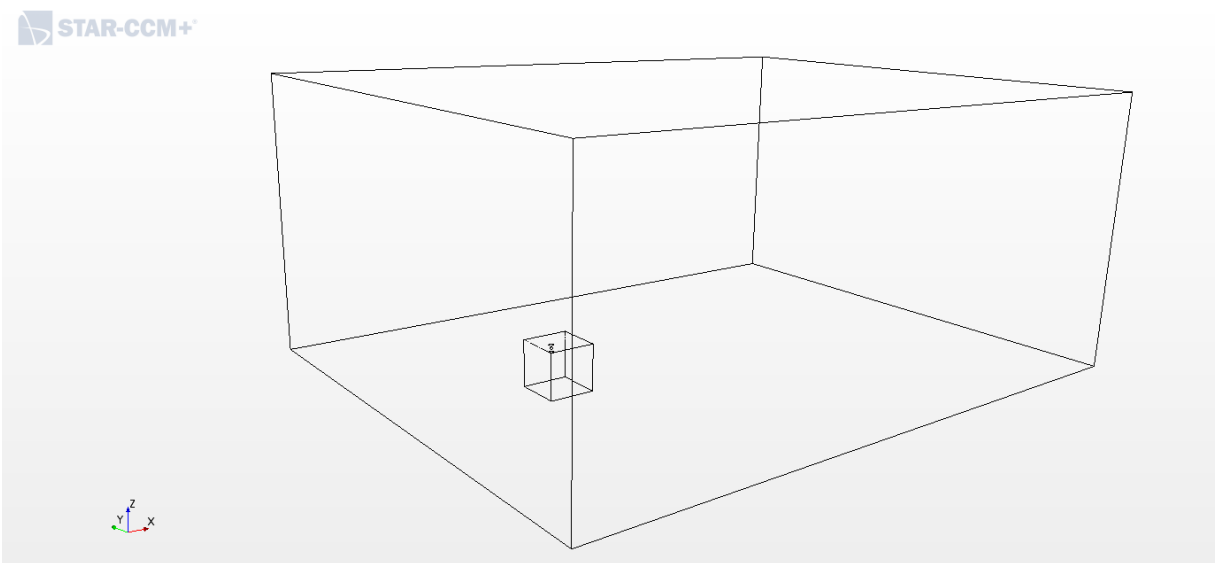


Figure 37: Isometric view of the computational domain

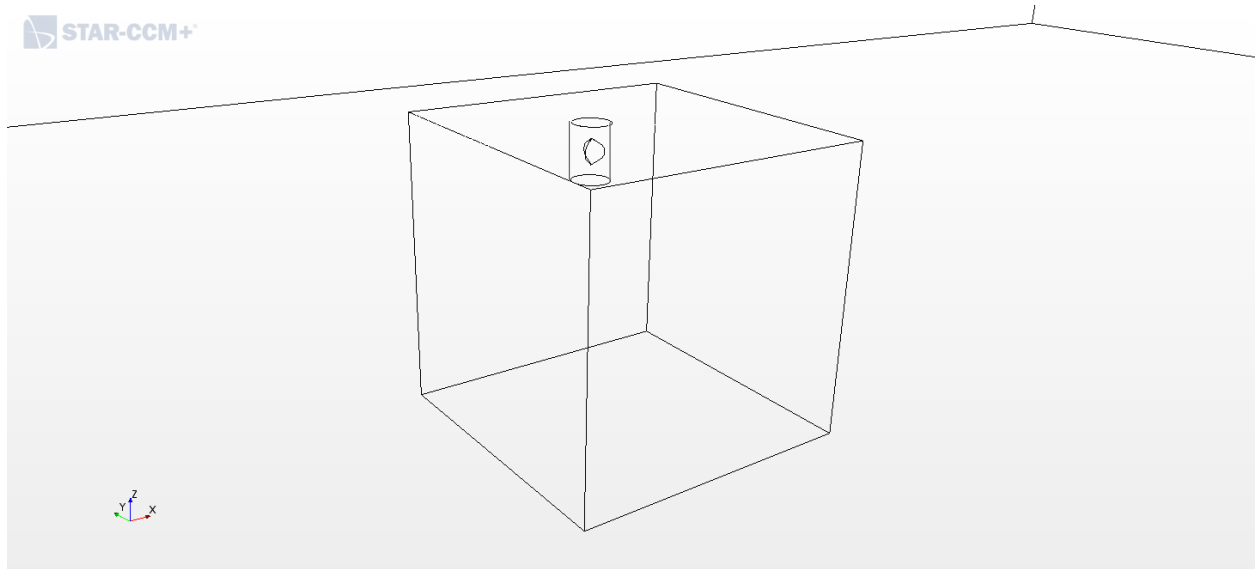


Figure 38: Isometric view of the cubic building and the rotating region located at the building corner

In Figure 38, the rotor is positioned directly above the building corner at a height corresponding to position 1 in Samson's work [8]. This domain geometry is one of the two that are used to conduct the numerical analyses. The other configuration is identical to the one corresponding to position 2 in Samson's paper [8], where the VAWT is located above the center of the upstream edge of the building to take advantage of the accelerated flow in that region. The dimensions involved in both configurations are shown in Figure 39 and Figure 40. The static region's dimensions are based on the domain size recommendations given in [56] and are normalized as a function of the building's height " h ", which is equal to 30.5m. From these figures, one can see that the domain's lateral and top sides are located at a distance of $5h$ from the building's surfaces. Also, the domain's downstream boundary is positioned at a distance of $10h$ from the building and the inlet is located at a distance of $3h$. The height values above the roof associated with position 1 and position 2 are also given in Figure 39 as a function of the rotor's diameter D .

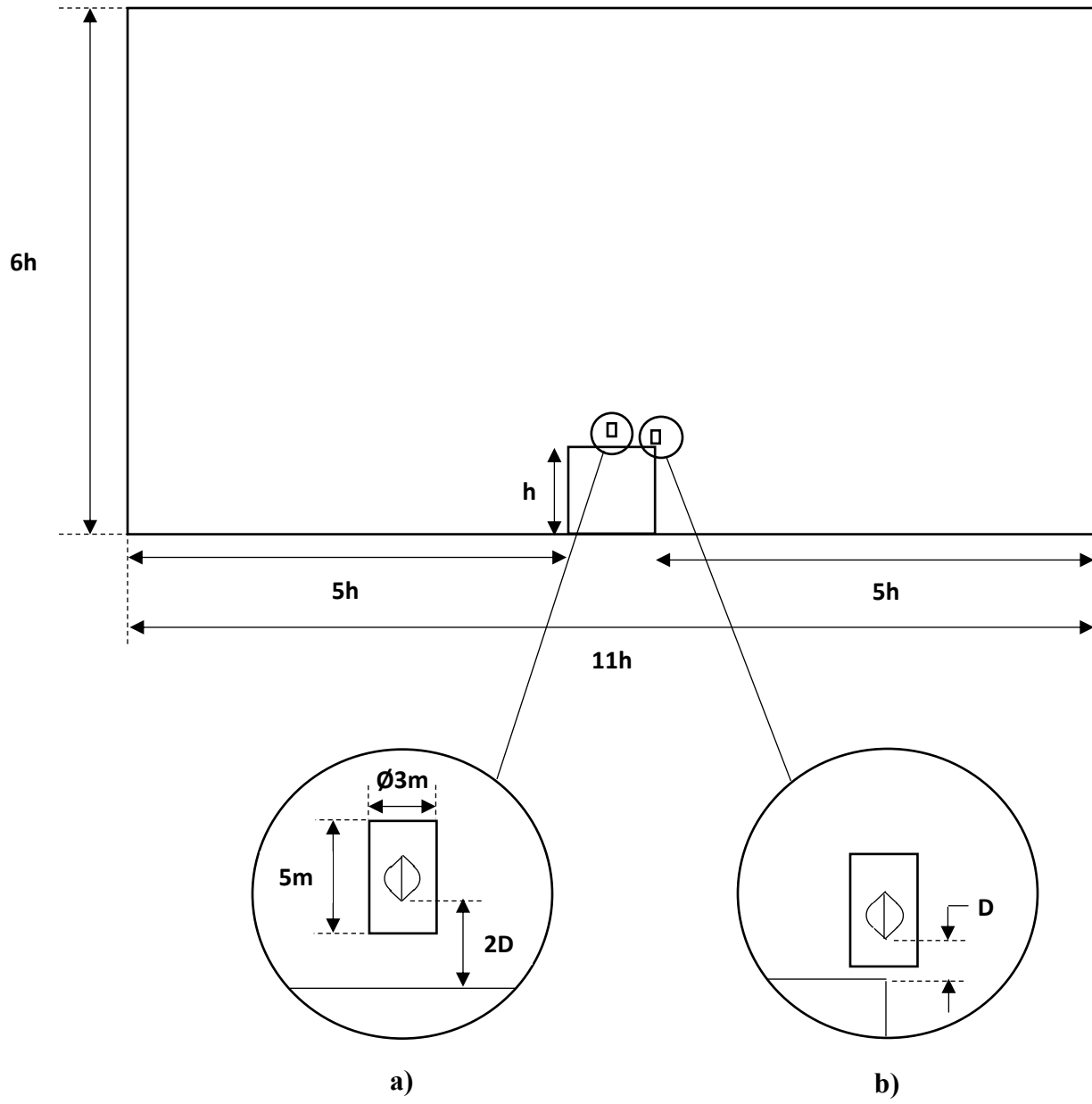


Figure 39: Frontal view of the computational domain with a) VAWT positioned above the building's upstream edge center at position 2, b) VAWT located above the building's corner at position 1 height

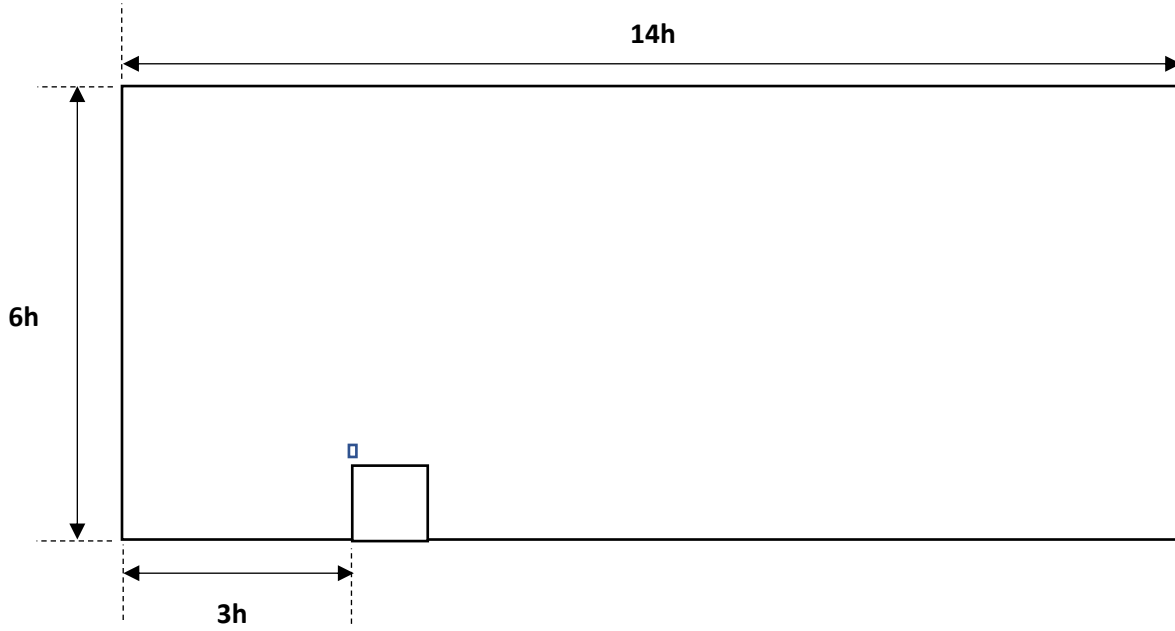


Figure 40: Side view of the center of the domain with VAWT located at position 2

The two VAWT's locations and associated domain geometries are tested at different TSR values and wind directions. The goal is to further study the impacts of this wind turbine's position on its coefficient of power output. The performance investigation of the Darrieus VAWT, when located above the roof's corner and operating under varying wind flow conditions, is of particular interest in this work due to its novel nature. Furthermore, it is also important to mention that both of the wind turbine's positions lie outside of the separation bubble present above the building. It is done to avoid large turbulence effects and low wind velocities associated with the bubble that can affect the rotor's performance.

4.2 Boundary Conditions

Three different sets of boundary conditions are associated with the studied cases, depending on the wind direction. Due to the fact that only some of the roof's corner simulations involved angled wind directions, the position 2 cases only share one set of boundary conditions. All elements of the three sets are shown in Figure 41 and 42. Figure 41 displays the atmospheric boundary layer profile generated using eq. (2.1) at each velocity inlets, with the exception of the top inlet. Indeed, the latter is instead assigned a constant wind speed corresponding to the maximum value of the wind profile for each simulation. It should be noted that eq. (2.1) is always valid, even when the wind direction changes, as it only affects the speed data of the wind profile. Also, it is important to mention that using velocity inlets on the side and top boundaries of the domain ensure that these surfaces further act as slip (zero shear stress) walls.

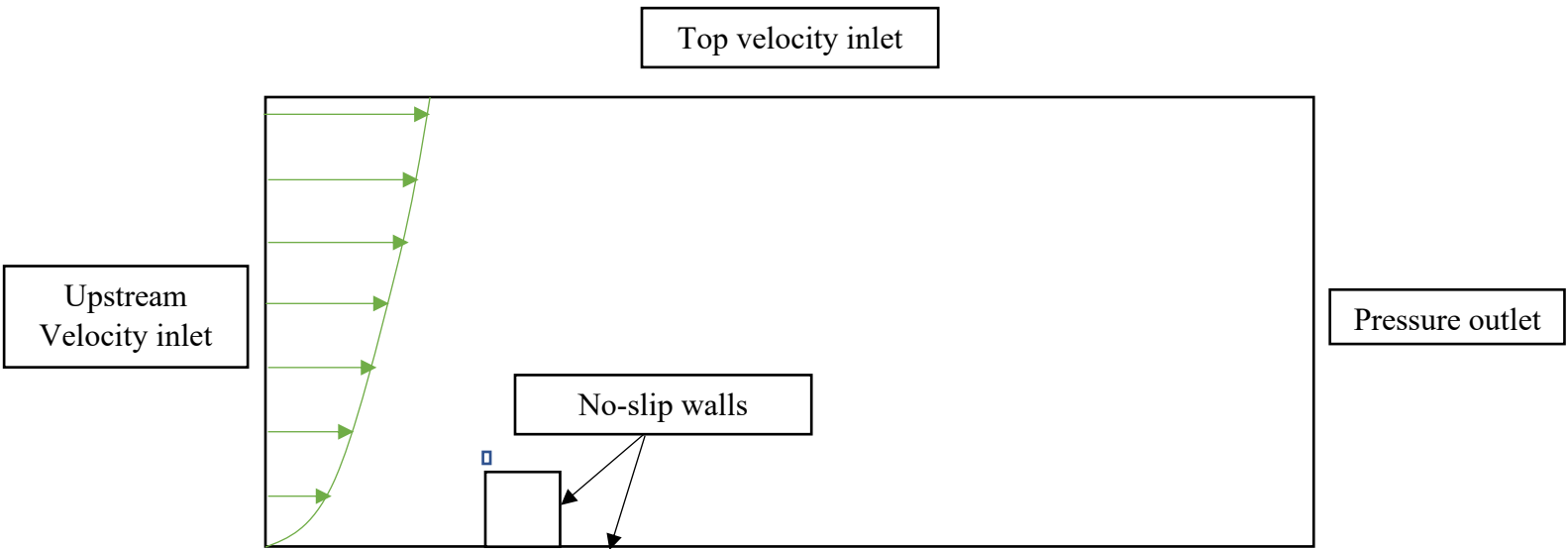


Figure 41: Wind profile for a straight wind (positive X) direction case

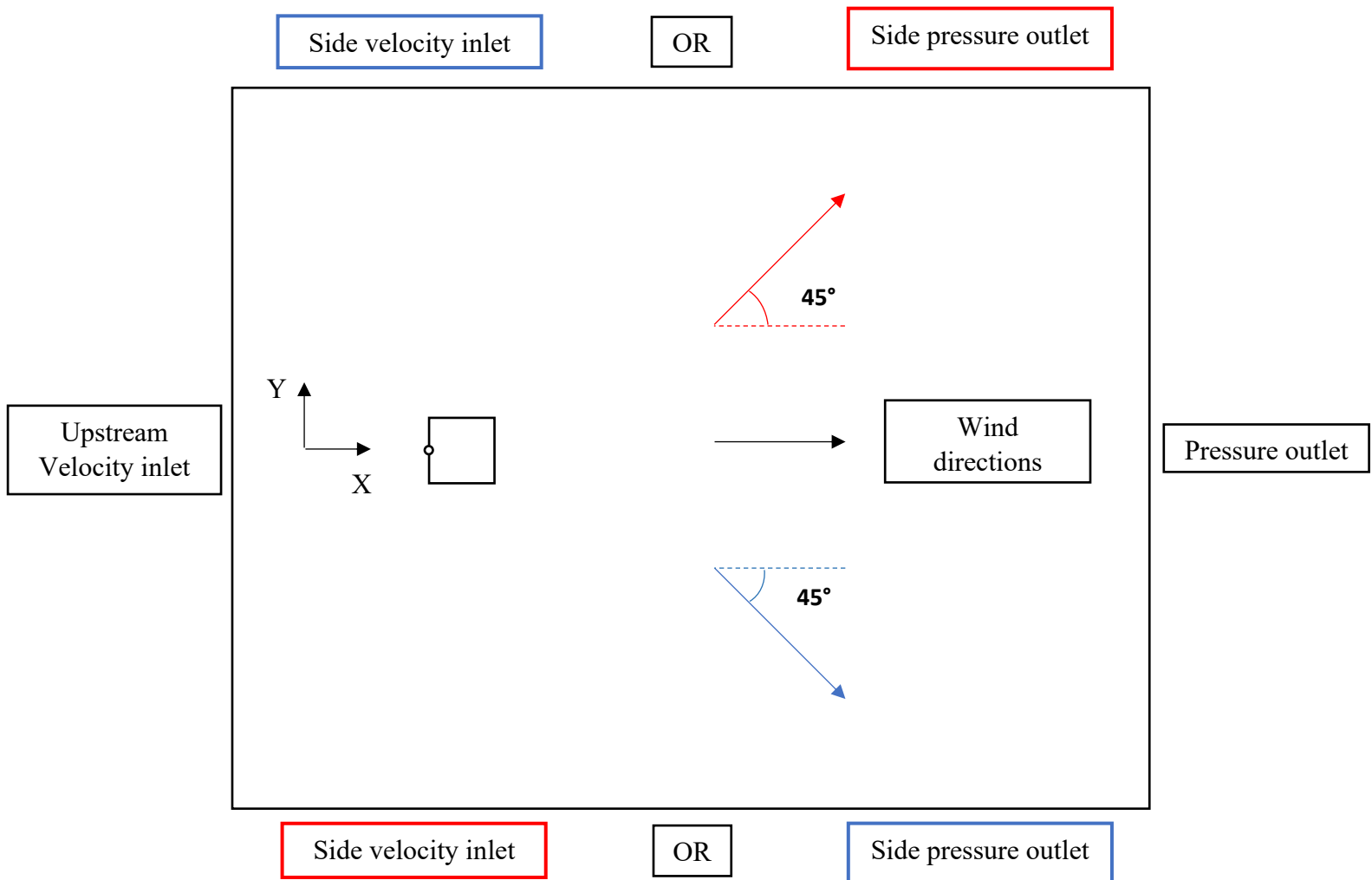


Figure 42: Boundary conditions and selected wind flow directions for the simulations

From the previous figures, one can see that wind direction does not vary in the Z (upward) direction. For a case where the wind follows a straight pattern in the positive X direction, both of the domain side boundaries act as velocity inlets, leaving only the downstream surface to act as a pressure outlet. Furthermore, a turbulence intensity ratio of 1% and a turbulence viscosity ratio of 10% are applied at each velocity inlets, while a gauge pressure of 0 Pa is set for each pressure outlets in order to simulate atmospheric wind conditions. The blades, ground and building surfaces are considered no-slip walls to set the flow velocity at these walls to zero. Non-conformal internal interfaces are generated between the static and rotating regions, as well as between the rotating region and the blades refinement zones.

4.3 Meshes Configurations

As there are two separate domain geometries studied in this work, two different meshes are created accordingly, one for each geometry. For the position 2 simulations, where the Darrieus VAWT is located at the center upstream edge of the building, the applied mesh is identical to the one described in Samson's work [8]. The Import Volume Mesh operation in Star CCM+ [45] is used to bring both the position 2 domain's geometry and the volume mesh, previously created by Samson with the ANSYS workbench mesher, in the Star CCM+ simulations files.

For the cases where the wind turbine is located directly above the building's corner, the mesh associated with the rotating region and the refinement zones around the blades is again the same as the one involved in Samson's work [8]. However, the static region's mesh is different due to the VAWT being displaced at the corner's location. This part of the mesh is generated using the Star CCM+ Automated Mesh operation [45].

4.3.1 Mesh Setup for Position 2 Simulations

Figure 43 displays a frontal view of the computational domain's hybrid mesh. The static and rotating regions are both meshed using an unstructured approach with tetrahedral cells. As progress is made towards the internal interfaces connecting the blades refinement zones to the rotating region, the volume cells are progressively refined to better capture the flow's behavior in the vicinity of the rotor and the building itself. Figure 44 shows a side view of the domain's mesh at its center. From this figure and Figure 45, one can see that cells located around the frontal upstream and top surfaces of the building are more refined than those around the other building surfaces. This is done in order to further increase the accuracy of the flow solution close to the wind turbine's rotor by properly capturing the vortices present inside the separation bubble above the roof. The patch independent meshing operation, which is available with the parts-based meshing approach

in ANSYS workbench mesher, is used to mesh each parts of the computational domain independently. To be clear, the domain's parts mentioned here refer to the previously described regions, such as the static or rotating regions.

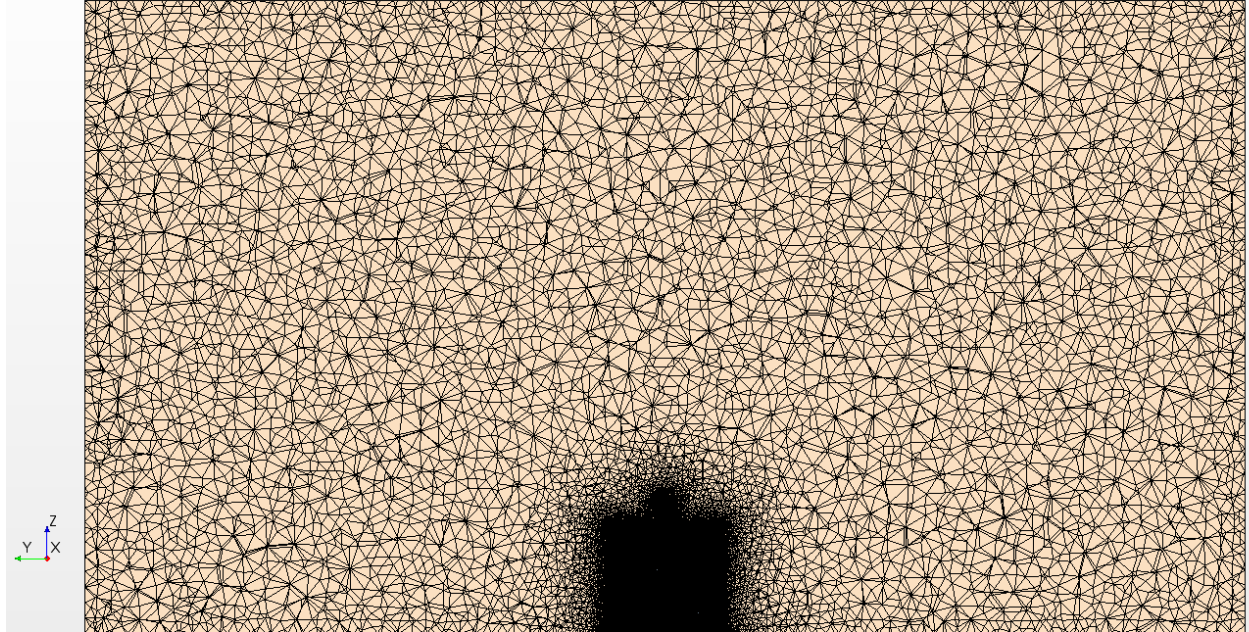


Figure 43: Frontal view of the position 2 cases mesh

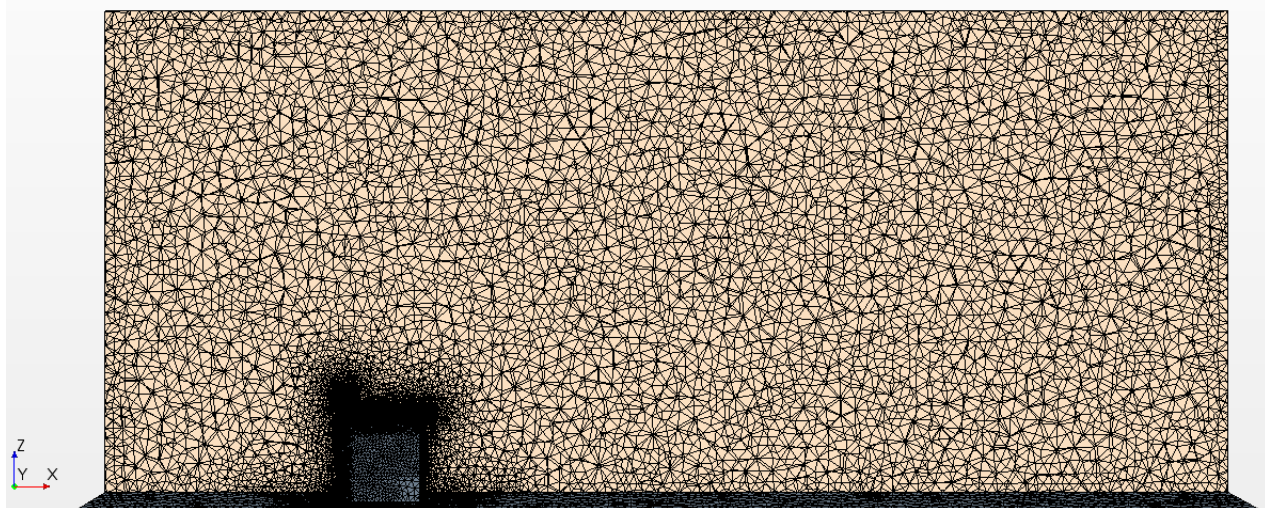


Figure 44: Side section view of the position 2 cases mesh

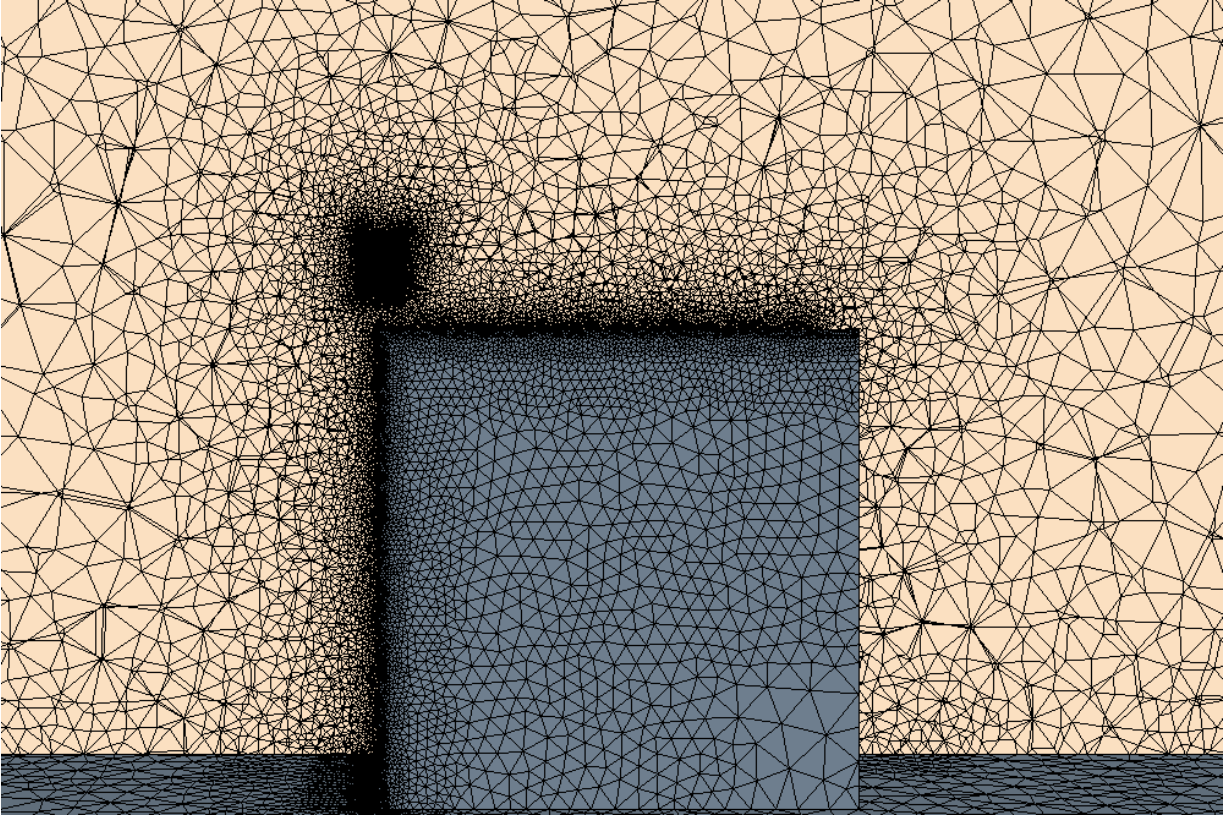


Figure 45: Refined mesh around the building and the static/rotating regions' interface (position 2 cases)

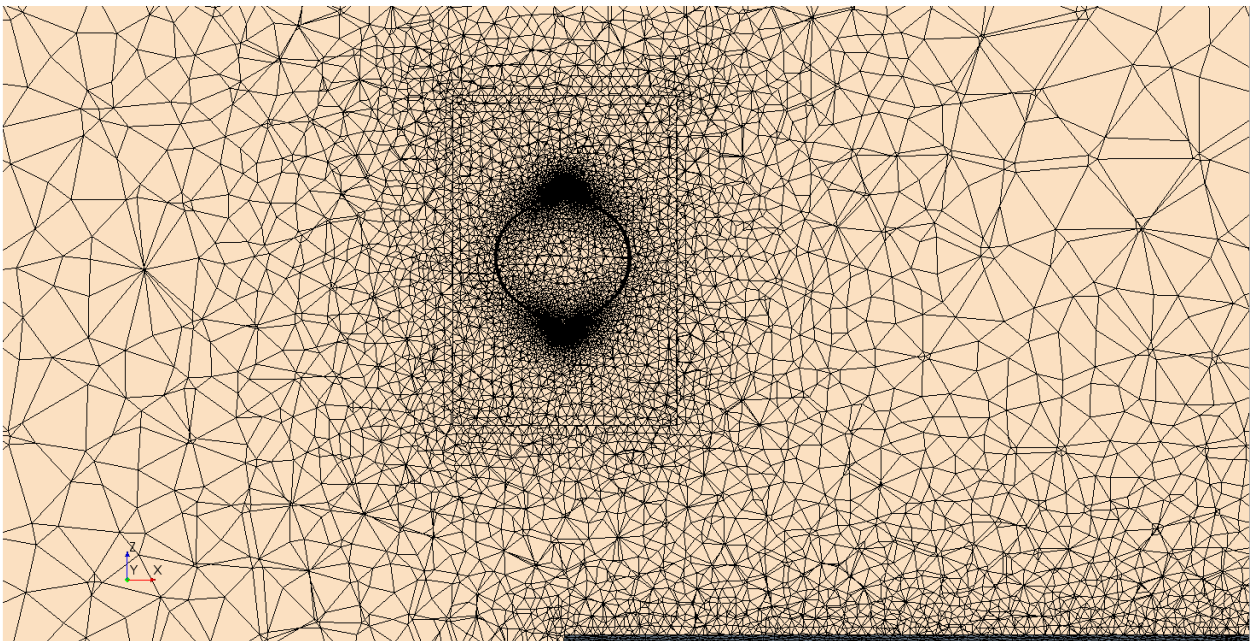


Figure 46: Rotating region's mesh for the position 2 geometry

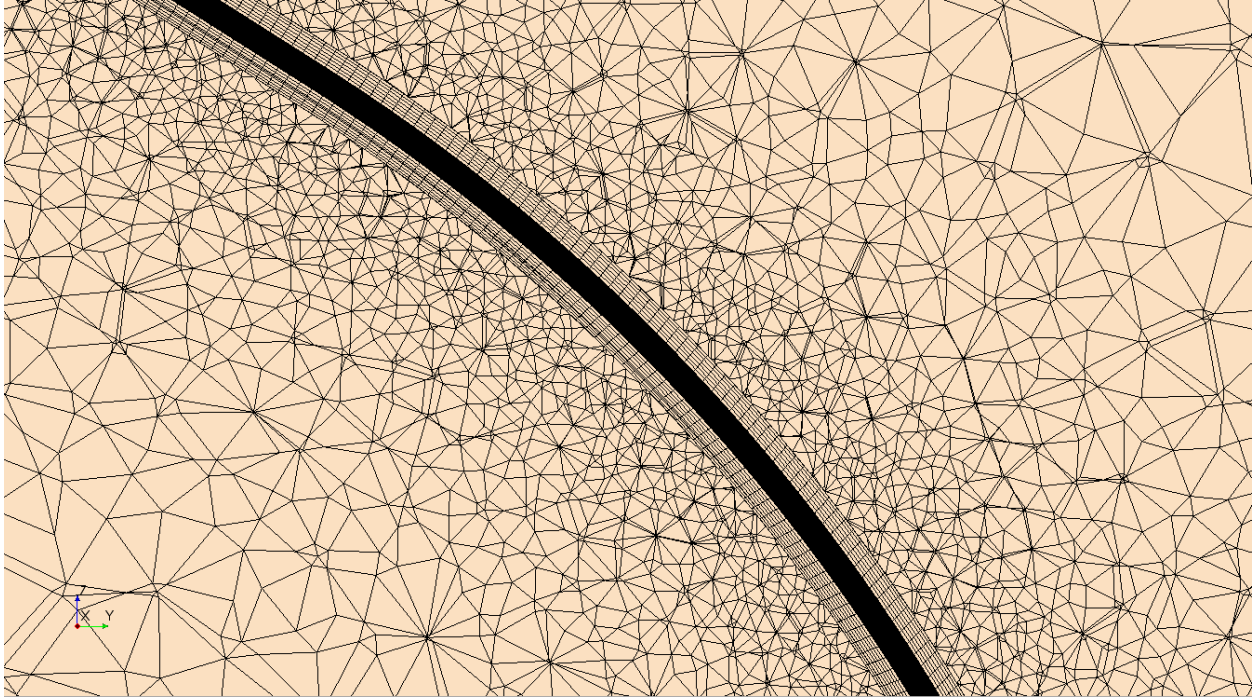


Figure 47: Section view of a blade refinement zone structured mesh

From Figure 43 to Figure 47, a slow size transition of the elements' edges from the coarser to finer parts of the domain can be observed. This transition is controlled by the growth rates of the static and rotating regions, which are 1.15 and 1.01 respectively [8]. Smooth transition between mesh elements helps increase mesh quality and overall control on the total amount of cells.

The same structured mesh approach previously described in Chapter 3 is used to mesh the blades' refinement zones. In order to generate these regions' meshes, the source 2D surface meshes, each located at one end of the blades' refinement zones, are swept across their respective regions' volumes to form 3D hexahedral cells. The source surface meshes are comprised of quadrilateral elements and are similar to the one shown in Figure 26. The inflation layers are also swept around the blades as part of this operation. Figure 47 shows the various volume mesh divisions associated with this meshing technique. The purpose of dividing the refinement zones volume meshes in 640 elements [8] is to ensure that the quality of the original source surface mesh remains constant across the blade refinement zone, which in turns increases the quality of the volume mesh as a whole. The greater accuracy of the structured mesh approach in areas where large gradients are expected makes it an ideal choice for the critical blades' refinement zones parts of the domain's mesh.

A bias factor option of 5 with hard constraining behavior is applied to the leading edges of the blades while a factor of 3.5 is used for the trailing edges upper and lower sections. A bias factor is described as the ratio of the largest element edge size on a curve to its smallest edge size. Using

these options, a total of 132 elements are created on each of the blades' leading edges, while 88 elements populate the trailing edges. Furthermore, 4 elements are defined at the trailing edges tips due to their straight cut geometries. In total, 224 elements are present around the airfoil [8]. A low y^+ condition (~ 1) is used to define the thickness of the first inflation layers around each of the rotor blades. The goal of this low- y^+ approach is to appropriately capture near wall flow phenomenon by accurately resolving the flow inside of the blades' boundary layers.

An important quality metric of the volume mesh is the skewness angle. For the mesh configuration described in this section, the maximum skewness angle is 86° with an average value of 27° [8]. Star CCM+ defines cells with a skewness angle above or equal to 90° as bad cells that can adversely affect solver convergence and numerical accuracy [45]. When intricate geometries and significant mesh sizes are involved, a high maximum skewness angle can be considered acceptable. Table 4 shows a summary of the relevant mesh parameters and their respective values.

Table 4: Mesh parameters for position 2 cases

Mesh parameters for position 2 cases	
Parameter	Value
Rotating region interface element size	0.145 m
Static region interface element size	0.130 m
Cell size at the upstream and top surface of the cubic building	0.230 m
Number of elements swept around each blade	640
Airfoil profile elements count	224
y^+ value at each blade surface	~ 1
Static region volume growth rate	1.15
Rotating region volume growth rate	1.01
Static domain volume cells count	4.5 million
Rotating domain volume cells count	14 million
Blade refinement zone volume cells count	3.3 million
Total mesh elements count	28.4 million

4.3.2 Mesh Setup for Building Corner Simulations

Figure 48 shows a frontal view of the hybrid domain's mesh. An unstructured approach with tetrahedral elements is again used to mesh both the rotating and static regions. The Darrieus VAWT's position on the building's roof is the same as the finer mesh zone located at the rightmost top corner of the building in the figure. The rotating region's and blades refinement zones' volume meshes are the same as the one described in the previous section. For this reason, only the static region's mesh is described here. It is created using Star CCM+ mesh operations.

When comparing Figure 48 with Figure 43, it is clear that the center part of the domain's mesh in the first image is coarser than the one shown in the second figure. Volume cells created in Star CCM+ grow away from the domain's boundaries and towards the core part of the mesh. In the static region's geometry, the core part is located around the volume center, which explains the presence of coarser elements there. As the work presented in this thesis focuses on the wind flow's behavior in proximity to the building and the wind turbine's rotor, the presence of these coarser elements is considered acceptable due to their location. A volume growth rate of 1.1 is applied to this region's mesh, which is smaller than the one used previously by Samson [8]. A side view of the domain at the building's corner Y coordinate is shown in Figure 49. A greater concentration of cells is again observed, from Figure 49 and Figure 50, in the vicinity of the upstream and top surfaces of the cubic building for the same reasons mentioned in section 4.3.1.

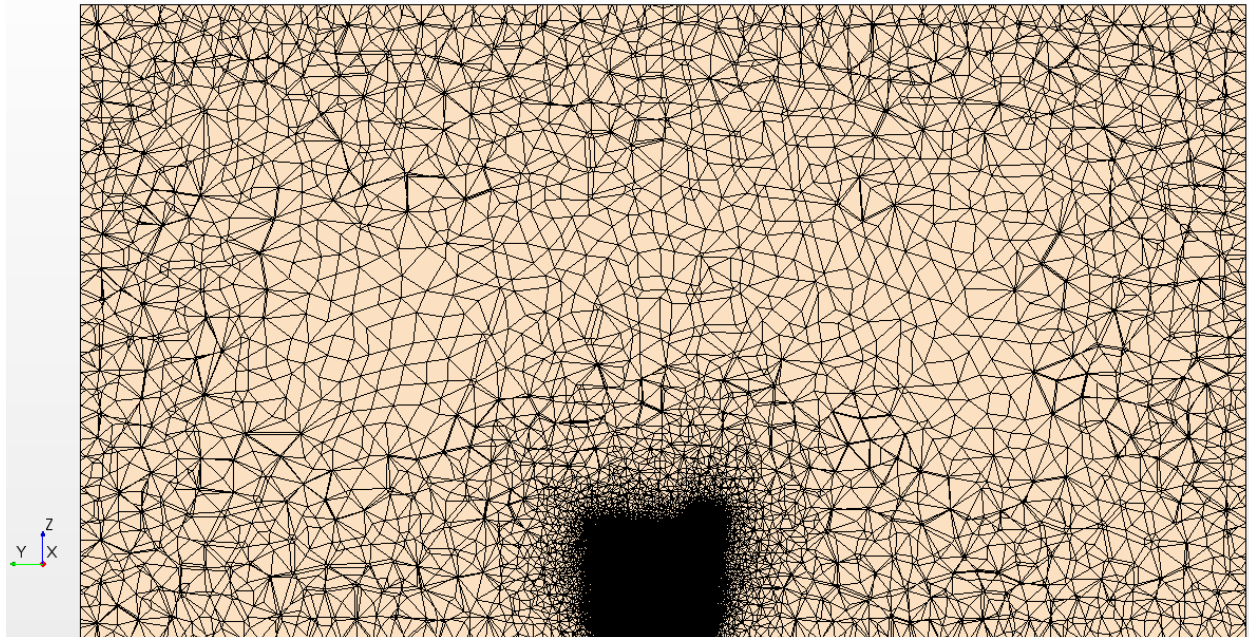


Figure 48: Frontal view of the corner cases' mesh

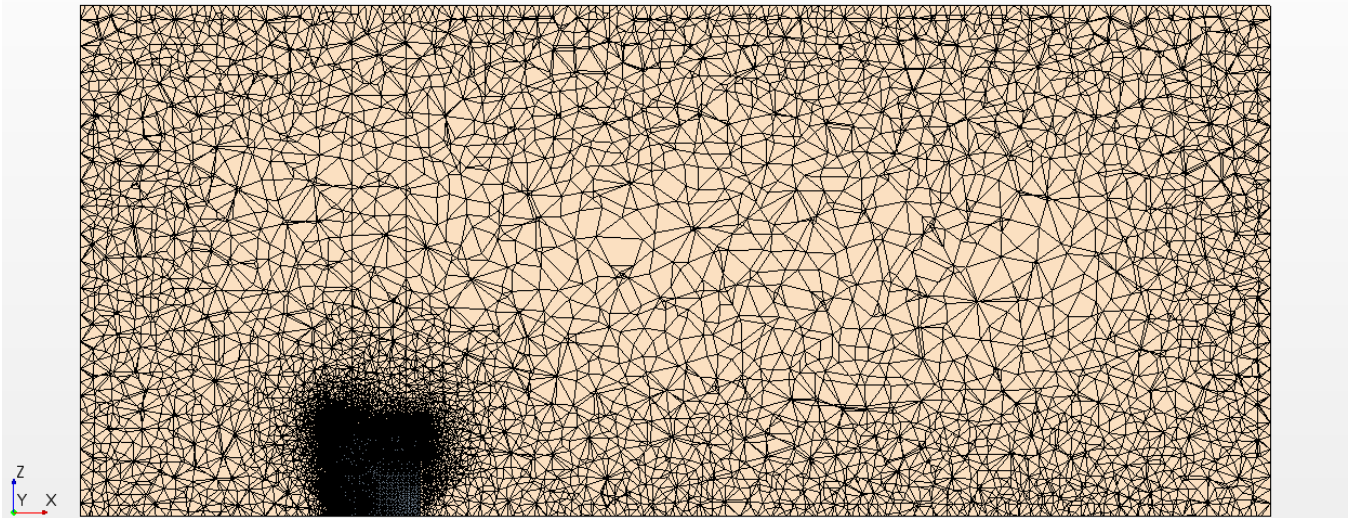


Figure 49: Side section view of the corner cases' mesh

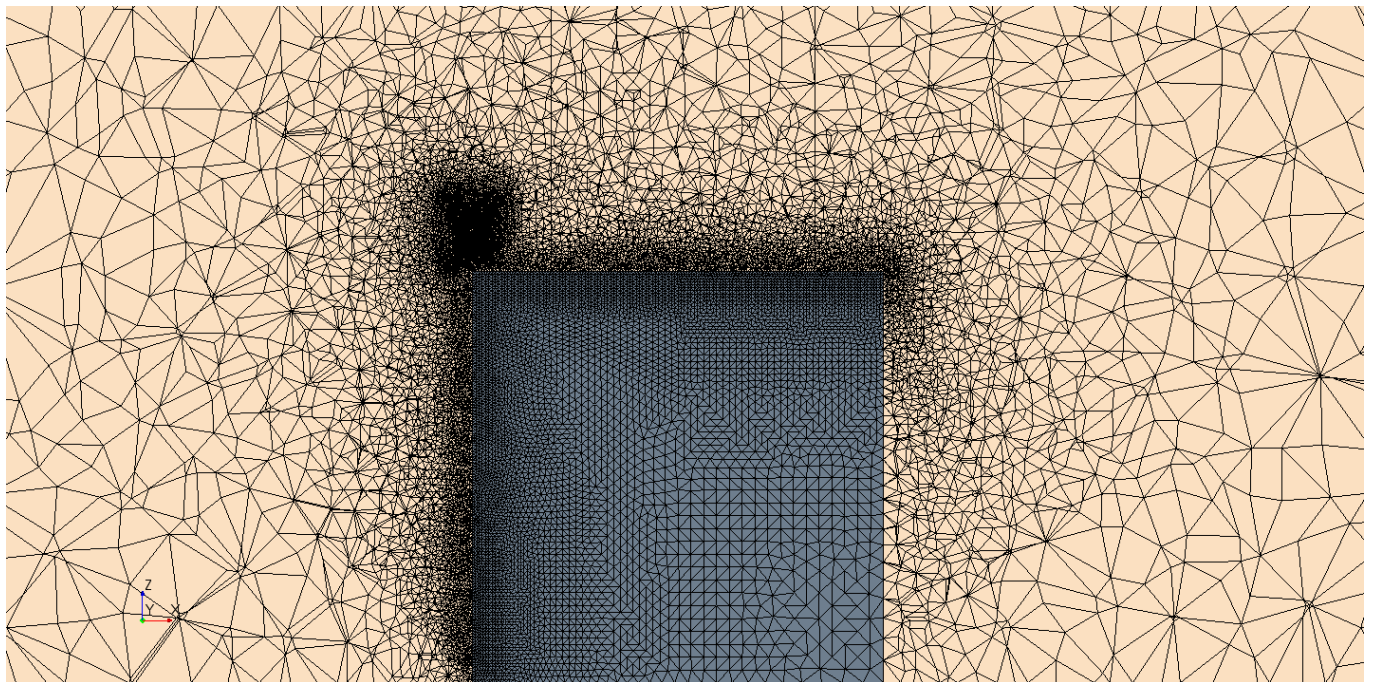


Figure 50: Refined mesh around the building and the rotor (corner cases)

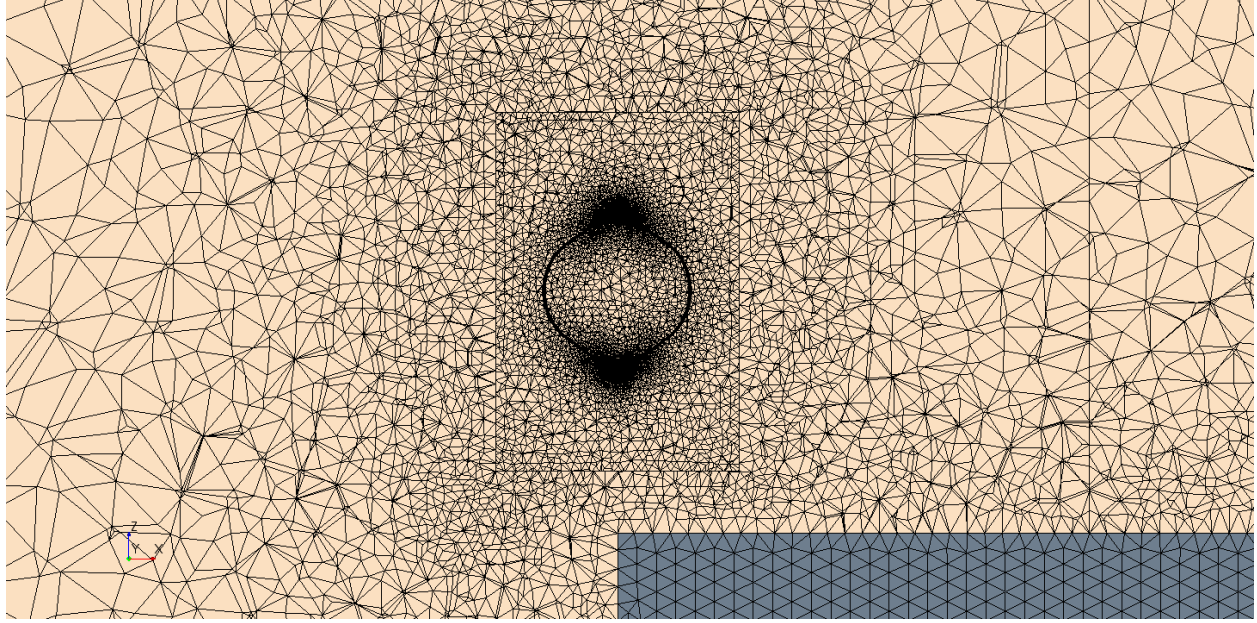


Figure 51: Mesh at the static/rotating regions' interface for the building corner geometry

Figure 51 displays the mesh at the non-conformal internal interface between the static and rotating regions. This non-conformal internal interface links both regions together and allow the flow through their connecting boundaries. An element edge size of 0.145 m is selected for the static region side of the interface. At the velocity inlets, pressure outlets and bottom wall boundaries, a base mesh size of 5m is applied. The proximity and curvature refinement options of the surface remesher tool are selected to improve surface mesh quality. The number of optimization cycles for the tetrahedral volume mesher is set to 8 with a quality threshold of 0.8 to maximize the volume mesh's quality. Furthermore, the surface curvature option for the surface mesh elements is left at its default value of 36 points per circle. This option defines how far an element can spread across a curved surface. The surface proximity refinement is left at its default value of 2 points in a gap and the surface growth rate is set to 1.3. Custom mesh controls are applied to the building's upstream and top walls to ensure a surface element size of 0.2 m. The mesh's maximum skewness angle is 82.5° with an average of 26.5° across the domain. Table 5 displays the important parameters of the computational domain's mesh and their respective values.

Table 5: Mesh parameters for the building's corner cases

Mesh parameters for the building's corner cases	
Parameter	Value
Rotating region interface element size	0.145 m
Static region interface element size	0.145 m
Cell size at the upstream and top surface of the cubic building	0.200 m
Number of elements swept around each blade	640
Airfoil profile elements count	224
y^+ value at each blade surface	~ 1
Static region volume growth rate	1.1
Rotating region volume growth rate	1.01
Static domain volume cells count	3 million
Rotating domain volume cells count	14 million
Blade refinement zone volume cells count	3.3 million
Total mesh elements count	27 million

4.4 Numerical Setup

Both geometries share the same set of physical models as part of their respective physics continuum. This set of models is the same as the one previously described in the methodology validation chapter.

The all y^+ wall treatment, described in Chapter 2.3, is the selected near wall modeling approach. The Implicit Unsteady model, used to define the simulation's time-step size corresponding to 1 degree of rotation of the rotor, is applied with a second-order temporal discretization scheme. In this scheme, every term in the differential equations are integrated over the time step Δt . Air density is again specified as 1.225 kg/m^3 while the dynamic viscosity is set to $1.7894 \cdot 10^{-5} \text{ kg/m} \cdot \text{s}$. The incompressible ideal gas behavior is selected for air and the Menter $k-\omega$ SST turbulence model, described in Chapter 2.4.2, is used to accurately resolve the boundary layer around the rotor blades. Furthermore, the angular velocity of the rotor is fixed at 400 rpm in each simulation. Therefore, by varying the TSR value in eq (2.2), a different value for V_t can be obtained. V_t is the desired flow speed at the center of the rotor. A change in V_t value also modifies the speed data of the wind

profile, as stated by eq. (2.1), creating a new case in the process. The Star CCM+ segregated flow solver, described in Chapter 2.6, is used with the SIMPLE pressure-velocity coupling algorithm. The Hybrid Gauss-Least Squares method is also applied to compute the solution variables gradients [45]. The rigid mesh rotation used to simulate the rotor's motion and described in Chapter 3.4 is also applied for the studied cases here. Second-order upwind is selected as the convective discretization scheme, which is used to calculate the convection fluxes on cells' faces in the transport equations. Under relaxation factors are left at their default values.

In order to decrease computational time, a parallel processing approach is used to conduct the simulations. Star CCM+ starts by dividing the computational domain into multiple sections called sub-domains, a method called domain decomposition. The number of sub-domains created is the same as the amount of processes used to run the simulation, as each sub-domain is allocated to a single process. When the domain decomposition is over, the processes commence their parallel work on their respective sub-domains, sharing information periodically. Load balancing and reductions in data communication between the processes, both gained by using parallel processing, are critical to running complex simulations in a time efficient manner.

To measure the rotor's performance in extracting power from the wind, the blades moment coefficient is measured for each simulation. It is taken as an output in each case and plotted over the simulation's physical time in seconds. The run is accepted as periodic when the average C_m output for a given rotational cycle does not vary by more than 1% of the previous cycle's average C_m value. Using eq. (2.3), the final C_p value can then be obtained and plotted against the experimental curve's corresponding value. Time-steps are considered converged when the simulation's residuals fall below 10^{-5} .

4.5 Performance Results and Discussions

Two scenarios involving the position 2 geometry are analyzed: a TSR=5 case with a straight positive X wind direction, and a TSR=6 case with the same wind direction. The TSR=5 case was previously conducted by Samson using the ANSYS Fluent CFD code [8]. The purpose of carrying out this simulation again in Star CCM+ is to further validate the approach described in this chapter by comparing the obtained C_p data of both works for this case.

Six more simulations are carried out using the building corner geometry. The selected TSR values and wind directions for each case, as well as the obtained C_p data, are listed in Table 6. Velocity magnitude contours are shown in Chapter 5 for all scenarios. As Darrieus VAWTs are known for their difficulties in self-starting under high wind speed conditions (at low TSR values), the selected TSR values for the studied cases are between 3 and 6.

Table 6: Calculated power coefficients for roof-mounted cases

Calculated power coefficients for roof-mounted cases			
Computational domain geometry	TSR	Wind direction	Power coefficients
VAWT located at position 2	5	Straight (positive X)	0.418
	6		0.414
VAWT located above the building's corner (position 1 height)	3	45° in the positive Y direction	0.081
		Straight (positive X)	0.073
		45° in the negative Y direction	0.080
	5	45° in the positive Y direction	0.399
		Straight (positive X)	0.455
		45° in the negative Y direction	0.549

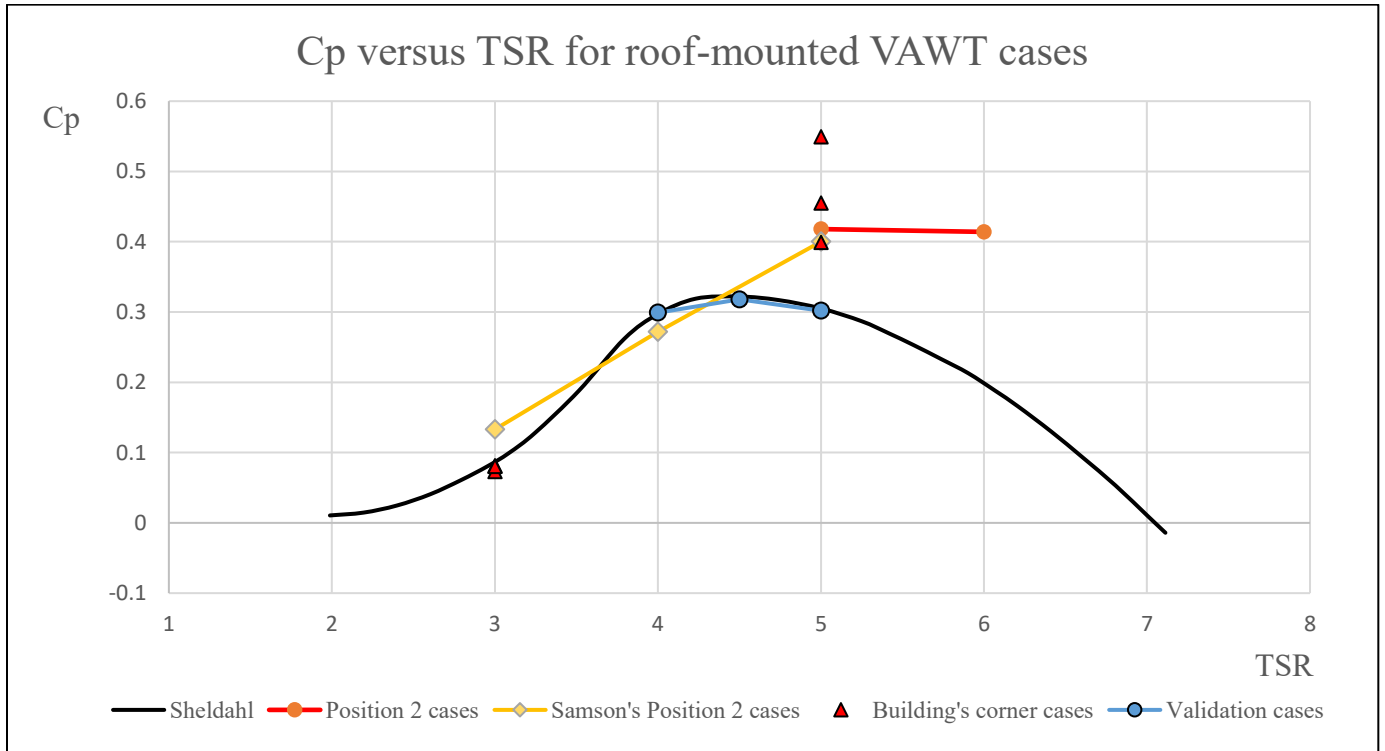


Figure 52: Cp versus TSR for roof-mounted VAWT cases

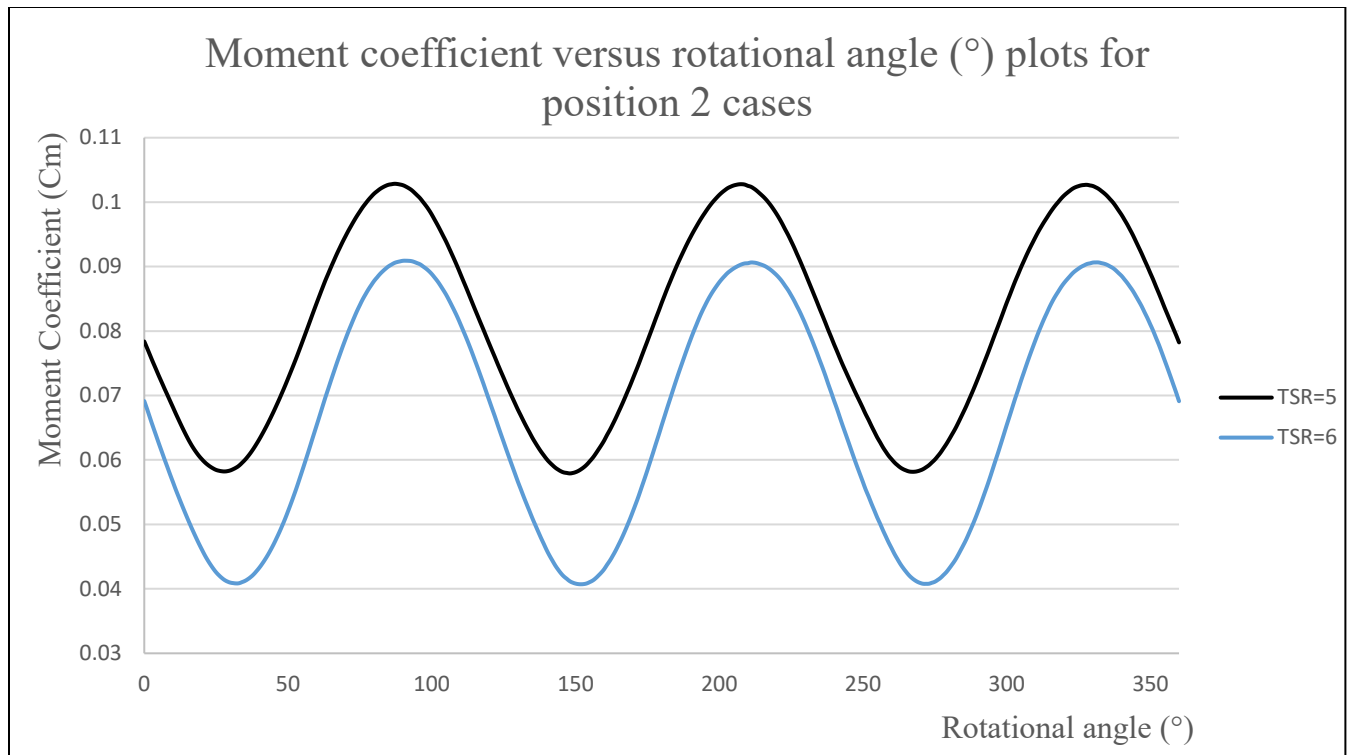


Figure 53: Moment coefficient versus rotational angle (°) plots for position 2 cases

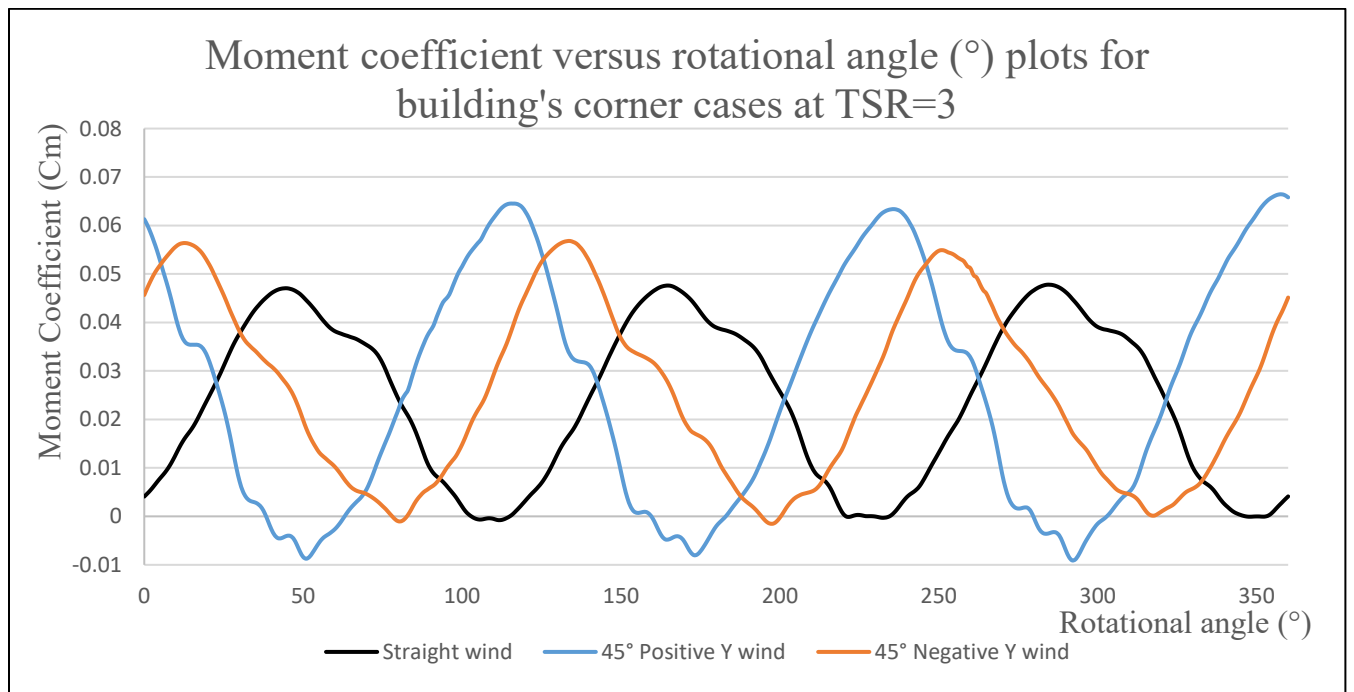


Figure 54: Moment coefficient versus rotational angle (°) plots for building's corner cases at TSR=3

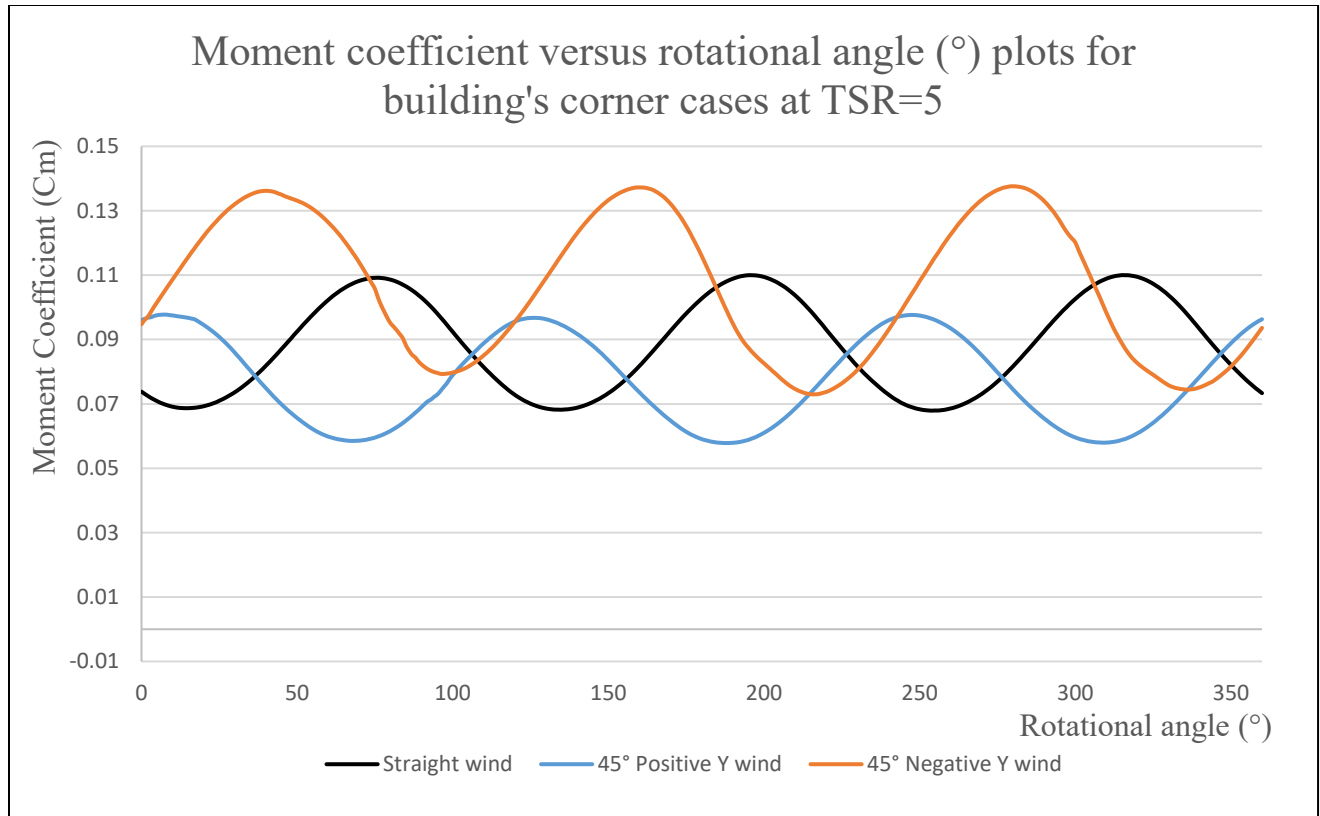


Figure 55: Moment coefficient versus rotational angle (°) plots for building's corner cases at TSR=5

As previously done in Chapter 3, the obtained results are compared with both Sheldahl's experimental curve and the relevant performance data from Samson's previous work [8]. Figure 52 displays the collected C_p vs TSR data from the studied simulations and the aforementioned sources.

For a TSR of 5, a percentage difference of 4.4% is noted between the obtained C_p value from the position 2 case and the one computed by Samson. This error is considered acceptable and shows the validity of the approach. Both of the obtained power coefficients from the position 2 simulations clearly indicate a significant improvement over the validation cases values. These results show that when the Darrieus VAWT is correctly placed above the building, it can perform better (for certain TSR values) than when operating under ideal wind tunnel conditions. The calculated C_p value from the TSR=6 simulation is lower than its TSR=5 counterpart. This suggests, considering the previously obtained position 2 results by Samson as well, that the peak of the VAWT's performance curve for this configuration lies between a TSR of 5 and 6. Also, it is clear that the position 2 performance curve is centered around higher TSR values than the experimental one. An increase of 30% in rotor performance is observed when comparing the C_p obtained from the TSR=6 simulation with the one computed from the TSR=4.5 validation case.

When one considers the computed power coefficients from the TSR=3 simulations, it is clear that the VAWT yields a low performance level at this TSR when located above the building's corner. All three cases involved a different wind direction, which shows that changes in the wind direction only have a minor impact on the rotor's performance at this TSR. Knowing that Samson obtained a C_p of 0.141 from a position 1 case at the same TSR value [8], a loss in rotor performance of 74% is found between this C_p value and the best computed C_p from the building's corner cases at a TSR=3. The VAWT therefore performs poorly at low TSR values when positioned at a height of 1D above the building's corner.

The last cases to consider are those where the Darrieus VAWT is again located above the building's corner, but operates at a TSR=5. Figure 52 and Table 6 show that the simulations where wind is flowing in the straight and negative Y directions both yield the two highest power coefficients out of all the studied cases. For the 45° negative Y wind direction case, an increase of 73% is noted between the C_p obtained from this simulation and the highest computed C_p from the validation cases. Furthermore, the calculated C_p for this case is only 8% lower than the theoretical Betz limit of 0.5926. When one looks at the calculated C_p data for these three cases, an increase in computed power coefficients can be observed from the positive Y wind direction case to its negative Y wind direction counterpart. These results further emphasize the importance of positioning the roof-mounted VAWT appropriately in order to optimize its performance.

In order to further research in the development of new methods to analyze the power generating performance of roof-mounted wind turbines in cities, Maryam et al. [57] created a CFD-based methodology in which the tested Darrieus VAWT's geometry, the same wind turbine model as the one described in this thesis, is not included in the simulation's computational domain. Instead, the different flow speeds, measured at the rotor's centers located above each of the building's corners, are used in conjunction with a new performance curve to determine the turbine's energy output in various scenarios. This new C_p vs TSR curve is actually the experimental curve obtained by Sheldahl [33] shifted upwards by a factor of 1.25, to approximate the positive effects of the building's presence on the wind turbine's performance. The methodology used to obtain this factor is explained in their work. Results from their paper show that this wind turbine model can operate very well above the corners of buildings in low building density areas, especially at the corner where the wind is prevalent most of the time. The three high power coefficients obtained from the building corner simulations (for a TSR=5) further support their methodology by showing the high-performance level attainable by the VAWT when placed at the corner of a building and operating under different wind directions.

Figure 53 to 55 display the change in the rotor blades' moment coefficient during the rotor's last converged cycle for the different simulated cases. The highest and lowest C_m values, as well as the curve's oscillation range, change depending on which plot is considered. The largest oscillation range is associated with the 45° positive Y wind direction case for a TSR=3. Furthermore, negative C_m values are present in the same case's plot. This indicates that each time one of the rotor's blade begins to stall, drag also starts to increase and creates a negative torque on the rotor.

Due to the highly turbulent nature of the flow and its various interactions with the turbine and the building, the amount of time and number of cycles necessary for a given case to converge can vary. Changing the turbine's position and/or the wind direction can affect the flow's behavior around the VAWT and the building, such as the formation process of the vortex and the separation bubble above the roof or the vortex shedding pattern. These changes can in turn impact the C_m solution of a given case by inducing variations in its average value in time. This increases the amount of cycles needed to reach a periodic behavior in the torque produced by the rotor blades. For the position 2 cases, it took 45 to 50 cycles for the simulations to fully converge. The building corner cases took between 40 and 55 cycles to converge. When running the simulations on computers equipped with 96 cores and 100 GB of RAM, it takes approximately 2 and a half months of run time to complete a case that requires a minimum of 50 cycles to converge.

CHAPTER 5: WAKES AND WIND FLOW ANALYSES

This chapter discusses the wind flow's behavior around the roof-mounted Darrieus VAWT, along with how the rotor's performance affects this behavior, in the various scenarios described in the previous chapter. Furthermore, the wake of the wind turbine is measured for each case. The approximate length and width of the wake are recorded and given in terms of the rotor's diameter D . The Star CCM+ ruler tool is used to take these measurements from the obtained streamlines of wind flow's velocity magnitude. The minimum values in each of the velocity magnitude scales in the streamline contours are set equal to 90% of V_t to help display the shape of the wakes and better approximate their size. As V_t is the desired flow velocity at the center of the rotor in each scenario, it can be expected that the flow's speed inside the VAWT's wake tend to be, for the most part, lower than this value when the turbine's performance is acceptable, due to the wind power extraction process. By setting the minimum value on the scales at $0.9V_t$ for each case, sections of the flow with lower speeds than this value appear in the darkest blue color in the streamline contours. These flow sections can then be used to approximate the wakes' dimensions downstream of the turbine. It is assumed, for all of the simulations, that the length of the VAWT's wake in the wind direction corresponds approximately to the maximum distance, measured from the rotor's center, reached by sections of the flow that have a speed lower than $0.9V_t$. Furthermore, it is also assumed that the approximate width of the turbine's wake in the Z direction, taken at half of the measured length of the wake, is equal to the maximum width attained at that location by flow sections bearing a speed lower than $0.9V_t$. This approach is used to approximate the wind turbine wake's length and width in all of the studied cases.

In their work on the analysis of the downstream wake recovery of a vertical axis wind turbine, Ouro et al. [59] determined that the tested rotor's wake could be divided into 3 different sections. The first and closest section to the rotor is the near-wake region, where the flow has low momentum and contains vortices caused by the blades' dynamic stall. This region can extend up to 2 rotor diameters in distance. The second section, located between 2 and 5 rotor diameters downstream of the turbine, is the transitional-wake region. In this region, the flow's momentum increases at a fast rate and turbulence intensity is high. The third and final section of the wake is the far-wake region. It begins at a downstream distance of approximately 5 rotor diameters, where the flow velocity is at 95% of the free stream velocity, and can extend up to 14 rotor diameters as high velocity fluctuations and flow skewness are still present up to this point. As the wake's flow velocity is almost completely recovered around a distance of 5 rotor diameters, the possibility of installing arrays of this type of VAWT on buildings' roofs is clearly present but requires careful optimisation of the rotors' positions to avoid downstream wake interactions or adverse effects from the flow around the building itself that could negatively impact the overall performance of the VAWTs.

5.1 Flow contours from the position 2 simulations

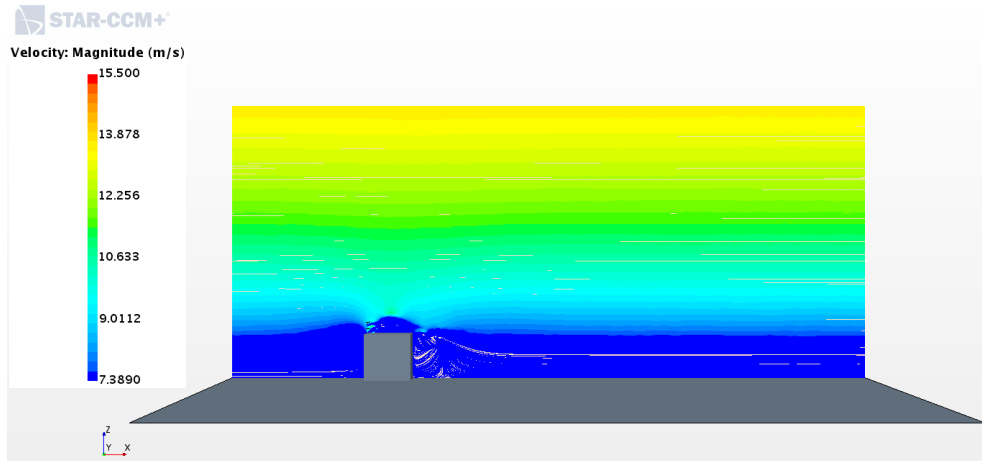


Figure 56: Streamlines of velocity magnitude from the TSR=5 simulation on the rotor's center XZ plane

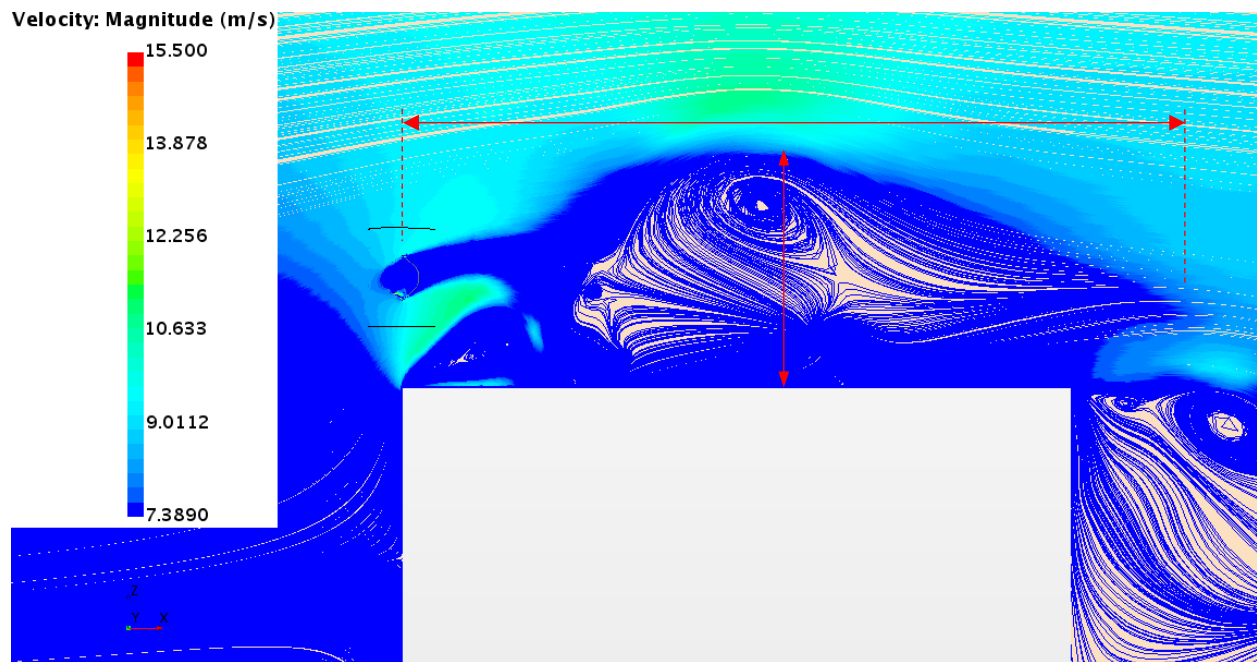


Figure 57: Side view of the flow streamlines above the roof on the rotor's center XZ plane for the TSR=5 case

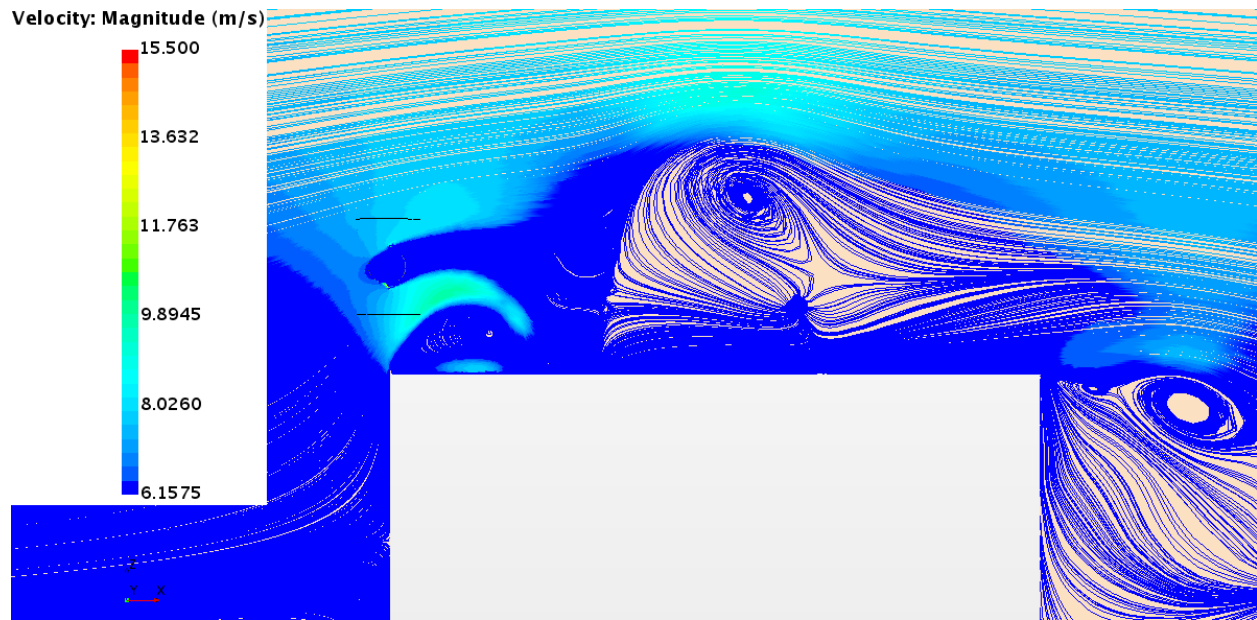


Figure 58: Side view of the flow streamlines above the roof on the rotor's center XZ plane for the TSR=6 case

Table 7: Approximate dimensions of the mixed flow phenomenon for position 2 cases

Approximate dimensions of the mixed flow phenomenon for position 2 cases			
TSR	Wind direction	Length measured in the wind direction	Width in Z measured at half its length
5	Straight (positive X)	18D	5.5D
6		18D	5.5D

Figure 56 to 58 show streamlines of the flow's velocity magnitude for each case and Figure 56 displays an atmospheric boundary layer profile across the domain's center. From Figure 57 and 58, one can see that the VAWT's wake mixes with the vortex formation present above the building's roof in both of the studied cases. Due to this mixing process, the dimensions of the wakes cannot be measured clearly. Therefore, the length and width of the entire mixed flow phenomenon are approximated instead and displayed in Table 7 in terms of the rotor diameter D . It is also clear that changes in the wind velocity profile affect the shapes of both the separation bubble and the downstream vortex formation. In both simulations, the separation bubble extends

only over a small portion of the roof. The Darrieus VAWT's excellent power extracting performances in both scenarios can be attributed to the fact that the rotor is located inside the accelerated flow region above the upstream edge of the building's roof. It is also positioned far enough above the separation bubble to avoid interacting with it. Furthermore, from both Figure 57 and Figure 58, one can see that flow streamlines inside the wakes show speeds below $0.9V_t$. These observations further demonstrate that the wind turbine's rotor is efficient in extracting power from the wind under these flow conditions. However, although a single VAWT's rotor placed at that location can perform well, it would most likely not be possible to add another rotor further downstream at the same height, due to the presence of vortices containing highly turbulent and slower wind flow around the roof's center. Nevertheless, such a case should still be examined in a future work, as there could always be changes in the flow's behavior above the building's roof due to the presence of other VAWT rotors.

5.2 Flow contours from the building's corner simulations

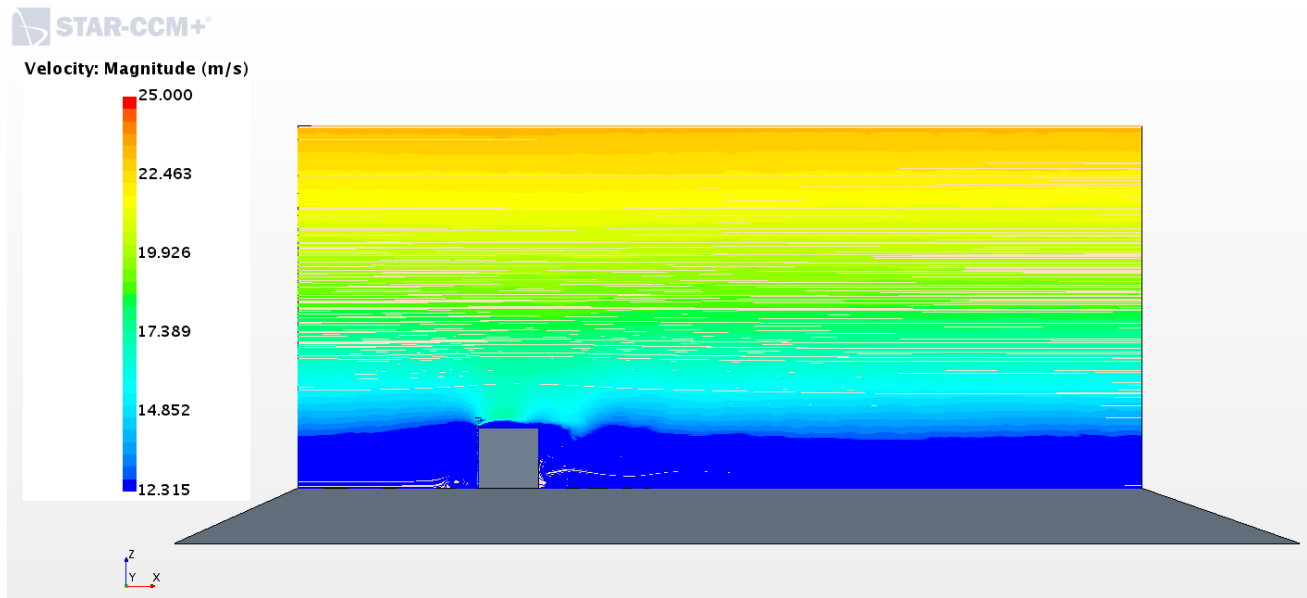


Figure 59: Streamlines of velocity magnitude from the TSR=3, straight wind simulation on the rotor's center XZ plane

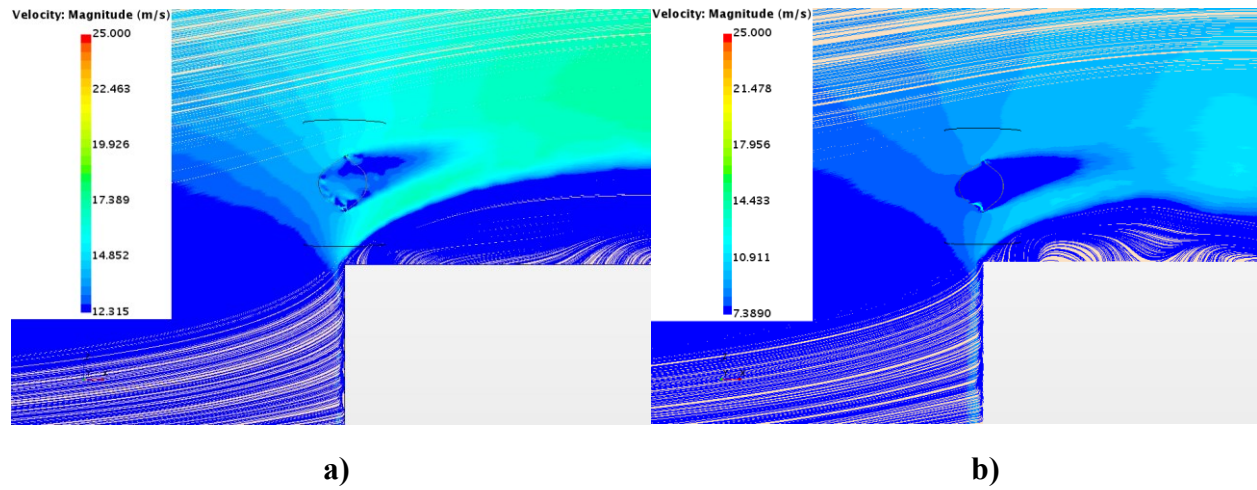


Figure 60: Flow streamlines around the rotor on its center XZ plane from a) the TSR=3 straight wind case and b) the TSR=5 straight wind case

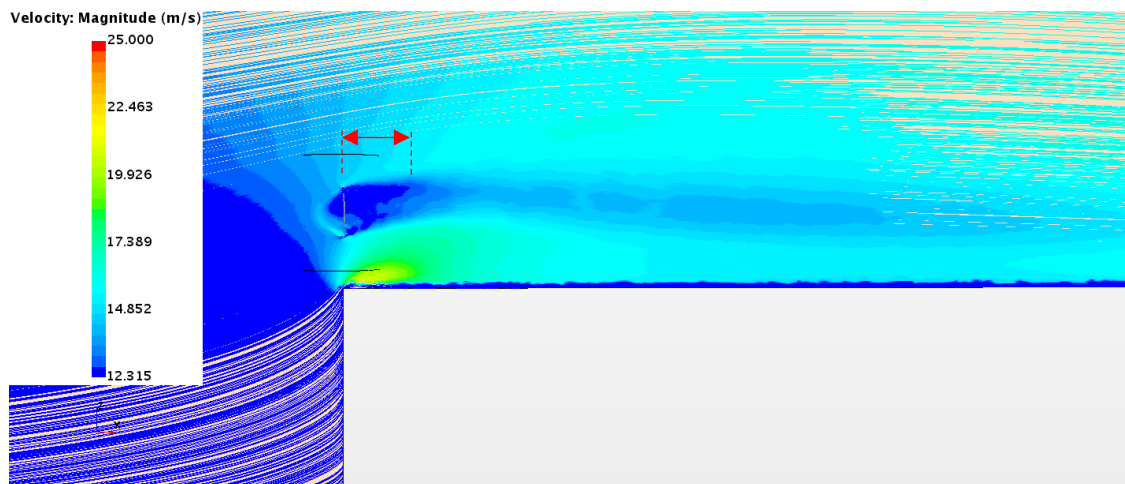


Figure 61: Section view of flow streamlines from the TSR=3 case with a 45°, positive Y wind direction

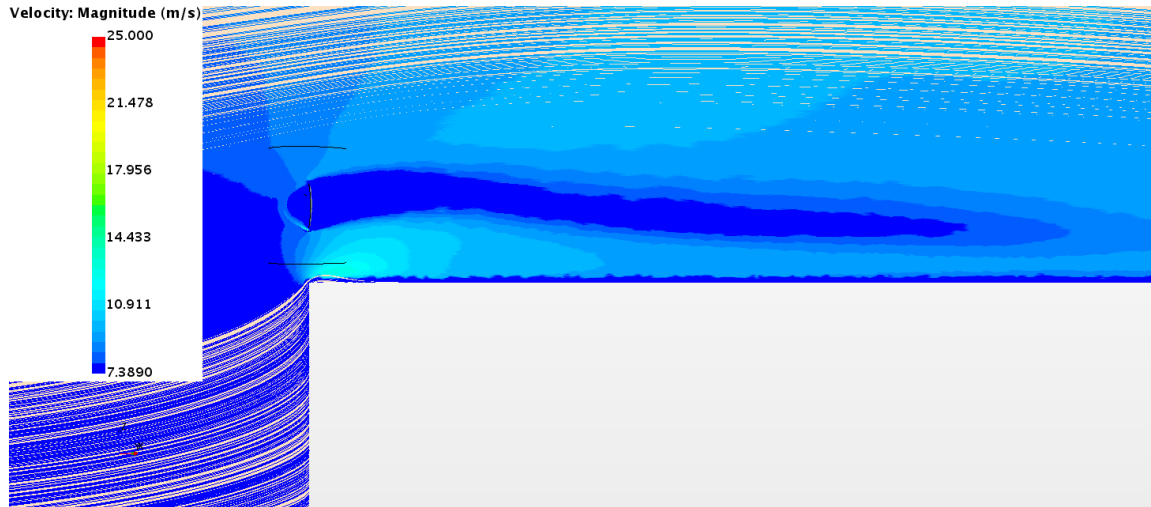


Figure 62: Section view of flow streamlines from the TSR=5 case with a 45°, positive Y wind direction

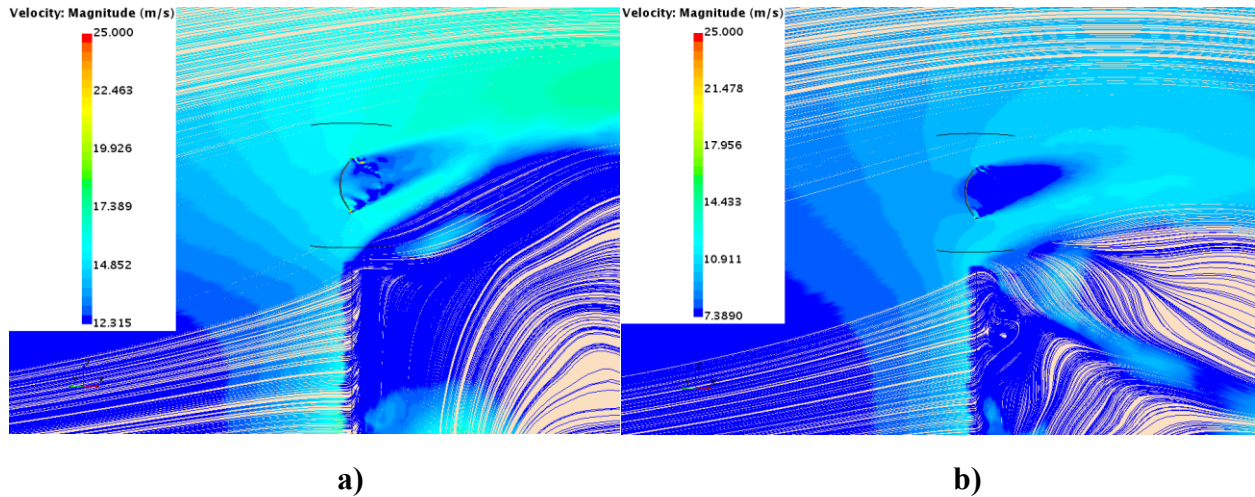


Figure 63: Section views of flow streamlines from a) the TSR=3 case with a 45°, negative Y wind and b) the TSR=5 case with a 45°, negative Y wind

Figure 59 to 63 display streamlines of the flow's velocity magnitude from each simulation. The cross-section planes, on which the flow streamlines are generated, cut the domain in the direction of the wind and through the rotor's center to appropriately capture the VAWT's wake. Figure 59 shows a wind velocity profile across the domain. Considering the rotor's wakes shown in Figure 60 to 63 and comparing those from the TSR=3 cases to their counterparts from the TSR=5 simulations, it is clear that the wakes from the latter cases contain slower winds with speeds lower than $0.9V_t$ across most of their center cross-sections. In the TSR=3 scenarios, the rotor's wakes show more irregular distributions in flow speeds at their center cross-sections, with larger sections of the flows having speeds higher than $0.9V_t$. This suggests that the rotor's performance in extracting power from the wind is reduced under these conditions when compared to the TSR=5

cases. Therefore, these results further support the conclusion that the Darrieus VAWT's rotor performs better at this position when operating under a TSR of 5 than at a TSR of 3.

It is also observed from Figure 60 that both of the wakes do not interact with the separated flows above the building's roof. Instead, these separated flows behave in a similar manner to what would be expected from them in a building only simulation, as shown in Figure 13. Furthermore, when comparing the rotor's wakes shown in Figure 61 and 62, it is found that the one corresponding to the TSR=5 case is much longer than its counterpart. This could be due to both the slower wind velocity profile and the more efficient VAWT's power extraction process from the wind. Another interesting phenomenon can be seen in Figure 63, where the separated flow at the building's corner, for the TSR=3 case, reaches a much higher point than what can be observed in the TSR=5 simulation.

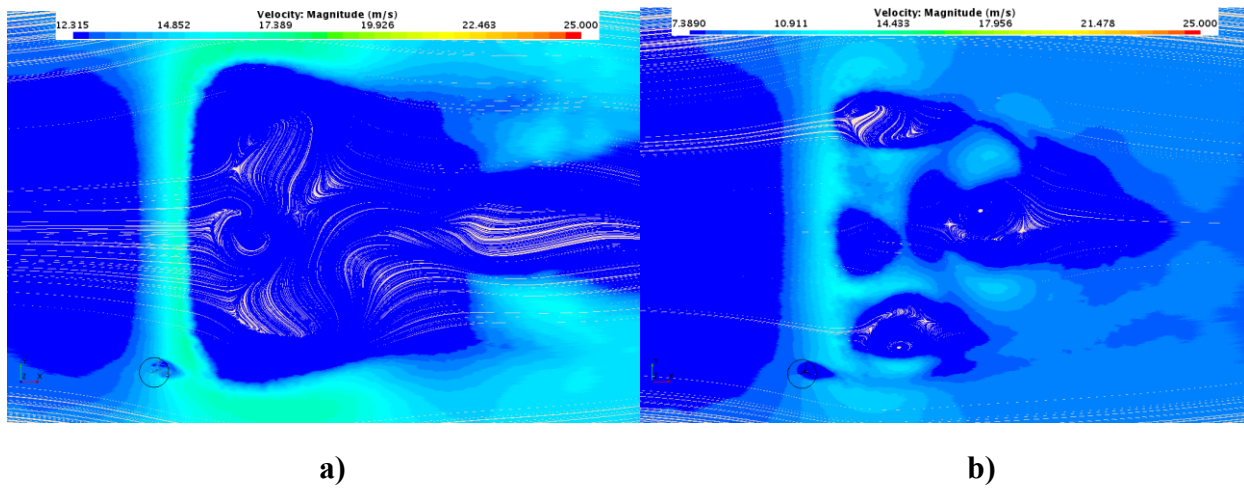


Figure 64: Top views of flow streamlines at the rotor's center XY plane from a) the straight wind TSR=3 case and b) the straight wind TSR=5 case

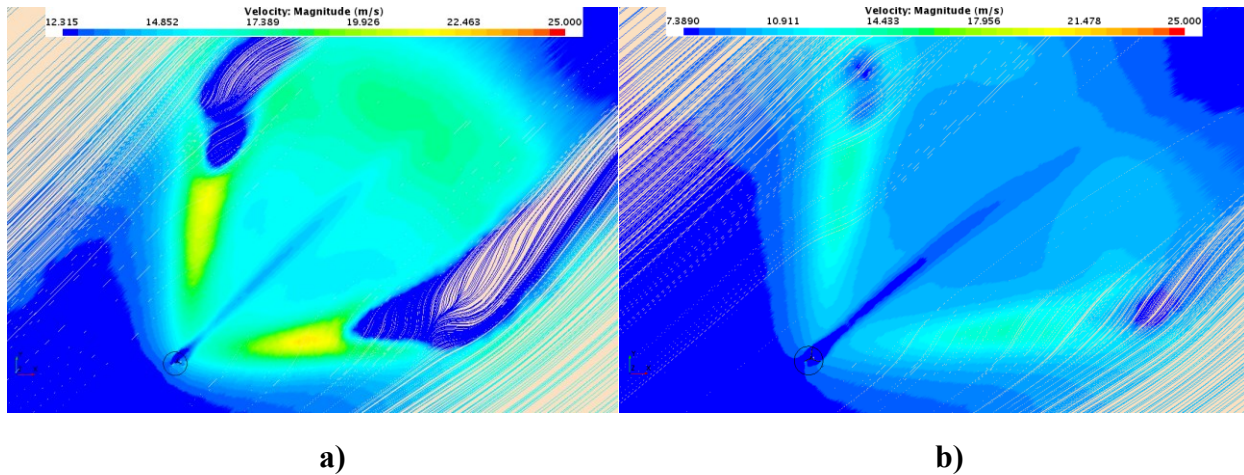


Figure 65: Top views of flow streamlines at the rotor's center XY plane from a) the TSR=3 case with a 45°, positive Y wind and b) the TSR=5 case with a 45°, positive Y wind

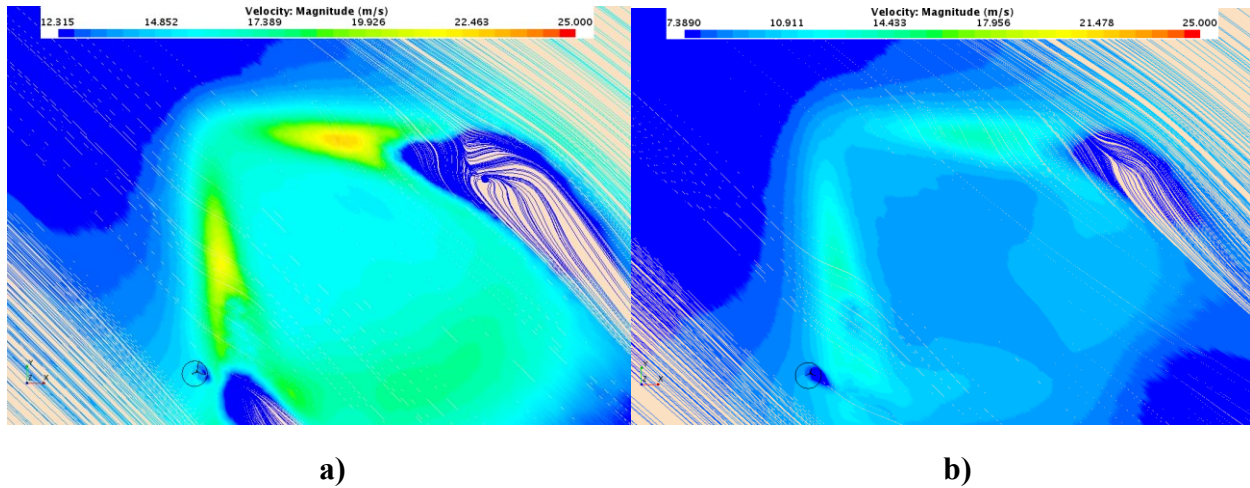


Figure 66: Top views of flow streamlines at the rotor's center XY plane from a) the TSR=3 case with a 45°, negative Y wind and b) the TSR=5 case with a 45°, negative Y wind

Table 8: Approximate wakes' dimensions for building's corner cases

Approximate wakes' dimensions for building's corner cases			
TSR	Wind direction	Wake's length measured in the wind direction	Wake's width in Z measured at half its length
3	45° in the positive Y direction	1.5D	1D
	Straight (positive X)	1D	0.5D
	45° in the negative Y direction	1D	1D
5	45° in the positive Y direction	13D	0.5D
	Straight (positive X)	2D	1D
	45° in the negative Y direction	2D	1D

In Figure 64 to 66, one can observe, from the TSR=5 cases, that the flows' speeds downstream of the VAWT's wakes are reduced on longer distances and take longer to recover than in their respective TSR=3 simulations. Knowing that the rotor performs better in the TSR=5 scenarios, this flow behavior is to be expected.

The approximate wakes' dimensions for the building's corner cases are given in Table 8. From this table, it is found that the rotor wake's length of the 45° , positive Y wind case with a TSR of 5 is 8.67 times higher than the corresponding wake from the TSR=3 simulation. One can also conclude, from the data shown in Table 8, that although the rotor's wakes are longer when the VAWT operates at a TSR=5, they are not necessarily wider, as shown again by comparing the positive Y cases.

It is also apparent, from the results obtained in the building's corner simulations, that in general the wakes are shorter than when the turbine operates in a freestream. This effect on the wakes' structures is a result of the mixing between the accelerated flow above the building's roof and the wakes themselves. From the position 2 results, it is also determined that the interactions with the flow around the building changes the wake structure by mixing flow from the recirculation region, as previously stated in section 5.1.

CHAPTER 6: CONCLUSIONS AND FUTURE WORK

6.1: Summary and Conclusions

Multiple 3D unsteady CFD simulations of a roof-mounted Darrieus VAWT model, with a Troposkien shape, were conducted as part of this thesis work using the Star CCM+ software. The model's geometry is equivalent to the one tested experimentally by Sheldahl [33]. The goals of these simulations were to evaluate the power extracting performance of the turbine, when it is operating under various flow conditions, as well as analyze the rotor wake's behavior and shape in each of the tested cases. Two different positions for the rotor were studied in the roof-mounted scenarios, one was above the center upstream edge of the cubic building at a height corresponding to position 2 in Samson's work [8] and the other was sitting above one of the building's upstream corners at a height of one rotor diameter. The Menter $k-\omega$ SST turbulence model was used, for both the validation and roof-mounted cases, due to its better accuracy in resolving boundary layers containing adverse pressure gradients. The methodology applied to prepare and run the simulations was validated with experimental results from Sheldahl's work [33] and Bedon's paper [54]. A constant velocity profile was applied at the inlet of the validation cases, whereas an atmospheric boundary layer was generated at the inlet of the roof-mounted simulations' domains in an attempt to simulate urban wind flow conditions. The roof-mounted cases were performed using three different tip speed ratios and three different wind directions.

When the turbine operates under a wind flow perpendicular to the upstream face of the building and is located at position 2, an increase of 30% is noted between the TSR=6 simulation's C_p and the highest C_p obtained from the simulations without the building. This improvement in performance is due to the rotor's presence inside the accelerated flow region above the upstream edge of the building. The rotor's wake clearly mixed with the vortex formation on top of the building and thus could not be properly sized due to the resulting changes in its structure. When one considers the building's corner simulations, it is found that the TSR=3 cases yielded very low and similar coefficients of power to what would be expected from a simulation without the building. On the other hand, the coefficients of power obtained from the TSR=5 scenarios are much higher than the highest calculated C_p of the cases without the building. Indeed, the C_p computed from the 45° negative Y wind direction case showed an improvement of 73% over the TSR=4.5 validation case's C_p . Thus, it is clear that the Darrieus VAWT's power extracting performance can be substantially improved from its baseline configuration, for certain TSR values, when the rotor is properly located above the building's roof. The rotor wakes' approximate measurements, taken from the building's corner cases, show that the wakes tend to be shorter than what would be expected if the rotor would operate in a freestream. The mixing process between these wakes and the accelerated wind flow above the roof is the cause of this impact on the wakes'

structures. It is also found that the wakes obtained from the $TSR=5$ simulations show wind speeds below $0.9V_t$ on a much higher portion of their center cross-sections, in comparison to the $TSR=3$ cases. This observation further supports the conclusion that the Darrieus VAWT's rotor operates better at a $TSR=5$, when located at this position above the building, than at a $TSR=3$.

6.2: Future Work

As mentioned previously in chapter 5.1, the addition of other Darrieus VAWT rotors downstream of the one located at position 2 should be investigated to evaluate their performance. Also, based on the obtained streamline contours of the cases with the rotor located above the building's corner, the possibility of adding another rotor above the Negative Y surface's edge of the building should be investigated. The new Darrieus rotor should be at a distance of at least $4D$ in the X direction from the original rotor, to avoid being affected by its wake, as well as being high enough to lie outside the separated flow region.

In this work, the velocity profile is not affected by the presence of other buildings or other obstacles on the roof. Furthermore, the shape of the cubic building itself is not modeled after an existing building and has no irregularities in its shape. It would be interesting to see how these conditions would affect the performance of the VAWT when it is installed at various locations above the roof. Furthermore, more wind directions and velocity profiles should be studied to analyze their impacts on the VAWT's performance. Investigating the effects of changing the rotational speed of the rotor, modifying its size and/or increasing the height of the building should also be considered in the future. The obtained results should also be validated with experimental data.

It is interesting to note that the shape and the height of the tested cubic building are both similar to those of small community buildings located in remote northern regions. The data collected in this work should therefore be considered in future analyses of this wind turbine model's performance when it is located above the roof of buildings present in these regions.

If a single rotor is present, positioning it at a different corner or location above the building's roof should be done to determine how it would impact its performance. For a case involving the same cubic building studied here with an angled flow direction, the selected rotor's position should attempt to take advantage of the accelerated flow above the two edges of the building. It is also important to note that the results presented in this thesis do not take into account mechanical losses, which should also be investigated in the future.

REFERENCES

- [1] S. Bilgen, “Structure and environmental impact of global energy consumption,” *Renewable and Sustainable Energy Reviews*, vol. 38, pp. 890–902, Oct. 2014, doi: [10.1016/j.rser.2014.07.004](https://doi.org/10.1016/j.rser.2014.07.004).
- [2] BP, “BP Statistical Review of World Energy,” 2019. [Online]. Available: <https://www.bp.com/content/dam/bp/business-sites/en/global/corporate/pdfs/energy-economics/statistical-review/bp-stats-review-2019-full-report.pdf>. [Accessed 17 October 2020].
- [3] J. Olivier, K. Schure and J. Peters, “Trends in global CO₂ and total greenhouse gas emissions - 2017 Report,” PBL Netherlands Environmental Assessment Agency, The Hague, 2017.
- [4] Global Wind Energy Council, “Global Wind Report 2018,” Brussels, 2019. [Online]. Available: <https://gwec.net/wp-content/uploads/2019/04/GWEC-Global-Wind-Report-2018.pdf>. [Accessed 17 October 2020].
- [5] K. Marvel, B. Kravitz, and K. Caldeira, “Geophysical limits to global wind power,” *Nature Climate Change*, vol. 3, p. 118, Sep. 2012.
- [6] R. J. Barthelmie *et al.*, “Comparison of Wake Model Simulations with Offshore Wind Turbine Wake Profiles Measured by Sodar,” *J. Atmos. Oceanic Technol.*, vol. 23, no. 7, pp. 888–901, Jul. 2006, doi: [10.1175/JTECH1886.1](https://doi.org/10.1175/JTECH1886.1).
- [7] R. Wiser, M. Hand, J. Seel, and B. Paulos, “Reducing Wind Energy Costs through Increased Turbine Size: Is the Sky the Limit?,” p. 7, Nov. 2016.
- [8] S. Victor, “UNSTEADY AND THREE-DIMENSIONAL CFD SIMULATION OF A DARRIEUS TURBINE ON THE ROOF OF A BUILDING,” p. 76, Jul. 2017.
- [9] P. A. Larin, “CFD Based Synergistic Analysis of Wind Turbine for Roof Mounted Integration,” p. 85, Apr. 2016.

- [10] E. Arteaga-López, C. Ángeles-Camacho, and F. Bañuelos-Ruedas, “Advanced methodology for feasibility studies on building-mounted wind turbines installation in urban environment: Applying CFD analysis,” *Energy*, vol. 167, pp. 181–188, Jan. 2019, doi: [10.1016/j.energy.2018.10.191](https://doi.org/10.1016/j.energy.2018.10.191).
- [11] United Nations Environment Programme, “Buildings and Climate Change - Summary for Decision-Makers,” Paris, 2009. [Online]. Available: <http://admin.indiaenvironmentportal.org.in/files/SBCI-BCCSummary.pdf>. [Accessed 17 October 2020].
- [12] A. Untaroiu, A. Raval, H. G. Wood, and P. E. Allaire, *Boundary Layer Control for a Vertical Axis Wind Turbine Using a Secondary-Flow Path System*. June 2011.
- [13] E. Hau, *Wind Turbines: Fundamentals, Technologies, Application, Economics*. Springer Science & Business Media, pp. 69-71, 2013.
- [14] D. Song, X. Fan, J. Yang, A. Liu, S. Chen, and Y. H. Joo, “Power extraction efficiency optimization of horizontal-axis wind turbines through optimizing control parameters of yaw control systems using an intelligent method,” *Applied Energy*, vol. 224, pp. 267–279, Aug. 2018, doi: [10.1016/j.apenergy.2018.04.114](https://doi.org/10.1016/j.apenergy.2018.04.114).
- [15] A. Hemami, *Wind Turbine Technology*. Nelson Education, pp. 48, 2012.
- [16] G. Müller, M. F. Jentsch, and E. Stoddart, “Vertical axis resistance type wind turbines for use in buildings,” *Renewable Energy*, vol. 34, no. 5, pp. 1407–1412, May 2009, doi: [10.1016/j.renene.2008.10.008](https://doi.org/10.1016/j.renene.2008.10.008).
- [17] W. Tjiu, T. Marnoto, S. Mat, M. H. Ruslan, and K. Sopian, “Darrieus vertical axis wind turbine for power generation I: Assessment of Darrieus VAWT configurations,” *Renewable Energy*, vol. 75, pp. 50–67, Mar. 2015, doi: [10.1016/j.renene.2014.09.038](https://doi.org/10.1016/j.renene.2014.09.038).
- [18] A. Al-Quraan, T. Stathopoulos, and P. Pillay, “Comparison of wind tunnel and on site measurements for urban wind energy estimation of potential yield,” *Journal of Wind Engineering and Industrial Aerodynamics*, vol. 158, pp. 1–10, Nov. 2016, doi: [10.1016/j.jweia.2016.08.011](https://doi.org/10.1016/j.jweia.2016.08.011).

- [19] N. C. Batista, R. Melício, V. M. F. Mendes, M. Calderón, and A. Ramiro, “On a self-start Darrieus wind turbine: Blade design and field tests,” *Renewable and Sustainable Energy Reviews*, vol. 52, pp. 508–522, Dec. 2015, doi: [10.1016/j.rser.2015.07.147](https://doi.org/10.1016/j.rser.2015.07.147).
- [20] T. Stathopoulos *et al.*, “Urban wind energy: Some views on potential and challenges,” *Journal of Wind Engineering and Industrial Aerodynamics*, vol. 179, pp. 146–157, Aug. 2018, doi: [10.1016/j.jweia.2018.05.018](https://doi.org/10.1016/j.jweia.2018.05.018).
- [21] S. J. Kooiman and S. W. Tullis, “Response of a Vertical Axis Wind Turbine to Time Varying Wind Conditions Found within the Urban Environment,” *Wind Engineering*, vol. 34, no. 4, pp. 389–401, Jun. 2010, doi: [10.1260/0309-524X.34.4.389](https://doi.org/10.1260/0309-524X.34.4.389).
- [22] A. Kc, J. Whale, and T. Urmee, “Urban wind conditions and small wind turbines in the built environment: A review,” *Renewable Energy*, vol. 131, pp. 268–283, Feb. 2019, doi: [10.1016/j.renene.2018.07.050](https://doi.org/10.1016/j.renene.2018.07.050).
- [23] D. R. Drew, J. F. Barlow, T. T. Cockerill, and M. M. Vahdati, “The importance of accurate wind resource assessment for evaluating the economic viability of small wind turbines,” *Renewable Energy*, vol. 77, pp. 493–500, May 2015, doi: [10.1016/j.renene.2014.12.032](https://doi.org/10.1016/j.renene.2014.12.032).
- [24] A. Rezaeiha, I. Kalkman, H. Montazeri, and B. Blocken, “Effect of the shaft on the aerodynamic performance of urban vertical axis wind turbines,” *Energy Conversion and Management*, vol. 149, pp. 616–630, Oct. 2017, doi: [10.1016/j.enconman.2017.07.055](https://doi.org/10.1016/j.enconman.2017.07.055).
- [25] A. Subramanian *et al.*, “Effect of airfoil and solidity on performance of small scale vertical axis wind turbine using three dimensional CFD model,” *Energy*, vol. 133, pp. 179–190, Aug. 2017, doi: [10.1016/j.energy.2017.05.118](https://doi.org/10.1016/j.energy.2017.05.118).
- [26] A. Rezaeiha, I. Kalkman, and B. Blocken, “Effect of pitch angle on power performance and aerodynamics of a vertical axis wind turbine,” *Applied Energy*, vol. 197, pp. 132–150, Jul. 2017, doi: [10.1016/j.apenergy.2017.03.128](https://doi.org/10.1016/j.apenergy.2017.03.128).
- [27] F. Ottermo and H. Bernhoff, “An upper size of vertical axis wind turbines,” *Wind Energy*, vol. 17, no. 10, pp. 1623–1629, 2014, doi: [10.1002/we.1655](https://doi.org/10.1002/we.1655).

- [28] S. Eriksson, H. Bernhoff, and M. Leijon, "A 225 kW Direct Driven PM Generator Adapted to a Vertical Axis Wind Turbine," *Advances in Power Electronics*, 2011. <https://www.hindawi.com/journals/ape/2011/239061/abs/> (accessed Aug. 21, 2019).
- [29] P. M. Kumar, K. Sivalingam, T.-C. Lim, S. Ramakrishna, and H. Wei, "Review on the Evolution of Darrieus Vertical Axis Wind Turbine: Large Wind Turbines," *Clean Technologies*, vol. 2, no. 1, pp. 52–70, Sep. 2019, doi: [10.3390/cleantechnol2010004](https://doi.org/10.3390/cleantechnol2010004).
- [30] B. F. Blackwell and G. E. Reis, "Blade shape for a troposkien type of vertical-axis wind turbine," Sandia Labs., Albuquerque, NM (USA), SLA-74-0154, Mar. 1977. Accessed: Aug. 27, 2019. [Online]. Available: <https://www.osti.gov/biblio/7257563>.
- [31] I. Paraschivoiu, *Wind Turbine Design: With Emphasis on Darrieus Concept*. Presses inter Polytechnique, 2002.
- [32] T. D. Ashwill, T. M. Leonard, T. D. Ashwill, and T. M. Leonard, *Developments in Blade Shape Design for a Darrieus Vertical Axis Wind Turbine*. 1986.
- [33] R. Sheldahl, "Comparison of Field and Wind Tunnel Darrieus Wind Turbine Data," Sandia National Laboratory, 1981.
- [34] Y. Wang, X. Sun, X. Dong, B. Zhu, D. Huang, and Z. Zheng, "Numerical investigation on aerodynamic performance of a novel vertical axis wind turbine with adaptive blades," *Energy Conversion and Management*, vol. 108, pp. 275–286, Jan. 2016, doi: [10.1016/j.enconman.2015.11.003](https://doi.org/10.1016/j.enconman.2015.11.003).
- [35] N. Ma *et al.*, "Airfoil optimization to improve power performance of a high-solidity vertical axis wind turbine at a moderate tip speed ratio," *Energy*, vol. 150, pp. 236–252, May 2018, doi: [10.1016/j.energy.2018.02.115](https://doi.org/10.1016/j.energy.2018.02.115).
- [36] M. Rossander *et al.*, "Evaluation of a Blade Force Measurement System for a Vertical Axis Wind Turbine Using Load Cells," *Energies*, vol. 8, no. 6, pp. 5973–5996, Jun. 2015, doi: [10.3390/en8065973](https://doi.org/10.3390/en8065973).

- [37] F. Balduzzi, J. Drofelnik, A. Bianchini, G. Ferrara, L. Ferrari, and M. S. Campobasso, “Darrieus wind turbine blade unsteady aerodynamics: a three-dimensional Navier-Stokes CFD assessment,” *Energy*, vol. 128, pp. 550–563, Jun. 2017, doi: [10.1016/j.energy.2017.04.017](https://doi.org/10.1016/j.energy.2017.04.017).
- [38] F. Toja-Silva, T. Kono, C. Peralta, O. Lopez-Garcia, and J. Chen, “A review of computational fluid dynamics (CFD) simulations of the wind flow around buildings for urban wind energy exploitation,” *Journal of Wind Engineering and Industrial Aerodynamics*, vol. 180, pp. 66–87, Sep. 2018, doi: [10.1016/j.jweia.2018.07.010](https://doi.org/10.1016/j.jweia.2018.07.010).
- [39] F. Toja-Silva, C. Peralta, O. Lopez-Garcia, J. Navarro, and I. Cruz, “Roof region dependent wind potential assessment with different RANS turbulence models,” *Journal of Wind Engineering and Industrial Aerodynamics*, vol. 142, pp. 258–271, Jul. 2015, doi: [10.1016/j.jweia.2015.04.012](https://doi.org/10.1016/j.jweia.2015.04.012).
- [40] D. Micallef, T. Sant, and C. Ferreira, “The influence of a cubic building on a roof mounted wind turbine,” *J. Phys.: Conf. Ser.*, vol. 753, p. 022044, Sep. 2016, doi: [10.1088/1742-6596/753/2/022044](https://doi.org/10.1088/1742-6596/753/2/022044).
- [41] I. Abohela, “Effect of roof shape, wind direction, building height and urban configuration on the energy yield and positioning of roof mounted wind turbines,” *Renewable Energy*, vol. 50, pp. 1106–1118, Feb. 2013, doi: [10.1016/j.renene.2012.08.068](https://doi.org/10.1016/j.renene.2012.08.068).
- [42] T. Wizelius, *Developing wind power projects: Theory and Practice*, 2006.
- [43] S. Liu, W. Pan, H. Zhang, X. Cheng, Z. Long, and Q. Chen, “CFD simulations of wind distribution in an urban community with a full-scale geometrical model,” *Building and Environment*, vol. 117, pp. 11–23, May 2017, doi: [10.1016/j.buildenv.2017.02.021](https://doi.org/10.1016/j.buildenv.2017.02.021).
- [44] M. Ragheb and A. M. Ragheb, “Wind Turbines Theory - The Betz Equation and Optimal Rotor Tip Speed Ratio,” *Fundamental and Advanced Topics in Wind Power*, Jul. 2011, doi: [10.5772/21398](https://doi.org/10.5772/21398).
- [45] Siemens, STAR-CCM+ User Guide, Version 12.06.011, Siemens PLM Software, 2019

- [46] M. Ghasemian, Z. N. Ashrafi, and A. Sedaghat, "A review on computational fluid dynamic simulation techniques for Darrieus vertical axis wind turbines," *Energy Conversion and Management*, vol. 149, pp. 87–100, Oct. 2017, doi: [10.1016/j.enconman.2017.07.016](https://doi.org/10.1016/j.enconman.2017.07.016).
- [47] D. A. Digaskar, "Simulations of Flow Over Wind Turbines," p. 101, May 2010.
- [48] K. Kim, "THREE-DIMENSIONAL HYBRID GRID GENERATOR AND UNSTRUCTURED FLOW SOLVER FOR COMPRESSORS AND TURBINES," p. 160, Dec. 2003.
- [49] H. Schlichting (Deceased) and K. Gersten, *Boundary-Layer Theory*. Springer, 2016.
- [50] J. O. Hinze, *Turbulence*, McGraw-Hill Publishing Co., New York, 1975.
- [51] G. Alfonsi, "Reynolds-Averaged Navier–Stokes Equations for Turbulence Modeling," *Applied Mechanics Reviews*, vol. 62, no. 4, p. 040802, Jul. 2009, doi: [10.1115/1.3124648](https://doi.org/10.1115/1.3124648).
- [52] D. C. Wilcox, *Turbulence Modeling for CFD*, 3rd ed. DCW Industries, 2006.
- [53] Menter, F.R., "Two-equation eddy-viscosity turbulence modeling for engineering applications", *AIAA Journal*, 32(8), pp. 1598-1605, Aug. 1994.
- [54] G. Bedon, E. Benini and S. Betta, "A computational assessment of the aerodynamic performance of a tilted Darrieus wind turbine," *Journal of Wind Engineering and Industrial Aerodynamics*, vol. 145, pp. 263-269, 2015.
- [55] L. Ledo, P. Kosasih and P. Cooper, "Roof mounting site analysis for micro-wind turbines," *Renewable energy*, vol. 36, no. 5, pp. 1379-1391, 2011.
- [56] A. U. Weerasuriya, "Computational Fluid Dynamic (CFD) simulation of flow around tall buildings," *Engineer*, vol. 46, no. 3, p. 43, Jul. 2013, doi: [10.4038/engineer.v46i3.6784](https://doi.org/10.4038/engineer.v46i3.6784).

[57] M. Zabarjad Shiraz, A. Dilimulati, and M. Paraschivoiu, “Wind power potential assessment of roof mounted wind turbines in cities,” *Sustainable Cities and Society*, vol. 53, p. 101905, Feb. 2020, doi: [10.1016/j.scs.2019.101905](https://doi.org/10.1016/j.scs.2019.101905).

[58] A. Peacock, D. Jenkins, M. Ahadzi, A. Turan, Berry and S., “Micro wind turbines in the UK domestic sector, ” *Energy and buildings*, vol. 40, no. 7, pp. 1324-1333, 2007.

[59] P. Ouro, S. Runge, Q. Luo and T. Stoesser, “Three-dimensionality of the wake recovery behind a vertical axis turbine,” Cardiff University, Cardiff, Jul. 2018. [Online]. Available: http://orca.cf.ac.uk/116392/1/Ouro_Runge_Luo_Stoesser_Original.pdf. [Accessed 18 October 2020].